博士論文

DEVELOPMENT OF ORGANIC - INORGANIC HYBRID MEMBRANES FOR CARBON DIOXIDE / METHANE SEPARATION

（CO_2 / CH_4 分離のための有機-無機ハイブリッド膜の開発）

BELHAJ MESSAOUD Souha

ベルハジュ　メッサウド　スヘー

Thesis Evaluation Committee

Professor Tatsuya OKUBO, The University of Tokyo

Professor Kazunari DOMEN, The University of Tokyo

Professor Kazuki AKAMATSU, Kogakuin University

Professor Yoshiko TSUJI, The University of Tokyo

Professor Hirokazu SUGIYAMA, The University of Tokyo

Professor Ryuji KIKICHI, The University of Tokyo

Professor S. Ted OYAMA (Supervisor), The University of Tokyo

الى المرأة التي ملأت حياتي عزيمة و تحدي وحب
الى جدتي حليمة الحرشاني

To my grand-mother HALIMA
You may be gone, but you will never be forgotten

Acknowledgments

I would like to express my deepest gratitude to Professor Ted OYAMA for his dedication to my supervision, his guidance throughout my research and his enthusiasm and constructive critiques throughout my Thesis research.

I would like also to thank the evaluation committee composed by Professor Tatsuya OKUBO, Professor Kazunari DOMEN, Professor Kazuki AKAMATSU, Professor Yoshiko TSUJI, and Professor Hirokazu SUGIYAMA for taking their time to review my thesis and their valuable suggestions and critiques.

I would like to show my sincere gratitude to Professor Riyuji KIKUCHI for his enlightening recommendations. I am thankful also to Doctor Atsushi TAKAGAKI and Mr. Takashi SUGAWARA for the support and encouragement whenever I was in need. I am grateful to Doctor Bernardo CASTRO DOMINGUEZ and Miss Pornravee LEELACHAIKUL for their significant contribution on the simulation part and Mr. Shunsuke SUZUKI for his tutoring for chemical vapor deposition method. I show also my appreciation to all OYAMA-KIKUCHI laboratory members for creating and maintaining a friendly and stimulating scientific environment.

I would like to acknowledge the Director, National Science Foundation, Division of Chemical, Bioengineering, Environmental, and Transport Systems (CBET) for the grant CBET-084316 and the Ministry of Education, Culture, Sports, Science and Technology (MEXT), Japan, for the scholarship to pursue this degree.

My special gratitude and love to my parents, Hamadi BELHAJ MESSAOUD and Rachida HORCHANI for their unequivocal support throughout my life. I would like to give my special thanks to my partner, Lassad BEN YOUNES, for the love, the continuous encouragement and the share of the ups and downs throughout the completion of this thesis.

Finally, I would like to take the opportunity to give my sincere appreciation to my caring sisters Emna and Maha, my dearest friends Phuong BUI, Douaa DHAHRI, Sahar GALAI, Meriem ENNEJEH, Olfa BERUMA and Oussema CHELLY, and my family in law for their patience, prayers and moral support during the course.

Abstract

Natural gas processing is one of the largest industrial gas separation applications worldwide. Membrane technology is an emerging technology which is increasingly competing with conventional separation processes. This thesis focuses on the development of hybrid membranes for the separation of carbon dioxide from methane. Hybrid membranes are promising materials since they combine the advantages of organic and inorganic materials. Two types of hybrid materials were investigated; alkylamine silica membranes and mixed matrix membranes. In the first type, amine groups were incorporated into silica matrix because of the well-known affinity between amine functionalities and CO_2. In the second type, silicoaluminophosphate zeolite (SAPO-34) was dispersed in polyetherimide polymer because SAPO-34 is selective to CO_2 permeation.

The first type of membrane was prepared by depositing an alkylamine silica selective layer on top of a multilayered alumina support using chemical vapor deposition (CVD). First, CVD parameters were optimized using (3-aminopropyltrimethoxysilane). It was found that the best combination used an N/Si ratio of 20% and a reaction temperature of 673 K. The membrane had a CO_2 permeance of 2.3×10^{-7} mol $m^{-2}s^{-1}Pa^{-1}$ and an ideal CO_2/CH_4 selectivity of 40 measured at a temperature of 393 K and a partial pressure difference of 0.10 MPa. The membrane pore size was determined by Tsuru's method and was 0.40 nm. The surface morphology and composition were also determined using SEM and XPS analyses, respectively. The transport mechanism for CO_2 permeation was facilitated transport and for CH_4 passage was gas-translation.

Primary and secondary amine functionalities were studied in order to understand the relationship between the microstructure and the performance of the membrane. Hybrid membranes were synthesized using 3-aminopropyltrimethoxysilane and (3-methylaminopropyl)trimethoxysilane as primary and secondary alkylamine-silica precursors, respectively. An amine free membrane prepared using propyltrimethoxysilane as precusor was used as reference membrane. The selective layer was also deposited by CVD using the optimum conditions determined forehead. The amine-free membrane had a CO_2 permeance of 2.1×10^{-8} mol $m^{-2}s^{-1}Pa^{-1}$, a CO_2/CH_4 selectivity of 4 and a pore size of 0.37 nm. The primary amine

membrane displayed a CO_2 permeance of $2.1x10^{-8}$ mol $m^{-2}s^{-1}Pa^{-1}$, an ideal CO_2/CH_4 selectivity of 70 with a pore size of 0.36 nm. The secondary amine achieved a CO_2 permeance of $1.3x10^{-7}$ mol $m^{-2}s^{-1}Pa^{-1}$, an ideal CO_2/CH_4 selectivity of 140 with a pore size of 0.43 nm. The pore sizes were also estimated by Tsuru's method. The transport mechanism of CO_2 throughout the amino-silica hybrid membranes was surface diffusion. The secondary amino-silica hybrid membrane was stable for 60 h under a relative humidity of 20%.

Mixed matrix membranes (MMMs) are hybrid materials prepared by dispersing inorganic particles in a polymeric matrix and are attracting increasing attention for the separation of CO_2/CH_4 mixtures. The zeolite SAPO-34 and polyetherimide were selected as the inorganic filler and the polymeric matrix for the synthesis of the supported MMMs. Two polymer solvents, dichloroethane and N-methyl-2-pyrrolidone, were investigated for the preparation, and the dichloroethane solvent resulted in a membrane with better CO_2/CH_4 selectivity. Various SAPO-34 amounts from 0 to 10 wt% were dispersed in the polymer precursor which was dissolved in dichloroethane. The membrane with 5 wt% SAPO-34 content presented the highest performance with a CO_2 permeance of $4x10^{-10}$ mol $m^{-2}s^{-1}Pa^{-1}$ and an ideal CO_2/CH_4 selectivity of 60. Based on mixed gas permeances and time-lag measurements, the separation of CO_2 and CH_4 was found to be dominated by the difference in the gas solubilities. The SAPO-34 decreased CH_4 transport by increasing its diffusion pathway. Particle agglomeration was observed at 10 wt% zeolite loading in the polymeric matrix.

Finally, an economic optimization was performed in order to determine optimum points within Robeson upper boundary which is a line linking the most permeable polymer membranes at a particular selectivity. Four gas pairs: CO_2/N_2, O_2/N_2, CO_2/CH_4, and N_2/CH_4 were considered in the study. The constraints used to limit the optimal points are based on the cost of the membrane, the number of units required to achieve a specific separation, and the compression requirements. The total costs include the fees for utilities and capital costs, and interest payments. The model results are verified against other studies, while initial and targeted parameters are subject to a sensitivity analysis. The optimum points obtained at an operating pressure of 1 MPa were for CO_2/N_2 a permeability of 3,200 barrers and a selectivity of 24, for O_2/N_2 a permeability of 550 barrers and a selectivity of 4, for CO_2/CH_4 a permeability of 2,000 barrers and a selectivity of 20, and for N_2/CH_4 a permeability of 110 barrers and a selectivity of 2. Secondary alkylamine silica membrane and mixed matrix membrane with 5 wt% SAPO-34 content were

evaluated using the proposed simulation. It was found that the alkylamine membrane resulted in the lowest operating costs for the separation of CO_2 and CH_4 mixtures.

Contents

Chapter 1: General introduction

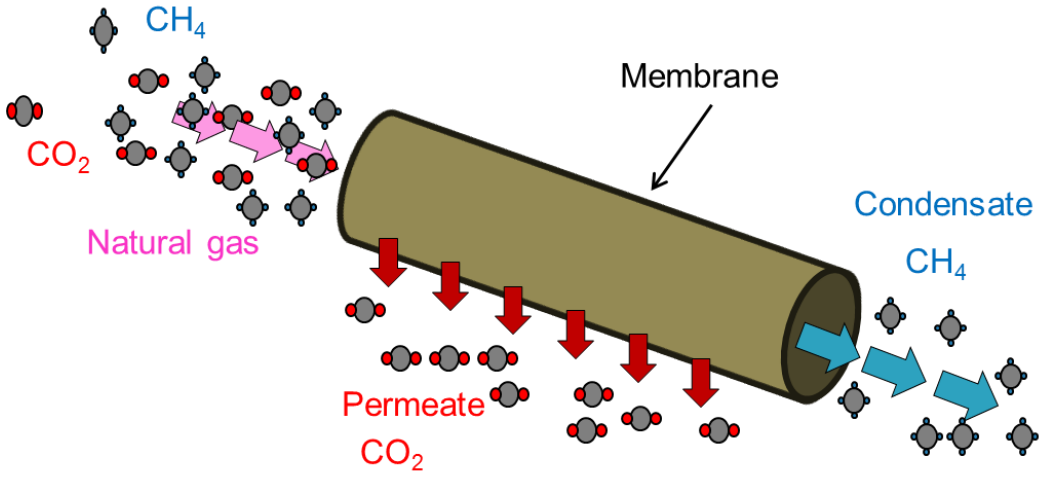

1.1. General background

In order to satisfy simultaneously the continuous increase of global energy demand [1] and the necessity to live in a cleaner environment [2], a highly pure, an economical and an environmentally friendly energy is needed. Natural gas is considered the cleanest primary energy that fulfills all the above mentioned requirements since it emits 30% less of greenhouse gases than conventional fossil fuel (oil, coal). Generally, over 70% of natural gas is formed by methane. Methane has several applications in various fields such as steam heat production, power generation, manufacturing, polyethylene synthesis. However, the crude gas contains also a mixture of various impurities (**Table 1**). As it can be seen, natural gas contains hydrocarbons such as ethane, propane, butane, and non-hydrocarbons such as carbon dioxide, nitrogen. The composition depends on the gas well [3]. In order to meet the usage and shipment quality standard specifications [4], most of the impurities must be removed. Carbon dioxide (CO_2), in particular, appears in high percentage in the composition of the raw gas (up to 70% of the total raw gas volume) [5]. This acid gas reduces the heating value of natural gas, corrodes process equipment, and freezes at a relatively high temperature. Therefore, it needs to be removed. There are several CO_2 removal processes available. Absorption processes including chemical and physical absorption, adsorption processes including thermal swing adsorption, pressure swing adsorption and displacement desorption, cryogenic processes, and recently, membrane technology. Generally, membranes can compete with conventional gas separation technologies especially in small scale processing plants [6,7]. Khol et al. [8] stated that compared to aforementioned separation processes membranes have " low capital investment, ease of operation, automatized process, good weight and space efficiency, minimal associated hardware, no moving parts, ease of installation, flexibility, minimal utility requirements, low environmental impact, reliability, ease of incorporation of new membrane developments".

Table 1: Typical composition of natural gas [9]

Component	Typical analysis (vol%)	Range (vol%)
Methane	94.9	87.0-96.0
Ethane	2.5	1.8-5.1
Propane	0.2	0.1-1.5
Isobutene	0.03	0.01-0.3
n-Butane	0.03	0.01-0.3
Isopentane	0.01	Trace to 0.14
n-Pentane	0.01	Trace to 0.14
Hexane	0.01	Trace to 0.06
Nitrogen	1.6	1.3-5.6
Carbon dioxide	0.7	0.1-1.0
Oxygen	0.02	0.01-0.1
Hydrogen	Trace	Trace to 0.02

1.2. Membranes for natural gas purification

Membrane technology is steadily gaining an important role in gas separation technology [10]. Membranes are selective barriers capable of allowing specific substances to pass through while retaining other components. Membrane material design (MMD) and membrane system engineering (MSE) are two defined areas in the field of membrane science and technology [11]. Membrane material design is used to select membranes for a particular application taking into account criteria such as stability, robustness of the material at operating conditions, productivity and separation efficiency [12]. However, membrane system engineering uses other parameters such as capital cost, operational simplicity, space and weight efficiency, ease of scalability and low power consumption when designing membrane technologies.

The most important properties of membranes for determining their performance are permeance and selectivity [13]. Permeance is an intrinsic property of the material that describes the gas flux transported for a specific pressure difference and membrane thickness. Permeances are calculated by using **Eq. (1)**:

$$\bar{P}_i = \frac{F_i}{A\,\Delta P_i} \qquad \textbf{Eq. (1)}$$

where $\bar{P}_i$ is the permeance of species *i* [mol $m^{-2}s^{-1}Pa^{-1}$], F_i is the molar flow rate of the gas *i* [mol s^{-1}], *A* is the surface area of the membrane [m^2] and ΔP_i is the partial pressure difference of a gas *i* between the inner and the outer side of the membrane tube [Pa].

Whereas, the selectivity reflects the efficiency of a membrane to separate one gas from another. The selectivity is designated as "ideal selectivity" or "permselectivity", when the permeance measurements involve pure single gases. In this case, the selectivity is the ratio of pure gas permeance of two species *i* and *j*. The permeance measurements are carried out at the same experimental conditions such as same temperature and partial pressure difference [14,15]. The ideal selectivity is written as follow:

$$\alpha^*_{i,j} = \frac{\bar{P}_i}{\bar{P}_j} \qquad \textbf{Eq. (2)}$$

where $\alpha^*_{i,j}$ is the selectivity of a specie *i* over *j* [-], $\bar{P}_i$ and $\bar{P}_j$ are the permeances of species *i* and *j*, respectively [mol $m^{-2}s^{-1}Pa^{-1}$].

However, the selectivity is denoted as "separation factor" or "separation selectivity", when mixed or binary gases are used for permeance measurements,. The separation selectivity can be written as the ratio of mole fractions of gases [14,16] as written in **Eq. (3)**.

$$\alpha_{i/j} = \frac{\left(y_i/y_j\right)_{Permeate}}{\left(x_i/x_j\right)_{Feed}} \qquad \textbf{Eq. (3)}$$

where y_i and y_j are the mole fractions of species *i* and *j* at the permeate side and x_i and x_j are the mole fractions in the feed side.

The permeance can also be expressed by gas permeation unit (GPU), where 1 GPU = $1x10^{-6}$ cm^3(STP) $cm^{-2}s^{-1}cmHg^{-1}$ = $3.35x10^{-10}$ mol $m^{-2}s^{-1}Pa^{-1}$.

Often membranes exhibit a trade-off relationship between permeability and selectivity. The permeability is the gas permeance normalized to the membrane thickness. For instance, high selectivities lead to high gas flux resistance resulting in low permeabilities. Robeson [17,18]

summarized the behavior of different polymeric membranes toward various pair gases leading to the concept of the empirical upper bound. The upper bound is a locus of points, usually a line, where the optimum selectivity and permeability are obtained. The Robeson diagram often plots the gas permeability as a function of gas pair selectivity. The gas permeability in the Robeson diagram is often expressed in barrer, where 1 barrer = $3.3x10^{-19}$ kmol m $m^{-2}s^{-1}Pa^{-1}$. Iarikov and Oyama [19] compared the performance of several types of membranes used for CO_2/CH_4 separation as shown in **Fig. 1**. The shaded area in this figure indicates the most desirable region for membrane performance, with a permeance above $1x10^{-7}$ mol $m^{-2}s^{-1}Pa^{-1}$ and an ideal CO_2/CH_4 selectivity over 40. This region represents membranes with a superior performance compared to commercially available systems [19]. From **Fig. 1**, various membranes for CO_2/CH_4 separation can be distinguished and can be classified into three main categories; polymeric, inorganic and hybrid membranes.

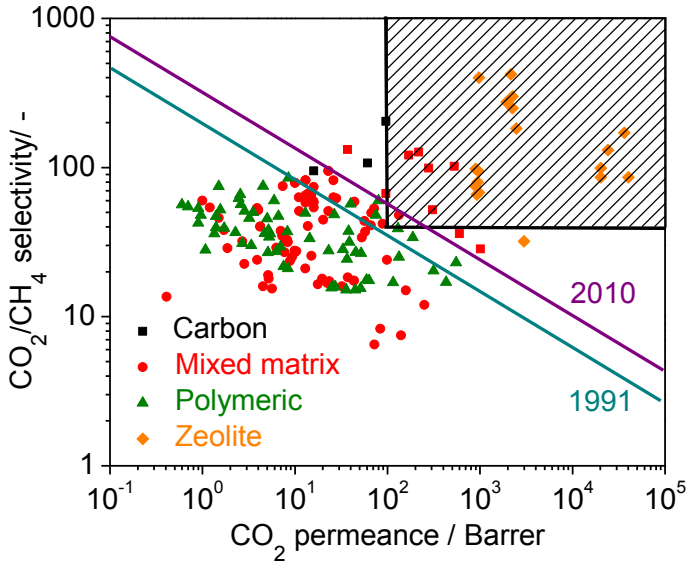

Fig. 1: Carbon dioxide/ Methane ideal selectivity plotted against carbon dioxide permeance (in barrers) for different membrane systems with a membrane thickness of 1 μm [19].

1.2.1. Organic membranes

Organic membranes are generally composed of polymers. They are widely used in gas separation due to the low cost, the simplicity of processing, and the ease to scale up [19,20]. They are classified based on their ability to operate either above (rubbery polymers) or below

(glassy polymers) their glass transition temperature. Polymeric membranes are generally formed by a thin non-porous selective layer supported on a thicker porous layer [19]. They separate gas by solution-diffusion mechanism (see **section 1.4.4. Solution-diffusion**).

Among polymeric membranes, membranes that operate by facilitated transport have been found to exhibit good performance for CO_2 separation [21,22,23,24]. These membranes consist of a carrier agent which is incorporated into the membrane material to react reversibly and selectively with the targeted gas, while the unreacted gases permeate by a solution-diffusion mechanism. For the separation of CO_2, polyallylamine, 2-aminoisobutyric acid potassium salt [21], chitosan [22] and DL-2,3-diaminopropionic acid hydrochloride [23] have been employed as carrier agents. Facilitated transport membranes can have either immobilized carriers in which the carrier agent is fixed to a support matrix by chemical bonding, or can have mobile carriers in which the carrier agent can move through the membrane. Yegani et al. [23] prepared a polyvinyl alcohol-polyacrylic acid copolymer membrane containing a mobile carrier and achieved a CO_2 permeance of 1.10×10^{-7} mol $m^{-2}s^{-1}Pa^{-1}$ and a CO_2/N_2 selectivity of 432 at 433 K under humid conditions. Kai et al. [25] synthesized a polyamidoamine dendrimer composite membrane and obtained a CO_2 permeance of 8.0×10^{-9} mol $m^{-2}s^{-1}Pa^{-1}$ and CO_2/N_2 selectivity of 150 at 313 K with durability exceeding 1000 hours.

However, polymeric membranes suffer from the ease of plasticization in contact with highly pressurized CO_2 [26]. As a result, processes for CO_2 separation using organic membranes were usually performed at relatively low temperatures [27].

1.2.2. Inorganic membranes

Inorganic membranes are useful for CO_2 separation under high temperature and pressure when organic based membranes are not functional [28,29]. They are mainly zeolite membranes [2630,31,32,33,34], silicate based membranes [35,36], and silica membranes [37,38,39].

Zeolite membranes are promising membranes. Zeolies are crystalline aluminosilicates with well-defined repeating pore structure [19]. They separate gas molecules by molecular sieve effects and favor the adsorption of CO_2 over CH_4 on most zeolites (see **section 1.4.2. Surface diffusion or molecular sieving**). Several zeolites are effective for CO_2/CH_4 separation since they have pore size similar to CH_4 but larger than CO_2. Silicoaluminophosphate (SAPO-34), T-type zeolite and deca-dodecasil 3R (DDR) are zeolites that have 0.38, 0.41, and 0.36 nm pore

diameter, respectively. Li et al. [31] synthesized SAPO-34 membrane in situ by crystallization onto porous stainless steel support, and obtained a CO_2 permeance of 5×10^{-7} mol $m^{-2}s^{-1}Pa^{-1}$ and a CO_2/CH_4 selectivity higher than 200 at 295 K for a feed pressure of 138 kPa and a 50/50 feed. Cui et al. [26] synthesized T-type zeolite membrane and obtained a CO_2 permeance of 2×10^{-8} mol $m^{-2}s^{-1}Pa^{-1}$ and a CO_2/CH_4 selectivity of 266 at 343 K in single gas experiment. Tomita et al. [33] prepared DDR membranes and obtained a CO_2 permeance of 7×10^{-8} mol $m^{-2}s^{-1}Pa^{-1}$ and a CO_2/CH_4 selectivity of 220 at 301 kPa for a pressure drop of 0.5 MPa. However, even though high performance was obtained, zeolite membranes suffer from formation of defects when produced at bigger scale due to their crystalline structures [40,41].

1.2.3. Hybrid membranes

Mixing both organic and inorganic materials is away to improve membrane performance. Hybrid membranes consist then in either incorporating inorganic materials into organic matrix or adding organic groups into inorganic matrix.

1.2.3.1. Mixed matrix membranes

Mixed matrix membranes (MMMs) are hybrid materials prepared by dispersing inorganic materials into continuous polymeric matrix. The MMMs associate the merits of both polymers such as low cost, high flexibility and easy processing and inorganic particles such as high permeability and high selectivity [42]. Inorganic fillers include various materials such as zeolites [43], carbon molecular sieves [44,45,46], activated carbons [47], mesoporous materials [48], non-porous silica [49], organic metallic framework [50], graphite [51]. They are classified into porous and non-porous fillers. Porous materials separate gases by molecular sieving, whereas, non-porous materials increase the permeated diffusion path of gas molecules within the polymeric matrix increasing, hence, the selectivity of small molecules compared to larger one [52]. Porous materials, especially zeolites, showed the best gas selectivity. Zhang et al. [53] reported the use of Matrimid® and mesoporous ZSM-5 nanoparticles. The separation of H_2/CH_4 improved from 83.3 to 169. Hosseini et al. [54] developed a MMM by mixing Matrimid® with MgO nanoparticles. The membrane was post-treated by immersed in silver solution. The best performance was obtained at 20 wt% MgO loading after 10 days of silver treatment. The CO_2/CH_4 selectivity increased by 50%. Sadeghi et al. [55] incorporated silica nanoparticles into

polybenzimidazole matrix. The silica nanoparticles increased the solubility but decreased the diffusivity of gases. The permeabilities of condensable gases such as CO_2 and CH_4 were higher whereas the permeability of non-condensable N_2 gas was lower.

Despite improvements obtained by adding inorganic fillers, these composite membranes still suffer in some cases from material incompatibility leading to the formation of voids or defects between the polymer chains and the inorganic filler resulting in higher gas diffusion [56]. Three main methods were investigated in order to improve polymer/sieve interaction [28,57]:

- Preparation of hybrid materials with van der Waals forces or hydrogen bounds interactions [58],
- Addition of small amount of polymer solution to nanoparticle suspension before mixing with the whole polymer precursor. This procedure defined as "priming" tends to minimize the stress at the polymer/nanoparticle interface [59].
- Reaction of silanes simultaneously with hydroxyl groups, amine groups and/or other functional groups from the zeolite and/or the polymer [60,61,62,63,64,65,66].

1.2.3.2. Composite carbon membranes

Carbon membranes are obtained after the pyrolysis of polymeric membranes. Several steps are involved in the preparation of carbon membranes [67]. Parameters selected in each step are essential to determine the characteristics of the resultant membrane. For instance, when selecting the polymer precursor, many factors should be taken into account such as aromatic carbon content, glass transition temperature, chemical stability and mechanical properties [68,69]. They determine the physico-chemical properties and the pore size of the resultant membrane. Polyimides [70], polyetherimides [71] and phenolic resins [72] satisfy those criteria and are usually chosen.

The gas permeability of the existing pure carbon membranes does not satisfy commercial requirements due to the disordered pore structure of the carbon matrix. In fact, Zhang et al. [73] and Huang et al. [74] stated that carbon membranes are brittle and demonstrated that the microstructure of the carbon matrix consists of disordered inter-connective nano-channels formed by the inter-granular holes (supermicropores) packed by the carbon microcrystals and the space (ultramicropores) existed between the carbon sheets. Therefore, high diffusion resistance of the gas molecules permeating through the membrane is generated. Supported carbon

membranes can overcome this deficiency by reducing the thickness of carbon layer to a range of less than 1 μm [75,76,77]. However, the disordered inter-connective nano-channels remain in the pure carbon matrix. They would still extend the gas permeance through the membrane. Recently, embedding inorganic particles into carbon membranes, particularly crystalline molecular sieve particles such as zeolites or ordered silica, has emerged as an efficient strategy for enhancing the transport properties. The gas separation permeability and selectivity of the new mixed matrix carbon membranes improved compared to pure carbon membranes or polymeric ones. This enhancement in membrane performance is related to the molecular dimension of the inorganic fillers. They open a special shaped and sized void that allows a specific gas to permeate faster [78]. Li et al. [78] prepared new mesoporous composite membrane by inserting ZSM-15, SBA-15 and MCM-48 particles into polyamic acid matrix and then carbonized the obtained membrane. They achieved a high CO_2 permability going from 1210, 1618 and 2485 barrers, respectively, with a high selectivity of 136, 170 and 146 correspondingly. Li et al [79] incorporated SAPO-34 crystals into a phenolic resin precursor. The membrane showed a CO_2 permeability of 3763 barrers for a selectivity of 87. Yin et al. [80] fabricated a Zeolite L/Carbon membrane using the polyfurfurylalcohol as polymer precursor and attained a permeability of carbon dioxide of 683 barrers with selectivity of 35.7. Lie et al. [81] added metal oxides and metal nitrate into carbon membranes. The modification increased micropore volume of the carbon matrix and promoted electronic interactions with CO_2 which can utilize the surface diffusion mechanism for enhanced CO_2 transport. The highest CO_2 permeance was 180 barrers with a CO_2/CH_4 selectivity of 130.

1.2.3.3. Silica modified membranes

Surface modification of silica matrix can dramatically change the chemical and the physical properties of materials. This technology is utilized in diverse fields including catalysis, semiconductors, and optics. Surface functionalization has been carried out in membrane technology to enhance CO_2 transport using phenyl and amine groups. Smaïhi et al. [82] synthesized inorganic-organic hybrid membranes using phenyl groups by means of a sol-gel method reaching a CO_2 permeance of $2.3x10^{-6}$ mol $m^{-2}s^{-1}Pa^{-1}$ with a CO_2/N_2 selectivity of 15 at 298 K. Okui et al. [83] used membranes with several organic functionalities such as methyl, propyl, 3-chloropropyl, (3, 3, 3-trifluoropropyl), octadecyl and phenyl groups. The membrane

having phenyl groups was the most efficient, giving a CO_2 permeance of $1.6x10^{-8}$ mol $m^{-2}s^{-1}Pa^{-1}$ and a CO_2/CH_4 selectivity of 6 at 298 K.

Amino group functionalized membrane materials are particularly effective for CO_2 separation and are believed to work by forming carbamates in a reversible manner [84,85,86,87,88]. During the separation, intermediate species are formed by the adsorption of CO_2 on the surface near the pore entrance. These species react with adjacent amine groups, resulting in the formation of carbamates. The gas diffuses into the pores using concentration difference (pressure difference) as the driving force. Consequently, the gas is transported by repetitive adsorption and desorption and the selectivity of CO_2 can be increased along with its permeance in contrast to other gases such as N_2, H_2 and CH_4 [89,90,91]. Sakamoto et al. [92] prepared amine-modified mesoporous silica membranes on porous alumina supports by sol-gel and spin-coating methods and reported a low CO_2 permeance of $1.0x10^{-9}$ mol $m^{-2}s^{-1}Pa^{-1}$ but a high CO_2/N_2 selectivity of 800 at 373 K using a 20/80 CO_2/N_2 gas mixture. Xoremitakis et al. [93] fabricated aminosilicate microporous membranes via a sol-gel process, resulting in a CO_2 permeance of $2.8x10^{-8}$ mol $m^{-2}s^{-1}Pa^{-1}$ and a CO_2/N_2 selectivity of 70 at 295 K for a ternary N_2-CO_2-H_2O gas stream of variable composition (1-20 vol.% CO_2-balance N_2, 0-40% relatively humidity). Ostwal et al. [89] modified a Vycor support tube using 3-aminopropyltriethoxysilane and obtained a CO_2 permeance $2.6x10^{-10}$ mol $m^{-2}s^{-1}Pa^{-1}$ with a CO_2/N_2 separation factor of 10 at 393 K using mixed gases. Hyun et al. [94] modified γ-Al_2O_3 /TiO_2 composite membranes by phenyltriethoxysilane and obtained a CO_2 permeance of $3.4x10^{-8}$ mol $m^{-2}s^{-1}Pa^{-1}$ and CO_2/N_2 selectivity of 1.7 at 363 K. Kang et al. [95] synthesized γ-Al_2O_3 composite membranes with a microporous silica layer using acidic silica solution to separate CO_2 and N_2. The membrane had a CO_2 permeance of $3.4x10^{-7}$ mol $m^{-2}s^{-1}Pa^{-1}$ and a CO_2/N_2 selectivity of 2.1. Chen et al. [96] made a hybrid membrane by adjusting a polymer silica hybrid matrix with a low molecular weight poly(ethylene glycol) dimethyl ether. In single gas measurements, the membrane containing 50 wt% additive showed CO_2 gas permeability of 1600 barrers and CO_2/H_2 selectivity and 13 at 308 K. Chua et al. [97] mixed polyetheramine with polyhedral oligomeric silsesquioxane to selectively separate CO_2 from N_2. The mechanical strength of the obtained membrane was improved and the CO_2 permeance reached 380 barrers with a CO_2/N_2 selectivity of 39 at 308 K.

1.3. Chemical vapor deposition

Amine-modified silica can be deposited either by sol-gel or chemical vapor deposition (CVD) methods. Sol-gel method leads to the formation of a porous layer when sol species is converted to gel state. This transition is achieved after a drying-calcining step at an appropriate temperature [98]. Paradis et al. [99] used a sol-gel procedure to prepare amino-silica hybrid membranes. Primary, mixed primary and secondary alkyl amino silicate and imidazole precursors were investigated. They reported a CO_2/N_2 selectivity of 4.9 at 423 K using a primary alkyl amine precursor (3-aminopropyltriethoxysilane). Xomeritakis et al. [100] synthesized membranes using 3-aminopropyl triethoxysilane as sol-gel precursor and obtained a CO_2 permeance of $2.58x10^{-8}$ mol $m^{-2}s^{-1}Pa^{-1}$ and CO_2/N_2 selectivity of 70 at 295 K. However, Gopalakrishnan et al. [101] stated that gas selectivity of membrane produced by the CVD method is much higher than that of membranes prepared by the sol-gel method. Li [102] stated that CVD is a reproducible method giving a defect free thin layer compared to the sol-gel method.

Chemical vapor deposition is “a process where gas phase molecules are decomposed in some manner to leave behind solid materials” [103]. In CVD, the reactants in the gas phase are simultaneously introduced into a preheated reaction chamber on the same or opposite sides of a substrate and reacted to form a permeable and selective solid layer [104,105,106,107]. The CVD has been successfully applied for the deposition of metal oxide or silica layers on the surface of porous and non-porous substrates [108,109,110,111,112]. Only few works report the deposition of amino-silica selective layers using the CVD method for the CO_2/CH_4 separation. Han et al. [113] deposited 3-aminopropylmethyldiethoxysilane by CVD on a ceramic support and obtained a CO_2 permeance of $3.7x10^{-8}$ mol $m^{-2}s^{-1}Pa^{-1}$ and CO_2/N_2 selectivity of 20 at 923 K.

1.4. Transport mechanism

Gas transport through a membrane depends on both membrane material and gas molecule chemical and physical properties. In porous membrane materials, various mechanisms may occur such as Knudsen diffusion, surface diffusion, gas-translational diffusion mechanisms [114]. However, in non-porous materials such as polymers, solution-diffusion is the main transport mechanism.

1.4.1 Knudsen diffusion

The Knudsen diffusion takes place when pore diameter is smaller than mean free path of the gas molecules. Gas molecules are transported while bumping on the pore wall (**Fig. 2**). The Knudsen permeance is presented by **Eq. (4)**.

$$\bar{P}_i = \frac{\varepsilon d_P}{\tau l}\left(\frac{8}{9\pi MRT}\right)^{1/2} \qquad \textbf{Eq. (4)}$$

where ε is the porosity of the membrane, τ the tortuosity of the membrane, M the gas molecular weight [g mol^{-1}], R the gas constant, d_p the pore diameter [nm], l the membrane thickness [m] and T the temperature [K].

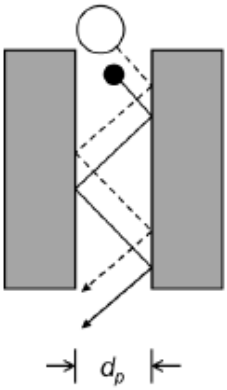

Fig. 2: Knudsen diffusion mechanism [114].

1.4.2 Surface diffusion or molecular sieving

Gas molecules are transported by surface diffusion at low temperatures when the interaction between the pore wall and gas molecules becomes strong compared to their kinetic energy. This mechanism becomes important with relatively small pores because of the relatively high proportion of surface area compared to pores volume (**Fig. 3**). In the surface diffusion mechanism, gas molecules adsorb onto the surface of the membrane at the pore entrance, diffuse through the membrane, and desorb at the pore exit. The mechanism can be expressed as follow:

$$\overline{P_{SD}} = \frac{\rho K_0 D_0}{l}\exp\left(\frac{\Delta H_a - \Delta E_{SD}}{RT}\right) \qquad \textbf{Eq. (5)}$$

where ρ is the gas density [kg m^{-3}], K_0 the adsorption equilibrium constant, D_0 the diffusion coefficient [m^2 s^{-1}], ΔH_a the enthalpy of adsorption [J mol^{-1}] and ΔE the energy barrier for gas molecule to move to other adsorption sites [J mol^{-1}], l the membrane thickness [m] and T the temperature [K].

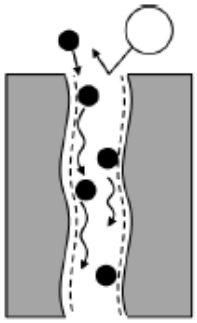

Fig. 3: Surface diffusion mechanism [114].

1.4.3 Gas-translational mechanism

The gas-translational mechanism occurs with condensable gas molecules in small pores. The diffusing gas molecules cannot totally escape the surface potential because of the small distance separating the pore walls (**Fig. 4**). The mechanism can be written as follow:

$$\overline{P_{GT}} = \frac{\varepsilon d_p \alpha_g}{\tau l}\left(\frac{8}{\pi T M R}\right)^{1/2} \exp\left(-\frac{\Delta E}{RT}\right) \qquad \textbf{Eq. (6)}$$

where ε represents the porosity, d_p the diameter of pores [m], τ the tortuosity, L the membrane thickness [m], α_g the probability of the velocity in the right direction [m s^{-1}], , and ΔE the energy barrier to be overcome [J mol^{-1}], M the gas molecule molecular weight [g mol^{-1}] and T the permeation temperature [K].

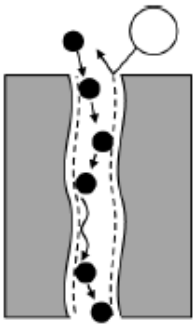

Fig. 4: Gas-translational mechanism [114]

1.4.4 Solution-diffusion

The solution-diffusion mechanism occurs in dense non-porous membranes such as polymeric membranes. Gases pass through dense membranes by sorption into the membrane surface, diffusion through the membrane and desorption at another site (**Fig. 5**). Therefore, permeance is the product of diffusivity (D) and solubility (S) of gases in the membrane normalized by membrane thickness as shown in **Eq. (7)**. Solubility coefficient is a thermodynamic parameter. It evaluates the amount of the penetrant gas sorbed by the membrane under equilibrium conditions. It is related with the condensability of the gas species and the interaction between the gas species and the membrane material. It depends on operating conditions (temperature, pressure, and composition). On the other hand, diffusion coefficient is a kinetic parameter which indicates how fast a penetrant gas is transported through the membrane. It depends on the gas species properties (size, shape, and polarity) and nature of the membrane (physical and chemical structure) [14].

$$\bar{P}_i = \frac{DS}{L} \qquad \textbf{Eq. (7)}$$

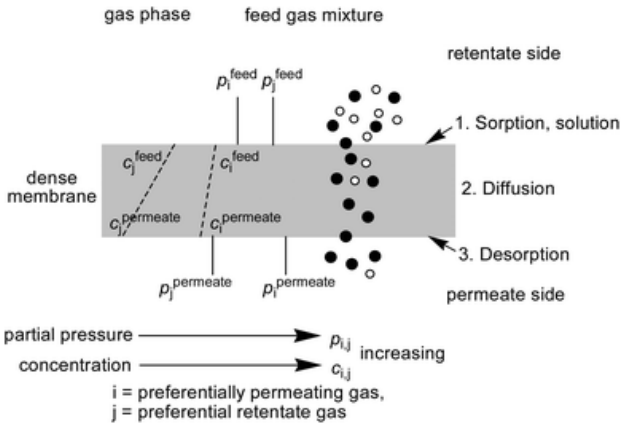

Fig. 5: Solution-diffusion mechanism [115].

1.4.5 Time-lag method

Solubility and diffusivity can be evaluated experimentally using the time-lag method [116]. The time-lag reflects the time that the gas takes to diffuse through a membrane and is inversely proportional to the gas diffusion coefficient. Experimentally, the time-lag can be estimated by first, purging both sides of the membrane using an inert gas, then, injecting a precise volume of the investigated gas to the surface of the membrane, after that, measuring the evolution of the permeated gas by the means of a thermal conductivity detector. The time delays resulting from the experimental set up are calibrated. It is the time the investigated gas will take to go from the tank to the surface of the membrane and from the permeation side to a detector. The expression for the permeance across a cylindrical body in a transient state is written as shown in **Eq. (8)** [117, 118]:

$$Q = \frac{2\pi\varepsilon L C_0 D_{eff}}{ln\left(\frac{r_c}{r_0}\right)} \left(t - \frac{r_0^2 - r_c^2 + (r_0^2 + r_c^2) ln\left(\frac{r_c}{r_0}\right)}{4 D_{eff} ln\left(\frac{r_c}{r_0}\right)} \right) \qquad \textbf{Eq. (8)}$$

where Q represents the total gas permeated [mol], t the time [s], ε the porosity, L the length of the cylinder [m], D_{eff} the effective diffusion coefficient [$m^2\ s^{-1}$], r_o the internal radius [m] and r_c the external radius [m].

The diffusion path is defined by the product of the outer radius (r_1) and the tortuosity (τ) of the membrane.

The concentration of dissolved gas,C_0, is given by Henry's law (**Eq. (9)**).

$$C_0 = SP$$ **Eq. (9)**

where S is the solubility of the gas in the liquid [mol $m^{-3}Pa^{-1}$].

The time-lag is measured when the concentration will reach a steady state. It can be estimated from the intercept on the time axis (**Eq. (10)**), while, the flux in the steady state flux is given by the slope of the asymptote, m_∞ (**Eq. (11)**).

$$t_{lag} = \frac{r_0^2 - r_c^2 + (r_0^2 + r_c^2)\ln\left(\frac{r_c}{r_0}\right)}{4D_{eff}\ln\left(\frac{r_c}{r_0}\right)}$$ **Eq. (10)**

$$m_\infty = \frac{2\pi\varepsilon L C_0 D_{eff}}{ln\left(\frac{r_c}{r_0}\right)}$$ **Eq. (11)**

From **Eq. (10)** and **Eq. (11)** the effective diffusion coefficient D_{eff} and solubility S can be re calculated (**Fig. 6**).

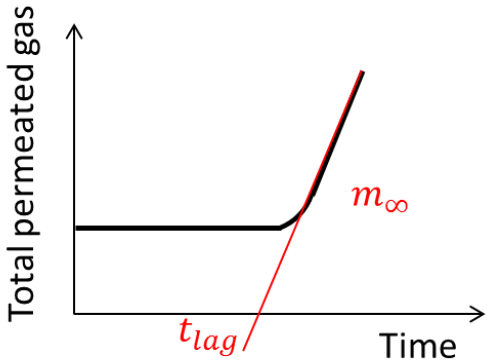

Fig. 6: Calculation of the effective diffusion coefficient and solubility using time-lag method

1.5. Robeson upper boundary

The Robeson upper boundary is an empirical correlation that relates the best permeability and selectivity values for polymer membranes, and serves as a goal for development of new

materials. However, the relationship has just been accepted as such, and it has been assumed that all points on the line are equally acceptable.

Extensive research has been carried out in the economical optimization of membrane processes. For example, Low et al. [119] investigated the performance of different polymeric membranes for the separation of CO_2 from flue gas based on the variation of the operational parameters such as the feed-to-permeate pressure ratio, the relative humidity, the temperature and the operational modes such as vacuum on the permeate side and/or compression on the feed, single or two-stage configurations. The study showed that for all cases higher CO_2 permeance led to lower required membrane area and higher CO_2/N_2 selectivity resulted in lower energy requirements for the separation. Ramasubramanian et al. [120] reported the effect of operating conditions and membrane price to the overall cost for separating CO_2 from post-combustion flue gases. A membrane with a CO_2 permeance of $9.9x10^{-7}$ mol $m^{-2}s^{-1}Pa^{-1}$ and a CO_2/N_2 selectivity of 140 operating at close to atmospheric pressure and using an air-sweep process can achieve a CO_2 recovery of 90% and a purity of 95% at a cost <\$24t^{-1} CO_2. Hinchliffe and Porter [121] used permeability and selectivity as parameters to economically optimize the separation of hydrogen and carbon monoxide through two commercially available membranes and compared the results with cryogenic flash distillation. The evaluation showed that membrane gas separation requires the optimization of the extent of separation. The minimum cost was found to be at a purity between 95 and 96% over a range of recovery between 85 and 97%. At the optimum separation conditions, the cost of separation was less than 60% that of cryogenic separation. Qi and Henson [122] considered the case of CO_2/CH_4 separation in spiral-wound permeators for natural gas treatment and oil recovery applications. The effects of the operating conditions, membrane properties, and economic parameters were investigated, and two different membrane configurations were considered for treating natural gas. A three-stage system with residue recycle was found to yield lower costs than a two-stage system with permeate recycle. Singh [123] optimized the cost of hydrogen extraction from multi-component mixtures in a membrane unit and investigated the influence of the membrane area, operating conditions and feed composition. The simulation assumed that the permeability of each component was the same as that of the pure species and was independent of pressure, as well as steady-state, plug flow, no concentration gradients, and uniformity of the membrane thickness. It was found that increases in the surface area of the membrane increased not only the degree of separation but also the

process cost. Several approaches to economic analysis of membranes have been described. For instance, Vareltzis et al. [124] reported the optimization of zeolite membranes by simulating the nonlinearity of the generalized Maxwell-Stefan distribution. Prasad et al. [125] stated that operating pressure is a key point in a membrane process. Increasing operating pressure can decrease the membrane area and increase product recovery. The objective of the simulation was to maximize purity and recovery while satisfying the constraints of the membrane. Mopharthi et al. [126] analyzed the economical viability of silica and palladium composite membrane reactors as dehydrogenation reactors. The analysis compared these reactors with conventional reactors and separators. Lim et al. [127] analyzed the general permeance requirement for a given diameter of membrane tube based on an empirical finding of sizes of chemical reactors. It was found that a permeance of 10^{-7} mol $m^{-2}s^{-1}Pa^{-1}$ was needed for commercial operation.

1.6. Research objectives and thesis overview

This work develops two types of hybrid membrane materials in an attempt to improve the separation of CO_2 from CH_4. First, organic groups (amine functional group) were incorporated into an inorganic matrix (silica). Then, an inorganic material (SAPO-34) was dispersed into an organic matrix (polyetherimide). Finally, optimum points within the Robeson upper boundary for various gas pairs were determined based on the cost of the membrane, the number of membrane units required to achieve a specific separation, and the compression requirements. .

The thesis is divided into 7 Chapters. **Chapter 1** gives an explanation about basic concepts, and introduces the background knowledge for this research. **Chapter 2** deals with the synthesis of amine-modified silica membranes in order to improve the CO_2/CH_4 separation. The work determines the chemical vapor deposition optimal conditions to synthesize hybrid silica membrane using 3-amino-propyltriethoxysilane and characterizes the obtained membranes. **Chapter 3** investigates two sorts of alkyl-amines and tries to understand the relationship between the micro-structure and the performance of the obtained hybrid membranes. **Chapter 4** studies the effect of the incorporation of different amount of CO_2 selective zeolite (SAPO-34) into thermo-stable polymeric matrix (polyetherimide) and attempts to improve zeolite dispersion into the polymeric matrix. **Chapter 5** gives an approach to determine optimal points within the Robeson upper boundary for four gas pairs: CO_2/N_2, O_2/N_2, CO_2/CH_4, and N_2/CH_4. Finally,

Chapter 6 provides conclusions of this work, and includes recommendations for future work on this topic.

1.7. References

[1] http://www.bp.com/content/dam/bp/pdf/Energy-economics/statistical-review-2014/BP-statistical-review-of-world-energy-2014-full-report.pdf

[2] "Kyoto Protocol to the United Nations Framework Convention on Climate Change: Annex B". United Nations Framework Convention on Climate Change. 2011.

[3] B. Shimekit, H. Mukhtar (2012). Natural Gas Purification Technologies - Major advances for CO_2 separation and future directions, Advances in Natural Gas Technology, Dr. Hamid Al-Megren (Ed.), ISBN: 978-953-51-0507-7, InTech, Available from: http://www.intechopen.com/books/advances-in-natural-gastechnology/ natural-gas-purification-technologies-major-advances-for-co2-separation-and-future-directions

[4] M.M. Foss, Interstate natural gas-quality specifications and interchangeability, Center for energy economics, the university of Texas at Austin, 2004.

[5] S. Sridhar, R.S. Veerapur, M.B. Patil, K.B. Gudasi, T.M. Aminabhavi, Matrimid polyimide membranes for the separation of carbon dioxide from methane, J. Appl. Polym. Sci. 106 (2007) 1585-1594.

[6] S. J. Khatib, S. T. Oyama, Silica membranes for hydrogen separation prepared by chemical vapor deposition (CVD), Sep. Purif. Technol. 111 (2013) 20-42.

[7] R.W. Baker, Future directions of membrane gas separation technology, Ind. Eng. Chem. Res. 41 (2002) 1393-1411.

[8] A. Kohl, R. Nielson, Gas purification, Gulf publishing company, fifth edition, 1997.

[9] A. Demirbas, Methane gas hydrate, Chapter 2. http://www.springer.com/978-1-84882-871-1

[10] D. D. Iarikov, P. Hacarlioglu, S. T. Oyama, Supported room temperature ionic liquid membranes for CO_2/CH_4 separation, Chem. Eng. J. 166 (2011) 401-406.

[11] R. Khalilpour, A. Abbas, Z. Lai, I. Pinnau, Analysis of hollow fiber membrane systems for multicomponent gas separation, Chem. Eng. Res. Des. 91 (2013) 332-347.

[12] W.J. Koros, R. Mahajan, Pushing the limits on possibilities for large-scale gas separation: which strategies? J. Membr. Sci. 175 (2000) 181-196.

[13] A. C. Lua, Y. Shen. Preparation and characterization of polyimide–silica composite membranes and their derived carbon–silica composite membranes for gas separation. Chem. Eng. J. 220 (2013) 441–451.

[14] M. Mulder, Basic principles of membrane technology, Kluwer Academic Publishers, 2nd edition, 1997, Dordrecht.

[15] T.T. Moore, S. Damle, D. Wallace, W.J. Koros, The engineering handbook, 2nd edition, CRC Press LLC, 2005.

[16] T.T. Moore, Effects of materials, processing, and operating conditions on the morphology and gas transport properties of mixed matrix membranes", PhD Thesis, The University of Texas at Austin, December 2004.

[17] L.M. Robeson, Correlation of separation factor versus permeability for polymeric membranes, J. Membr. Sci. 62 (1991) 165-185.

[18] L.M. Robeson, The upper bound revisited, J. Membr. Sci. 320 (2008) 390-400.
[19] D.D. Iarikov, S. T. Oyama, Review of CO_2/CH_4 Separation Membranes, in S.T.Oyama, S.M. Stagg-Williams (Eds.) Inorganic, polymeric, and composite membranes: Structure-function and other correlations, Elsevier, Amsterdam, 2011.
[20] V. Abetz, T. Brinkmann, M. Dijkstra, K. Ebert, D. Fritsch, K. Ohlrogge, Developments in membrane research: From material via process design to industrial application, Adv. Eng. Mater. 8 (2006) 328-358.
[21] J. Huang, J. Zou, W.S. Winston Ho, Carbon dioxide capture using a CO_2-selective facilitated transport membrane, Ind. Eng. Chem. Res. 47 (2008) 1261-1267.
[22] L. A.El-Azzami, E.A. Grulke, Parametric study of CO_2 fixed carrier facilitated transport through swollen chitosan membranes, Ind. Eng. Chem. Res. 48 (2009) 894-902.
[23] R.Yegani, H. Hirozawa, M. Teramoto, H. Himei, O. Okada, T. Takigawa, N. Ohmura, N. Matsumiya, H. Matsuyama, Selective separation of CO_2 by using novel facilitated transport membrane at elevated temperatures and pressures, J. Membr. Sci. 291 (2007) 157-164.
[24] S. Hanioka, T. Maruyama, T. Sotani, M. Teramoto, H. Matsuyama, K. Nakashima, M. Hanaki, F. Kubota, M. Goto, CO_2 separation facilitated by task-specific ionic liquids using a supported liquid membrane, J. Membr. Sci. 314 (2008) 1-4.
[25] T. Kai, T. Kouketsu, S. Duan, S. Kazama, K. Yamada, Development of commercial-sized dendrimer composite membrane modules for CO_2 removal from flue gas, Sep. Purif. Technol. 63 (2008) 524-530.
[26] Y. Cui, H. Kita, K.-I. Okamoto, Preparation and gas separation performance of zeolite T membrane, J. Mater. Chem. 14 (2004) 924-932.
[27] A.B. Shelekhin, A.G. Dixon and Y.H. Ma, Adsorption, permeation, and diffusion of gases in microporous membranes. II. Permeation of gases in microporous glass membranes, J. Membr. Sci., 15 (1992) 233-244
[28] Y. Zhang, J. Sunarso, S. Liu, R. Wang, Current status and development of membranes for CO_2/CH_4 separation: A review, Int. J. Greenh. Gas Control 12 (2013) 84–107.
[29] J.L. Li, B.H. Chen, Review of CO_2 absorption using chemical solvents in hollow fiber membrane contactors, Sep. Purif. Technol. 41(2005) 109–122.
[30] S. Li, J.L. Falconer, R.D. Noble, SAPO-34 membranes for CO_2/CH_4 separations: Effect of Si/Al ratio. Micropor. Mesopor. Mater., 110 (2008) 310-317.
[31] S. Li, M.A. Carreon, Y. Zhang, H.M. Funke,R.D. Noble, J.L. Falconer, Scale-up of SAPO-34 membranes for CO_2/CH_4 separation, J. Membr. Sci. 352 (2010) 7-13.
[32] J.C. Poshusta, R.D. Noble, J.L. Falconer, Characterization and permeation properties of zsm-5 tubular membranes, J. Membr. Sci. 160, 1 (1999) 1797-1812.
[33] T. Tomita, K. Nakayama, H. Sasaki, Gas separation characteristics of DDR type zeolite membrane, Micropor. Mesopor. Mater. 68 (2004)71-75.
[34] J. Lindmark, J. Hedlund, Carbon dioxide removal from synthesis gas using MFI membranes. J. Membr. Sci., 360 (2010) 284-291.
[35] L.J.P. van den Broeke, F. Kapteijn, J.A. Moulijn, Transport and separation properties of a silicalite-1 membrane-II. Variable separation factor, Chem. Eng. Sci. 54 (1999) 259–269.
[36] T. Yamaguchi, T. Niitsuma, B.N. Nair, K. Nakagawa, Lithium silicate based membranes for high temperature CO_2 separation. J. Membr. Sci., 294 (2007) 16-21.
[37] N.K. Raman, C.J. Brinker, Organic "template" approach to molecular sieving silica membranes. J. Membr. Sci., 105 (1995) 273-279.

[38] B.-K. Sea, K. Kusakabe, S. Morooka, Pore size control and gas permeation kinetics of silica membranes by pyrolysis of phenyl-substituted ethoxysilanes with cross-flow through a porous support wall. J. Membr. Sci., 130 (1997) 41-52.
[39] G. Xomeritakis, C.Y. Tsai, Y.B. Jiang, C.J. Brinker, Tubular ceramic-supported sol–gel silica-based membranes for flue gas carbon dioxide capture and sequestration. J. Membr. Sci. 341 (2009) 30-36.
[40] B. Belaissaoui. E. Favre, Membrane separation processes for post-combustion carbon dioxide capture: State of the art and critical overview, Oil & Gas Science and Technology – Rev. IFP Energies nouvelles (2013). DOI: 10.2516/ogst/2013163
[41] W. J. Koros, Gas separation membranes: Needs for combined materials science and processing approaches, Macromol. Symp., 188 (2002)13-22.
[42] E.V. Perez, K.J. Balkus Jr., J.P. Ferraris, I.H. Musselman, Mixed-matrix membranes containing MOF-5 for gas separations, J. Membr. Sci. 328 (2009) 165-173.
[43] G. Dong, H. Li, and V. Chen, Challenges and opportunities for mixed-matrix membranes for gas separation, J. Mater. Chem. A 1 (2013) 4610-4630.
[44] D. D'Alessandro, B. Smit and J. Long, Carbon dioxide capture: prospects for new materials, Angew. Chem., Int. Ed. 49 (2010) 6058-6082.
[45] P. L. Llewellyn, S. Bourrelly, C. Serre, A. Vimont, M. Daturi, L. Hamon, G. De Weireld, J.-S. Chang, D.-Y. Hong, Y. Kyu Hwang, S. Hwa Jhung and G. Ferey, High uptakes of CO_2 and CH_4 in mesoporous metal—organic frameworks MIL-100 and MIL-101, Langmuir, 24 (2008) 7245-7250.
[46] Y. Li, F. Liang, H. Bux, W. Yang and J. Caro, Zeolitic imidazolate framework ZIF-7 based molecular sieve membrane for hydrogen separation, J. Membr. Sci., 453 (2010) 48-54.
[47] R. Adams, C. Carson, J. Ward, R. Tannenbaum and W. Koros, Metal organic framework mixed matrix membranes for gas separations, Microporous Mesoporous Mater., 2010, 131, 13–20.
[48] S. Kim, T. W. Pechar and E. Marand, Poly(imide siloxane) and Carbon Nanotube Mixed Matrix Membranes for Gas Separation, Desalination 192 (2006) 330-339.
[49] T. C. Merkel, B. D. Freeman, R. J. Spontak, Z. He, I. Pinnau, P. Meakin and A. J. Hill, Ultrapermeable, reverse-selective nanocomposite membranes, Science 296 (2002) 519-522.
[50] A. I. Skoulidas and D. S. Sholl, Self-diffusion and transport diffusion of light gases in metal-organic framework materials assessed using molecular dynamics simulations, J. Phys. Chem. B 109 (2005) 15760-15768.
[51] G. Clarizia, C. Algieri and E. Drioli, Filler-polymer combination: a route to modify gas transport properties of a polymeric membrane, Polymer 45 (2004) 5671-5681.
[52] C.A. Scholes, S.E. Kentish, G.W. Stevens, Carbon dioxide separation through polymeric membrane systems for flue gas applications, Rec. Pat. Chem. Eng. 1 (2008) 52–66.
[53] Y. Zhang, K.J. Balkus Jr., I.H. Musselman, J.P. Ferraris, Mixed-matrix membranes composed of Matrimid® and mesoporous ZSM-5 nanoparticles, J. Membr. Sci. 325 (2008) 28-39.
[54] S.S. Hosseini, Y. Li, T. Chung, Y. Liu, Enhanced gas separation performance of nanocomposite membranes using MgO nanoparticles, J. Membr. Sci. 302 (2007) 207-217.
[55] M. Sadeghi, M.A. Semsarzadeh, H. Moadel, Enhancement of the gas separation properties of polybenzimidazole (PBI) membrane by incorporation of silica nano particles, J. Membr. Sci. 331 (2009) 21-30.

[56] V.C. Souza, M.G.N. Quadri, Organic-inorganic hybrid membranes in separation processes: a 10-year review, Braz. J. Chem. Eng. 30 (2013) 683 – 700.
[57] C. Guizard, A. Bac, M. Barboiu, N. Hovnanian, Hybrid organic-inorganic membranes with specific transport properties: Applications in separation and sensors technologies, Sep. Purif. Technol. 25 (2001) 167–180.
[58] M.R. Coleman, W.J. Koros, Transport properties of polyimide isomers containing hexafluoroisopropylidene in the diamine residue. J. Polym. Sci., Part B: Polym. Phys. 32 (1994) 1915–1926.
[59] A.M.W. Hillock, S.J. Miller, W.J. Koros, Crosslinked mixed matrix membranes for the purification of natural gas: effects of sieve surface modification. J. Membr. Sci. 314 (2008) 193–199.
[60] T.T. Moore, W.J. Koros, Non-ideal effects in organic-inorganic materials for gas separation membranes, J. Mol. Struct. 739 (2005) 87–98.
[61] R. Mahajan, W.J. Koros, Factors controlling successful formation of mixed matrix gas separation materials. Ind. Eng. Chem. Res. 39 (2000) 2692–2696.
[62] R. Mahajan, W.J. Koros, Mixed matrix membrane materials with glassy polymers. Part 1, Polym. Eng. Sci. 42 (2002) 1420–1431.
[63] R. Mahajan, W.J. Koros, Mixed matrix membrane materials with glassy polymers. Part 2, Polym. Eng. Sci. 42 (2002) 1432–1441.
[64] R. Mahajan, R. Burns, M. Schaeffer, W.J. Koros, Challenges in forming successful mixed matrix membranes with rigid polymeric materials. J. Appl. Polym. Sci. 86 (2002) 881–890.
[65] C. Hibshman, C.J. Cornelius, E. Marand, The gas separation effects of annealing polyimide–organosilicate hybrid membranes. J. Membr. Sci. 211 (2003)25–40.
[66] I.F.J. Vankelecom, S. VandenBroeck, E. Merckx, H. Geerts, P. Grobet, J.B. Uytterhoeven, Silylation to improve incorporation of zeolites in polyimide films. J. Phys. Chem. 100 (1996) 3753–3758.
[67] W. N. W. Salleh, A. F. Ismail, T. Matsuura,M. S. Abdullah. Precursor selection and process conditions in the preparation of carbon membrane for gas separation: A Review. Sep. Purif. Rev. 40 (2011) 261–311.
[68] S.M. Saufi, A.F. Ismail, Fabrication of carbon membranes for gas separation-A review. Carbon. 42(2004)241–259.
[69] P.S. Tin, T.S.Chung, A.J. Hill. Advanced fabrication of carbon molecular sieve membranes by nonsolvent pretreatment of precursor polymers. Ind. Eng. Chem. Res.. 43(2004)6476–6483.
[70] (a) A.C. Lua, J. Su. Effects of carbonization on pore evolution and gas permeation properties of carbon membranes from kapton polyimide. Carbon. 44(2006)2964–2972.
(b) E.P. Favvas, E.P. Kouvelos, G.E. Romanos, G.I. Pilatos, A.C. Mitropoulos, N.K. Kanellopoulos. Characterization of highly selective microporous carbon hollow fiber membranes prepared from a commercial co-polyimide precursor. J. Porous Mat., 15(2008)625–633.
[71] (a) A.B. Fuertes, T.A. Centeno. Preparation of supported asymmetric carbon molecular sieve membranes. J. Membr. Sci., 144(1998)105–111.
(b) M.G. Sedigh, L. Xu, T.T.Tsotsis, M. Sahimi, Transport and morphological characteristics of polyetherimide-based carbon molecular sieve membranes. Ind. Eng. Chem. Res., 38(1999)3367–3380.

(c) M.G. Sedigh, M. Jahangiri, P.K.T. Liu, M. Sahimiand, T.T. Tsotsis. Structural characterization of polyetherimide-based carbon molecular sieve membranes. AIChE J., 46(2000) 2245–2255.

(d) E.B. Coutinho, V.M.M. Salim, C.P. Borges. Preparation of carbon hollow fibermembranes by pyrolysis of polyetherimide. Carbon, 41(2003)1707–1714.

(e) P.S. Rao, M.Y. Wey, H.H.Tseng, I.A. Kumar, T.H. Weng. A comparison of carbon/nanotube molecular sieve membranes with polymer blend carbon molecular sieve membranes for the gas permeation application. Microp. Mesop. Mat., 113(2008) 499–510.

[72] (a) A.B. Fuertes, I. Menendez. separation of hydrocarbon gas mixtures using phenolic resin-based carbon membranes. Sep. Purif. Technol., 28(2002)29–41.

(b) T.A., Centeno, J.L. Vilas, A.B. Fuertes. Effects of phenolic resin pyrolysis conditions on carbon membrane performance for gas separation. J. Membr. Sci., 228(2004)45–54.

[73] B. Zhang, T.Wang, S.L. Liu, S.Zhang, J.Qiu, Z.Chen. Structure and morphology of microporous carbon membrane materials derived from poly (phthalazinone ether sulfoneketone). Microporous Mesoporous Mater. 96 (2006)79–83.

[74] Z. Huang, F. Kang, W. Huang, J. Yang, K. Liang, M. Cui. Pore structure and fractal characteristics of activated carbon fibers characterized by using HRTEM. J Colloid Interface Sci. 249 (2002)453–7.

[75] M.Shiflett, H. Foley. Ultrasonic deposition of highselectivity nanoporous carbon membranes. Science 285(1999)5.

[76] W. Zhou, M . Yoshino, H . Kita, K. Okamoto. Preparation and gas permeation properties of carbon molecular sieve membranes based on sulfonated phenolic resin. J Membr Sci 217(2003)55–67.

[77] C. Song, T. Wang, H. Jiang, X. Wang, Y. Cao, J. Qiu. Gas separation performance of C/CMS membranes derived from poly(furfuryl alcohol) (PFA) with different chemical structure. J Membr Sci. 361(2010)1–2.

[78] L. Li, T. Wang, Q. Liu, Y. Cao, J. Qiu. A high CO_2 permselective mesoporous silica/carbon composite membrane for CO_2 separation. Carbon. 50(2012)5186-5195.

[79] G. Li, J. Yang, J. Wang, W. Xiao, L. Zhou, Y. Zhang, J. Lu, D. Yin. Thin carbon/SAPO-34 microporous composite membranes for gas separation. J. Membr. Sci. 374 (2011) 83–92.

[80] X. Yin, J. Wang, N. Chu, J. Yang, J. Lu, Y. Zhang, D. Yin. Zeolite L/carbon nanocomposite membranes on the porous alumina tubes and their gas separation properties. J. Membr. Sci. 348 (2010) 181–189.

[81] J.A. Lie, M.B. Hagg. Carbon membranes from cellulose and metal loaded cellulose. Carbon. 43 (12) (2005) 2600.

[82] M. Smaïhi, T. Jermoumi, J. Marignan, R.D. Noble, Organic-inorganic gas separation membranes: preparation and characterization, J. Membr. Sci. 116 (1996) 211-220.

[83] T. Okui, Y. Saito, T. Okubo, M. Sadakata, Gas permeation of porous organic/inorganic hybrid membranes, J. Sol-Gel Sci. Technol. 5 (1995) 127-134.

[84] B.A. McCool, W.J. DeSisto, Amino-functionalized silica membranes for enhanced carbon dioxide permeation, Adv. Funct. Mater. 15 (2005) 1635-1640.

[85] N. Hiyoshi, K. Yogo, T. Yashima, Adsorption characteristics of carbon dioxide on organically functionalized SBA-15, Microporous Mesoporous Mater. 84 (2005) 357365.

[86] E.L. Cussler, R. Aris, A. Bhown, On the limits of facilitated diffusion, J. Membr. Sci. 43 (1989) 149-164.

[87] O. Leal, C. Bolívara, C. Ovalles, J.J. García, Y. Espidel, Reversible adsorption of carbon dioxide on amine surface-bonded silica gel, Inorg. Chim. Acta. 240 (1995) 183-189.
[88] M. Rocchia, E. Garrone, F. Geobaldo, L. Boarino, M. J. Sailor, Sensing CO_2 in a chemically modified porous silicon film, Phys. Status Solidi A: Applications and Materials Science. 197 (2003) 365-369.
[89] M. Ostwal, R.P. Singh, S.F. Dec, M.T. Lusk, J.D. Way, 3- Aminopropyltriethoxysilane functionalized inorganic membranes for high temperature CO_2/N_2 separation, J. Membr. Sci. 369 (2011) 139–147.
[90] C.A. Scholes, S.E. Kentish, G.W. Stevens, Carbon dioxide separation through polymeric membrane systems for flue gas applications, Recent Pat. Chem. Eng. 1 (2008) 52–66.
[91] R. Xing, W.S.W. Ho, Crosslinked polyvinylalcohol-polysiloxane/fumed silica mixed matrix membranes containing amines for CO_2/H_2 separation, J. Membr. Sci. 367 (2011) 91–102.
[92] Y. Sakamoto, K. Nagata, K. Yogo, K. Yamada, Preparation and CO_2 separation properties of amine-modified mesoporous silica membranes, Microporous Mesoporous Mater. 101 (2007) 303-311.
[93] G. Xomeritakis, Y.C. Tsai, C.J. Brinker, Microporous sol–gel derived aminosilicate membrane for enhanced carbon dioxide separation, Sep. Purif. Technol. 42 (2005) 249-257.
[94] S.H. Hyun, S.Y. Jo, B.S. Kang. Surface modification of ϒ-alumina membranes by silane coupling for CO_2 separation. J. Membr. Sci 120 (2) (1996) 197.
[95] B.S. Kang, S.H. Hyun. ϒ-Alumina composite membranes modified with microporous silica for CO_2 separation. J. Mater. Sci. 34(6) (1999) 1391.
[96] H.Z. Chen, T.S. Chung. CO_2-selective membranes for hydrogen purification and the effect of carbon monoxide (CO) on its gas separation performance. Int. J. Hydrogen Energ. 37 (2012) 6001-6011.
[97] M.L. Chua, L. Shao, B.T. Low, Y. Xiao, T.S. Chung. Polyetheramine–polyhedral oligomeric silsesquioxane organic–inorganic hybrid membranes for CO_2/H_2 and CO_2/N_2 separation. J. Membr. Sci. 385- 386 (2011) 40-48.
[98] P. Innocenzi, V.G. Kessler, Sol-gel methods for materials processing: focusing on materials for pollution control, water purification, and soil remediation, Springer, Ukraine, 2007.
[99] G.G. Paradis, R. Kreiter, M.M.A. van Tuel, A. Nijmeijer, and J.F. Vente, Amino-functionalized microporous hybrid silica membranes, J. Mater. Chem., 22 (2012) 7258 – 7264.
[100] G. Xomeritakis, C.Y. Tsai, C.J. Brinke, Microporous sol–gel derived aminosilicate membrane for enhanced carbon dioxide separation Sep. Purif. Technol. 42 (2005) 249–257.
[101] S. Gopalakrishnan, Y. Yoshino,M. Nomura, B.N. Nair, S. Nakao, A hybrid processing method for high performance hydrogen-selective silica membranes, J. Membr. Sci. 297 (2007) 5-9.
[102] K. Li, Ceramic membranes for separation and reaction, John Wiley & Sons, England, 2007.
[103] J. M. Jasinski, B. S. Meyerson, and B. A. Scott, Mechanistic studies of chemical vapor deposition, Ann. Rev. Phys. Chern. 38 (1987) 109-40.
[104] D. Koutsonikolas, S. Kaldis, G.P. Sakellaropoulos, A low-temperature CVI method for pore modification of sol–gel silica membranes, J. Membr. Sci. 342 (2009) 131–137.
[105] M. Tsapatsis, G. Gavalas, Structure and aging characteristics of H_2- permselective SiO_2-Vycor membranes, J. Membr. Sci. 87 (1994) 281–296.

[106] A. Nijmeijer, B.J. Bladergroen, H. Verweij, Low-temperature CVI modification of c-alumina membranes, Microporous Mesoporous Mater. 25 (1998) 179–184.
[107] B.K. Sea, M. Watanabe, K. Kusakabe, S. Morooka, S.-S. Kim, Formation of hydrogen permselective silica membrane for elevated temperature hydrogen recovery from a mixture containing steam, Gas Sep. Purif. 10 (1996) 187–195.
[108] M. Pan, C. Cooper, Y.S. Lin, G.Y. Meng, CVD modification and vapor/gas separation properties of nanoporous alumina membranes, J. Membr. Sci., 158 (1999), pp. 235–241.
[109] T. Ivanova, M. Surtchev, K. Gesheva, Investigation of CVD molybdenum oxide film, Mater. Lett., 53 (2002) 250–257.
[110] S. Mathur, P. Kuhn. CVD of titanium oxide coatings: comparative evaluation of thermal and plasma assisted processes, Surf. Coat. Technol., 201 (2006) 807–814.
[111] N. Jin, Y. Yang, X. Luo, Z. Xia. Development of CVD Ti-containing films, Prog. Mater Sci., 58 (2013) 1490–1533.
[112] Z. Dimitrova, D. Gogova, On the structure, stress and optical properties of CVD tungsten oxide films, MRS Bull., 40 (2005) 333–340.
[113] H.H. Han, S.H. Ryu, S. Nakao, Y.T.Lee, Gas permeation properties and preparation of porous ceramic membrane by CVD method using siloxane compounds, J. Membr. Sci. 431 (2013) 72–78
[114] S.T. Oyama, M. Yamada, T. Sugawara, A. Takagaki, R. Kikuchi, Review on mechanisms of gas permeation through inorganic membranes, J. Jpn. Pet. Inst. 54 (2011) 298-309.
[115] H.B.T. Jeazet, C. Staudt, and C. Janiak, Metal–organic frameworks in mixed-matrix membranes for gas separation, Dalton Trans. 41 (2012) 14003–14027.
[116] H.A. Daynes, The process of diffusion through a rubber membrane, Proc. R. Soc. Lond. A 97 (1920) 286-307.
[117] R. Ash, R.M. Barrer, D.G. Palmer, Diffusional conductances and time-lags in laminated hollow cylinders, Trans. Faraday Soc. 65 (1969) 121-130.
[118] J.R. Phillips, B.F. Dodge, Concentration-dependant time-lag measurements, AIChE J. 14 (1968) 392-397.
[119] B.T. Low, L. Zhao, T.C. Merkel, M. Weber, D. Stolten, A parametric study of the impact of membrane materials and process operating conditions on carbon capture from humidified flue gas. J. Membr. Sci. 431 (2013) 139-155.
[120] K. Ramasubramanian, H. Verweij, W.S.W. Ho, Membrane processes for carbon capture from coal-fired power plant flue gas: a modeling and cost study. J. Membr. Sci. 421-422 (2012) 299-310.
[121] A.B. Hinchliffe, K.E. Porter, Gas separation using membranes. 1. Optimization of the separation process using new cost parameters. Ind. Eng. Chem. Res. 36 (1997) 821-829.
[122] R. Qi, M.A. Henson, Optimization-based design of spiral-wound membrane systems for CO_2/CH_4 separations. Sep. Purif. Technol. 13 (1998) 209-225.
[123] B. Singh, A theoretical model for cost optimization of multicomponent mixtures across membranes in a permeation unit. 2nd International Conference on Environmental Science and Technology IPCBEE vol.6, IACSIT Press: Singapore, 2011.
[124] P. Vareltzis, E.S. Kikkinides, M.C. Grorgiadis, On the optimization of gas separation process using zeolite membrane. Trans IChemE. 81 (2003) 525-536.
[125] R. Prasad, R. L. Shaner, K. J. Doshi, Comparison of membranes with other gas separation technologies, in: D.R. Paul, Y.P. Yampolskii. Polymeric gas separation membranes, CRC Press:

Boca Raton, 1994, 514.
[126] A. Moparthi, R. Uppaluri, B.S. Gill, Economic feasibility of silica and palladium composite membranes for industrial dehydrogenation reactions. Chem. Eng. Res. Des. 83 (2010) 1088-1101.
[127] H. Lim, Y. Gu, S. T. Oyama, Studies of the effect of pressure and hydrogen permeance on the ethanol steam reforming reaction with palladium and silica-based membranes. J. Membr. Sci. 396 (2012) 119-127.

Chapter 2: Development of Amino-Silica Hybrid Membranes for CO_2/CH_4 Separation Using 3-Aminopropyltriethoxysilane

This Chapter is a modified version of a paper published in the Journal of Membrane Science:

S. Suzuki, S. Belhaj Messaoud, A. Takagaki, T. Sugawara, R. Kikuchi, S.T. Oyama, Development of inorganic-organic hybrid membranes for carbon dioxide/methane separation, J. Membr. Sci. 471 (2014) 402–411.

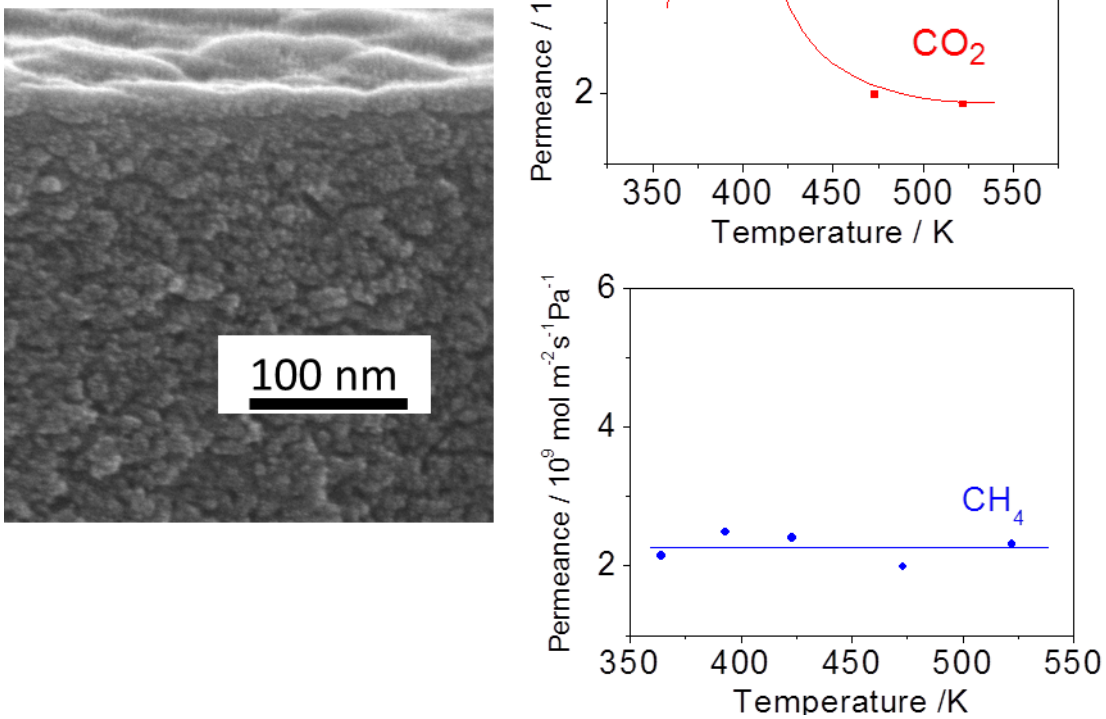

Overview

In this chapter inorganic-organic hybrid membranes were prepared employing tetraethylorthosilicate and 3-aminopropyltriethoxysilane as silica and amino-silica precursors. They were deposited on the surface of a porous alumina support at high temperature using oxygen as a co-reagent. The selective layer was coated using chemical vapor deposition at atmospheric pressure. The objective was to enhance the permeance of CO_2 by placing amine groups on the surface of the membrane. The amino-silica ratio (R) was varied from 0 to 100% in order to find an optimum composition for the separation of the CO_2 from CH_4. The best membrane was found to have a ratio R of 20% with a CO_2 permeance of 2.3×10^{-7} mol $m^{-2}s^{-1}Pa^{-1}$ and an ideal CO_2/CH_4 selectivity of 40 at 393 K and 0.10 MPa of partial pressure difference. The transport mechanism for CO_2 permeation was surface diffusion and for CH_4 passage was gas-translation. The pore size of the membrane was evaluated by Tsuru's method revealing a pore size of 0.44 nm. The results are significant because the permeance level is above that necessary for commercial use, the selectivity is adequate to produce a pipeline quality natural gas (purity > 2.4%), and the permeating gas is CO_2 which allows retention of methane at high pressure.

2.1 Experimental

2.1.1 Materials

Porous alumina tubes were obtained from the Pall Corporation and were employed as supports. The tubes had an outside diameter of 10 mm and a thickness of 1 mm. The support had a multilayered structure, with the outermost layer having an average pore size of size 5 nm. Glass joints were made from glass powder bought from the Nippon Electric Glass Co., Ltd and were used to attach the membrane support to dense alumina tubes. The glass joints required heating to 1273 K for 10 min using heating and cooling rates of 5 K min^{-1}. Aluminum isopropoxide (AIP, Sigma Aldrich, ≥ 98.0%), acetic acid (CH_3COOH, Wako, 60.0 ~ 61.0%) and nitric acid (HNO_3, Wako, 95.0%) were purchased from Tokyo Chemical Industry and poly(vinyl alcohol) (PVA, Wako, 99.7 mole% hydrolyzed, M. W. ~ 78,000) was procured from Poly sciences Inc. They were used for the preparation of boehmite sols. Tetraethyl orthosilicate (TEOS, TCI, ≥ 96.0%) and 3-Aminopropyltriethoxysilane (APTES, Sigma Aldrich, ≥ 98.0%) were supplied from Tokyo Chemical Industry and were used as silica and amino-silica

precursors, respectively. Pure Ar, He, O_2, CH_4, CO_2, N_2 and H_2 gases with a purity of 99.9% were acquired from Tokyo Koatsu Yamazaki Co., Ltd.

2.1.2 Membrane synthesis

2.1.2.1 Intermediate layers preparation

Two intermediate γ–Al_2O_3 layers were placed on the support through a sol-gel process by sequential dip-coating and calcination of a series of boehmite (AlOOH) sols of two different particle sizes to produce a uniform and defect free membrane surface. The sol-gel procedure was similar to that described previously by the group of Oyama [1, 2]. The sizes of the sol particles were tuned by precisely adjusting the synthesis parameters including the type and concentration of the acid. First, 0.13 mol of AIP was added to distilled water at 365 K and was stirred for 24 or 96 hours. Subsequently, CH_3COOH or HNO_3 was added to the solution to obtain small or large particle sizes, respectively. The ratios of H^+/alkoxide were adjusted to 0.10 and 1.50, respectively, and the solutions were refluxed at 365 K for 24 h. The prepared sols were then cooled to room temperature. Two boehmite sols with mean particle sizes of 40 and 100 nm were obtained. Dilute dipping solutions were prepared by mixing the boehmite sols with a PVA solution and distilled water to obtain a 0.15 M concentration of the sol and a 0.35 wt% concentration of the PVA. The alumina support was wrapped with Teflon tape and then dipped into the solution for 10 s. The alumina particles were deposited inside the tube, dried in air for 24 h and calcined by heating to 923 K for 3 h. The heating and the cooling rate was 1 K min^{-1}. The dipping-calcining cycle was repeated two times using large (100 nm) and small (40 nm) sol particle sizes.

2.1.2.2 Selective layer preparation

After the placement of the γ–Al_2O_3 intermediate layers on the support, a thin amino-silica film was deposited by CVD [3]. The streams of the reactants TEOS, APTES, and oxygen were introduced on the inner side of the tubular membrane, with the liquid silicates supplied with bubblers. The experimental set up is shown in **Fig. 7**. Argon was used as carrier in the inner side of the membrane and as balance gas in the outside, and its flow rate was adjusted to be the same to equalize the pressure on both sides. The delivery rate of the silicate and the amino-silicate precursors were altered by controlling their respective bubbler temperatures. The lines from the

bubbler exit to the reactor entrance were kept at 408 K with ribbon heaters to prevent condensation of the reactants. After heating the furnace to 673 K at a heating rate of 1 K min^{-1}, the carrier was introduced through two bubblers, then, premixed with O_2 at the entrance of the membranes. The total molar flow rate of the silica precursor was constant for all experiments and the CVD was carried out at atmospheric pressure. The CVD conditions are summarized **Table 2** .

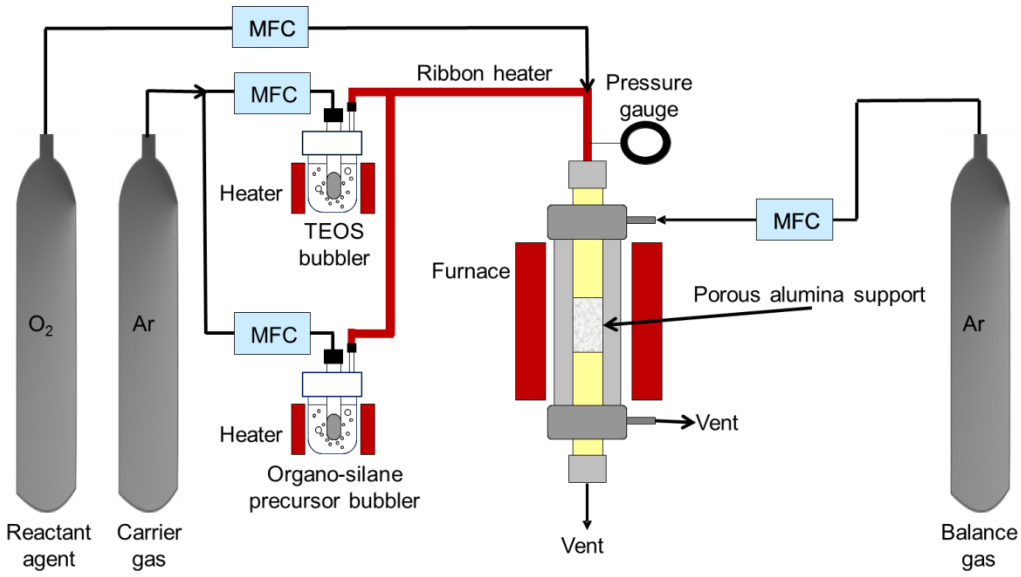

Fig. 7: Topmost layer deposition experimental set up.

Table 2: Chemical Vapor Deposition conditions with varying ratios of APTES and TEOS

CVD parameter	**Amount**
Total silica precursor	4.3 µmol/s
Reaction agent	8.0 µmol/s
Membrane inside	56 µmol/s
Balance gas (Ar)	56 µmol/s
APTES/(APTES+TEOS)	0 ~ 100%
CVD temperature	673 K

2.2 Characterization techniques

The particle size of the prepared boehmite sols was measured by a dynamic light scattering analyzer (Horiba Model LB-550). The gas permeance measurements were conducted

at 393 K before and after CVD by introducing a single gas to the inner side of the membrane. The flow rate of the permeating gases were measured using a flow meter (Agilent Technologies, AD1000). For permeances under 10^{-9} mol $m^{-2}s^{-1}Pa^{-1}$, the composition of the permeate stream was determined by a gas chromatograph (GC, Shimadzu, TCD, GC-8A) equipped with a thermal conductivity detector. The morphology of the membranes was obtained using a field emission scanning electron microscope (FE-SEM, Hitachi S-900). Samples were prepared by mechanically breaking the membranes into small pieces after cooling with liquid nitrogen. Samples were coated with a layer of Pt-Pd by ion sputtering (E-1030, Hitachi) with a current of 15 mA for 15 s before the observation of the cross section and the surface of the membranes. The presence of amine groups in the surface region was determined by X-ray photoelectron spectroscopy (XPS, PHI5000 VersaProbe, ULVAC Phi). Spectra were acquired using a monochromatic Al Kα source operated at 23.5 kV under charge neutralization using an Ar ion gun. Samples for XPS measurements were obtained in the same manner as for the SEM measurements.

2.3 Permeation measurements

The permeances of various gases (CH_4, CO_2, N_2 and H_2) were measured separately, and were repeated at least three times. The permeance and the ideal selectivity were calculated using **Eq. (1)** and **Eq. (2)** explained in **Chapter 1**.

2.4 Results and discussion

2.2.1 Permeation properties

Membranes were prepared with different ratios R of $\frac{APTES}{APTES+TEOS}$ from 0 to 100%. Permeances of CO_2 and CH_4 and CO_2/CH_4 selectivity are displayed as a function of this ratio in **Fig. 8**. The conditions were a temperature of 393 K and 0.10 MPa of partial pressure difference. For the membrane with only TEOS (R= 0%), the permeances of the gases decreased rapidly with increasing deposition time of the silica layer to 1.5 h, while the selectivity remained unchanged. For the membranes with mixed APTES and TEOS (R from 1 to 40%), the behavior was similar, with the permeances of CO_2 and CH_4 both decreasing with CVD deposition time, but with that of CH_4 decreasing more. It is likely that the formation of the amino-silica layer resulted in reduced pore sizes, decreasing both permeances, but in the case of CO_2, amine groups in close proximity

enhanced permeation and the ideal selectivity increased. The reason for low separation performance is the formation of a dense silica network and small pores. The highest selectivity was obtained at R= 20%. For each membrane having R between 1 and 40%, the highest selectivity was obtained after 1.5 h of CVD. Further deposition decreased the permeances of the gases and the selectivity since the pores were blocked by the deposition of the amino-silicate. For the membrane formed with only APTES (R= 100%), the permeances of the gases remained high but the CO_2/CH_4 selectivity was low. The membrane with (R= 100%) showed lower CO_2/CH_4 selectivity than the membranes with lower R. This result is attributed to the formation of a loose structure that allows both CO_2 and CH_4 to permeate easily. The membrane with an R= 20% displayed the best performance achieving a CO_2 permeance of $2.3x10^{-7}$ mol $m^{-2}s^{-1}Pa^{-1}$ and an ideal CO_2/CH_4 selectivity of 40. It is surmised that appropriate pore sizes for the separation of CO_2 were formed in the membrane. It has been shown that a permeance level of 10^{-7} mol $m^{-2}s^{-1}Pa^{-1}$ is required for commercial applications [4], so the results are significant.

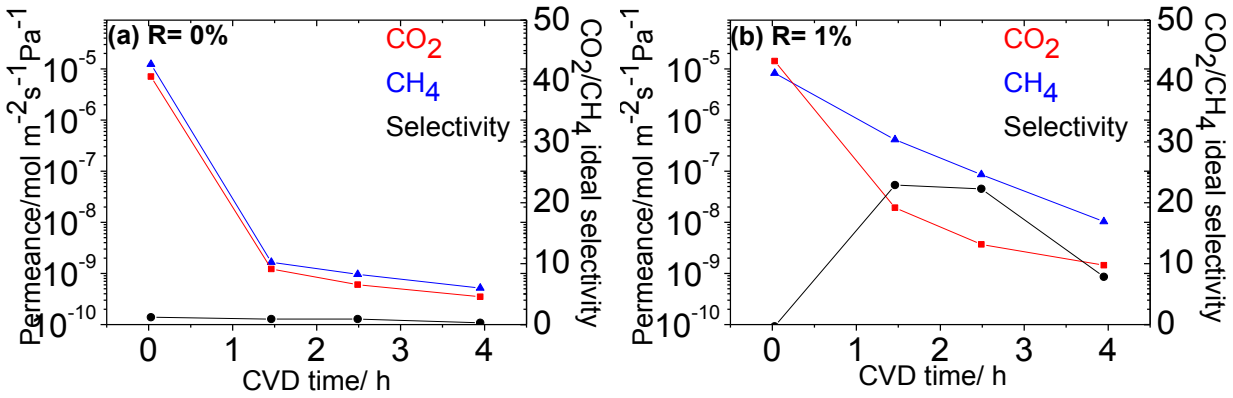

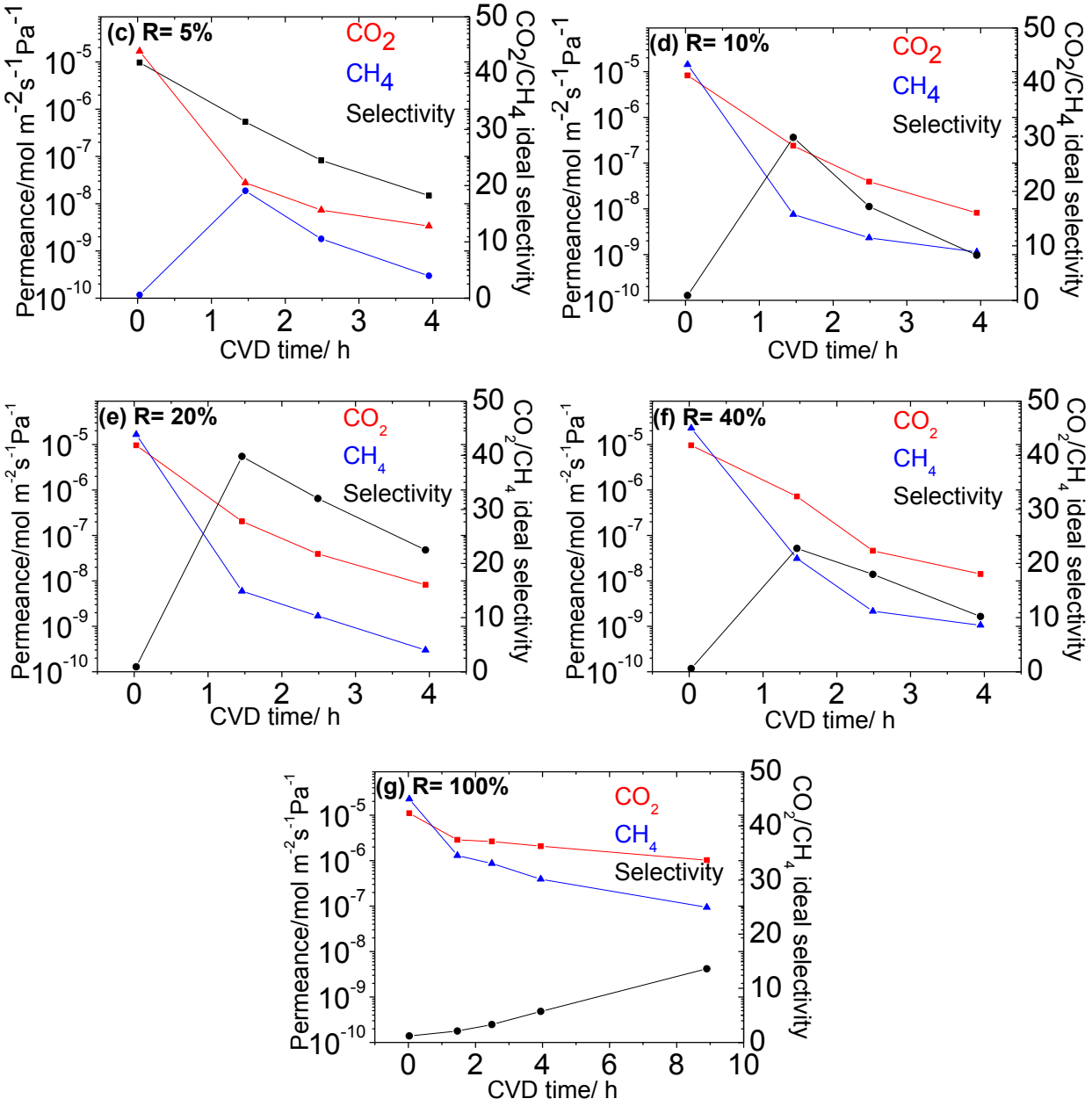

Fig. 8: Separation performance of the prepared membranes as a function of the ratio R at 393 K and 0.10 MPa. (a) R= 0%; (b) R= 1%; (c) R= 5%; (d) R= 10%; (e) R= 20%; (f) R= 40% and (g) R= 100%.

The reproducibility of the synthesis of the membrane with R= 20% was also verified. **Fig. 9** plots the permeance of the CO_2 and CH_4 as a function of the CVD time. The membrane had a CO_2 permeance of 1.4 mol $m^{-2}s^{-1}Pa^{-1}$ and an ideal selectivity of 43. However, the CVD time

increased from 1.5 to 5 h. This was because the topmost intermediate layer had bigger particle size (50 nm). Therefore, a longer time was needed to cover the whole surface.

The stability of the membrane with R=20% was verified in the course of the mechanism studies to be discussed in a subsequent section. The membrane was stable for the duration of the measurements of 20 h. Similar organosilicate membranes have been shown to be thermally stable under hydrothermal conditions [5].

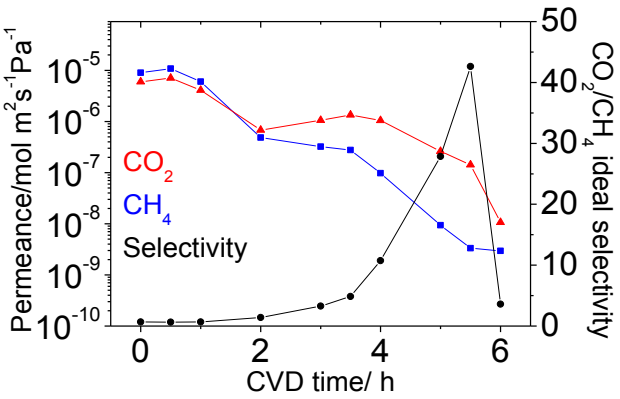

Fig. 9: New synthesized membrane with R= 20% at 393 K and 0.10 MPa.

2.2.2 Pore size calculation

In order to obtain insight on the pore structure of the R= 20% membrane, the permeances of various molecules with different kinetic diameter were measured at 393 K. The molecules used were CO_2, CH_4, N_2, and H_2 (**Table 3**) [6].

Table 3: Molecular size of used gases

Gas molecule	**Kinetic diameter (nm)**
H_2	0.289
CO_2	0.330
N_2	0.364
CH_4	0.387

The permeation properties of the above molecules after 1.5, 2.5 and 4 h of CVD using APTES and TEOS mixtures (R=0, 20, 100%) are shown in **Fig. 10**, with the CVD times shown by the blue, green and black lines, respectively.

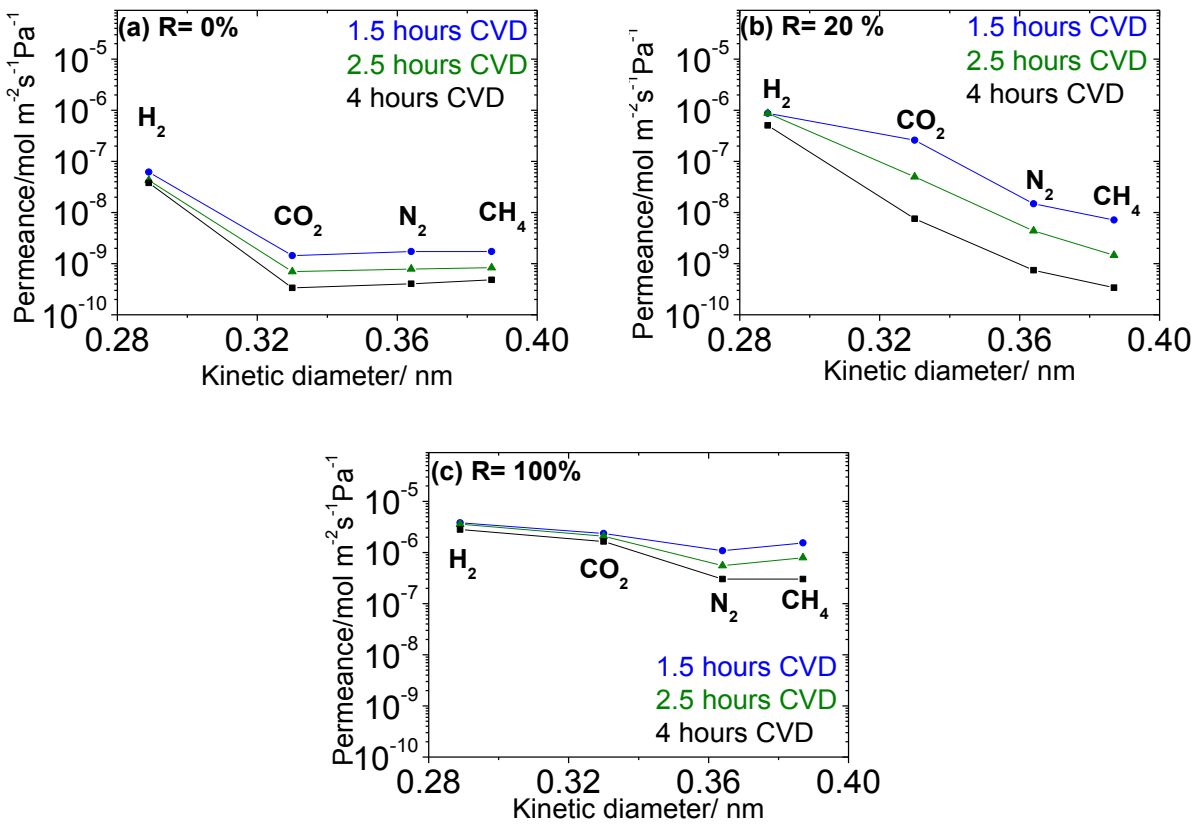

Fig. 10: Gas permeance change of various molecules with different kinetic diameter at 393 K and 0.10 MPa. Membrane with (a) R= 0%; (b) R= 20% and (c) R= 100%.

For the membrane with only TEOS (R= 0%), the permeances of the molecules larger than CO_2 are not different, but H_2 shows relatively high permeance. As discussed in a number of previous studies [1,3], membrane (R= 0%) does not have continuous pores but has a network of solubility sites with permeation occurring by jumps from site to site.

For the membrane with only APTES (R= 100%), the differences in gas permeance of various gases are very small compared with those of membranes (R= 0%) or (R= 20%). This shows that large pore sizes are formed that are not suitable for the separation of CO_2. Overall the results suggest that the control of the ratio of APTES and TEOS is important to fabricate membranes with an appropriate pore size for the separation of CO_2.

The membrane with 20% APTES (R= 20%), appear to operate by a molecular sieving mechanism. The pore size of the microporous membrane was estimated using Tsuru's method, in which a normalized Knudsen permeance (NKP) is calculated for gases with different kinetic diameter such as CO_2, CH_4, N_2, and H_2 [7]. This method is derived from a gas translation model. This normalized permeance is plotted versus the molecular size and is fitted using equation **Eq. (12)** where f represents the ratio of the permeance of the i-th component (P_i) to that predicted from a reference component (He) based on the Knudsen diffusion mechanism. Herein, He is employed as a reference component because it has the smallest molecular size (0.260 nm).

$$f = \frac{\left(1-{d_i}/{d_p}\right)^3}{\left(1-{d_{He}}/{d_p}\right)^3} \qquad \textbf{Eq. (12)}$$

where d_i is the kinetic diameter of a gas i [nm], d_{He} is the kinetic diameter of helium and d_p is the estimated membrane pore size [nm].

Both the plots and fits results for the membrane (R= 20%) after 1.5 h CVD employing the permeances measured at 523 K are presented in **Fig. 11**. The result yields to a mean pore size of 0.44 nm. Previously, the characteristic distance for the membrane derived from TEOS was determined to be 0.34 nm prepared through a sol-gel method [7] and a CVD process [1]. Hence, the mean pore size is about 0.1 nm larger than that for the membranes using APTES and TEOS and this small difference in pore size significantly affects the gas permeance properties and CO_2 separation performance. According to Wang et al. [8] and Thornton et al. [9], the optimum pore size for the separation for CO_2 was found to be 0.40 nm because CO_2 and CH_4 permeate through

membranes by different mechanisms, a surface diffusion mechanism for CO_2 and an activated diffusion mechanism for CH_4. Membranes prepared in this work have essentially this optimal value.

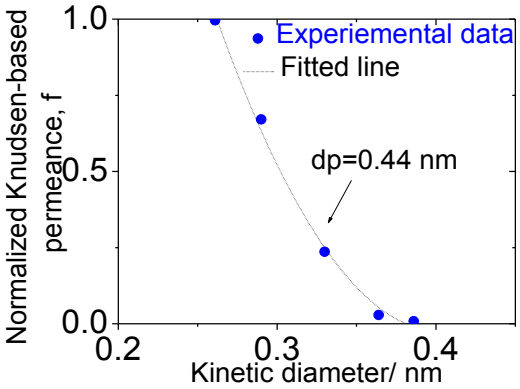

Fig. 11: Determination of pore size of the membrane (R = 20%) after 1.5 h CVD at 523K using normalized Knudsen-based permeance as a function of molecular size.

2.2.3 Transport mechanism of CO_2 and CH_4

In order to investigate the transport mechanism of the membrane (R = 20%), the temperature dependency of the permeances of several gases, especially CO_2 and CH_4 were measured. The temperature was varied from 363 K to 523 K and the results are shown in **Fig. 12(a)**. In the case of CO_2, the permeance went through a maximum with temperature as shown in **Fig. 12 (b)**. Because CO_2 is a condensable gas, it interacts with the membrane wall and likely moves by a surface diffusion mechanism. In the case of CH_4, the permeance is constant with temperature as shown in **Fig. 12 (c)**. Although CH_4 is also condensable, it is more volatile than CO_2, so can desorb easily. This makes it a candidate for the gas-translational mechanism, also called activated Knudsen diffusion which occurs when a species can escape the surface potential to some extent but is restrained by the pore walls.

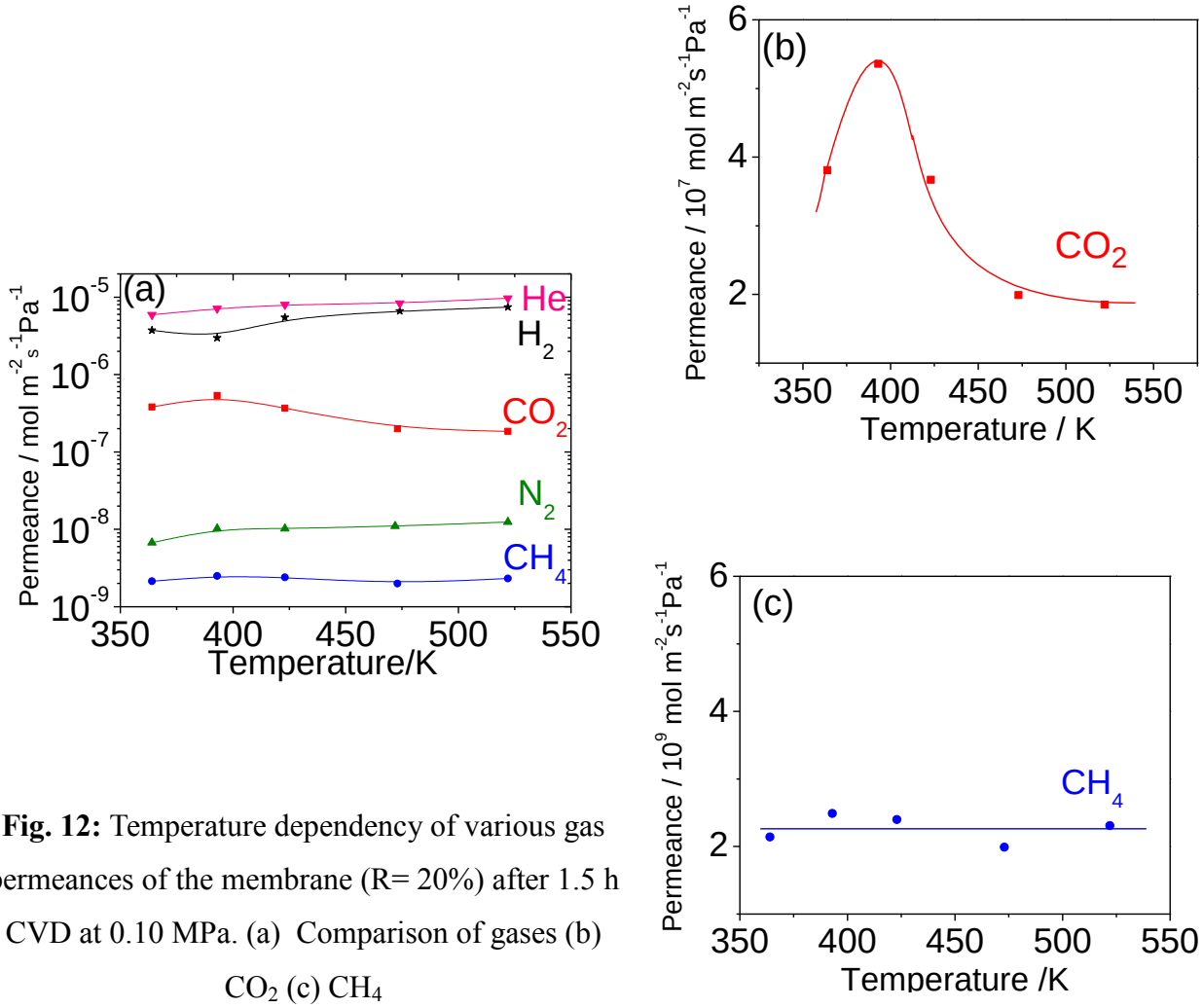

Fig. 12: Temperature dependency of various gas permeances of the membrane (R= 20%) after 1.5 h CVD at 0.10 MPa. (a) Comparison of gases (b) CO_2 (c) CH_4

In surface diffusion gas molecules adsorb on the membrane surface, diffuse into the membrane pore and desorb at the pore exit. The adsorption process can be described by the Langmuir adsorption model in membranes as follows:

$$\theta = \frac{q}{q_s} = \frac{K_p}{1+K_p} \qquad \textbf{Eq. (13)}$$

where θ is the fractional occupancy of adsorption sites, q the amount of adsorbed gas molecules per unit mass of adsorbent [mol kg^{-1}], q_s the saturation amount of adsorbed molecules [mol kg^{-1}], p the pressure [Pa], and K an adsorption equilibrium constant [Pa^{-1}]. This constant can be described by a Van't Hoff expression as shown in **Eq. (14).**

$$\mathrm{K} = K_0 \exp\left(\frac{-\Delta H_a}{RT}\right) \quad \textbf{Eq. (14)}$$

where ΔH_a is the enthalpy of adsorption [J mol^{-1}]. Using **Eq. (13)** and **Eq. (14)**, the concentration of the diffusing gas in the membrane is presented as in **Eq. (15)**.

$$\mathrm{c} = \rho\mathrm{q} = \rho q_s K_0 p \frac{\exp\left({}^{-\Delta H_a}/_{RT}\right)}{1+K_0 p\, exp\left({}^{-\Delta H_a}/_{RT}\right)} \quad \textbf{Eq. (15)}$$

where ρ is the density of the gas molecules [kg m^{-3}]. Since it is assumed that surface diffusion takes place by molecules which jump from one site to another, a diffusion coefficient is introduced as shown in **Eq. (16)**:

$$D_{SD} = \frac{\varepsilon}{\tau}\lambda^2 \nu\, exp\left(-\frac{\Delta H_{SD}}{RT}\right) = D_0\, exp\left(-\frac{\Delta H_{SD}}{RT}\right) \quad \textbf{Eq. (16)}$$

where ε represents the porosity, τ the tortuosity, λ the distance between the adsorption sites [m], $\lambda\nu$ the velocity in the right direction [m s^{-1}] given by the probability, g_d , ν the jump frequency of the molecule between adsorption sites [s^{-1}] and ΔE_{SD} the energy barrier to be overcome by diffusion [J mol^{-1}]. Using Fick's model, the molar flux, N_{SD} [mol m^{-2} s^{-1}] can be written as:

$$N_{SD} = -D_{SD}\frac{dc}{dZ} = D_{SD}\frac{c}{L} = A\, exp\left(-\frac{\Delta H_{SD}}{RT}\right)\frac{\exp\left({}^{-\Delta H_a}/_{RT}\right)}{1+K' exp\left({}^{-\Delta H_a}/_{RT}\right)}p \quad \textbf{Eq. (17)}$$

where $\mathrm{A} = \frac{D_0 \rho q_s K_0}{L}$ and $K' = K_0 p$

Therefore, the permeance for surface diffusion can be as written as:

$$\overline{P_{SD}} = A \exp\left(-\frac{\Delta H_{SD}}{RT}\right)\frac{\exp\left({}^{-\Delta H_a}/_{RT}\right)}{1+K' exp\left({}^{-\Delta H_a}/_{RT}\right)} \quad \textbf{Eq. (18)}$$

The left side of this expression has a surface diffusion term which increases with temperature. The right side has the adsorption dependency, which decreases with temperature. Thus, a maximum is obtained which fits the observed behavior shown in **Fig. 12 (b).**

In gas-translation mechanism contributions of both surface diffusion and gas-translation are present. By introducing a probability α for diffusion through a micropore to the Knudsen diffusion model, the following equation is obtained in **Eq. (19)**.

$$\overline{P_{GT}} = \frac{\varepsilon d_p a}{\tau L}\left(\frac{8}{\pi MRT}\right)^{1/2} \qquad \textbf{Eq. (19)}$$

Moreover, the probability α consists of a pre-exponential, a_g and a diffusion barrier as shown in **Eq. (20)**;

$$\alpha = \alpha_g \exp\left(-\frac{\Delta E}{RT}\right) \qquad \textbf{Eq. (20)}$$

Hence, using **Eq. (19)** and **Eq. (20)**, the permeance in the gas-translational model is presented in **Eq. (21)**.

$$\overline{P_{GT}} = A\frac{1}{\sqrt{T}}\exp\left(-\frac{\Delta E}{RT}\right) \qquad \textbf{Eq. (21)}$$

where $A = \frac{\varepsilon d_p \alpha_g}{\tau L}\left(\frac{8}{\pi MR}\right)^{1/2}$

It can be seen from **Eq. (21)** that there is a partial cancellation of temperature contributions. The inverse square root of temperature decreases with temperature, but the exponential increases with temperature and this may result in the constant temperature profile observed in **Fig. 12 (c)**. Fitting of **Eq. (18)** to the experimentally acquired permeance for CO_2 and **Eq. (21)** to the data for CH_4 give the results shown in **Table 4**. The table also includes the regression coefficients of the fitting parameters for CO_2 and CH_4.

Table 4: Parameters of the transport models for CO_2 and CH_4

Gas	Model	Model parameters				Regression coefficient
		A	ΔE_{SD} (kJ mol^{-1})	ΔH_a (kJ mol^{-1})	K'	
CO_2	Surface diffusion	1.58×10^{-9}	6.84	-26.3	6.21×10^{-4}	0.876
CH_4	Gas-translation	1×10^{-6}	1.60	-	-	0.975

2.2.4 Microscopic structure

The surface and the cross section of the synthesized membranes are shown in **Fig. 13**. The surface structure shows that the intermediate layers helped to form a defect free topmost layer (**Fig. 13(b)**, **Fig. 13(c)** and **Fig. 13(d)**). The globular structure seen in the surface of the membranes with a silica layer (R= 0, 20 and 100%) indicates that during the synthesis steps intermediate species adsorbed on the solid surface are decomposed to silica [10]. In the membrane with only APTES (R= 100%), defects seen on the surface contributed to the low separation performance. However, there were no defects on the surfaces of membranes with R= 0 and 20%. The cross-sectional images of the membrane with no APTES (R= 0%) and with R= 20% show the formation of silica layers (**Fig. 13(f), (g)**). The thickness of the silica layer in the R= 20% membrane was about 23 nm (**Fig. 13(g)**) but in the membrane with only APTES (**Fig. 13(h)**), the topmost layer was very thin.

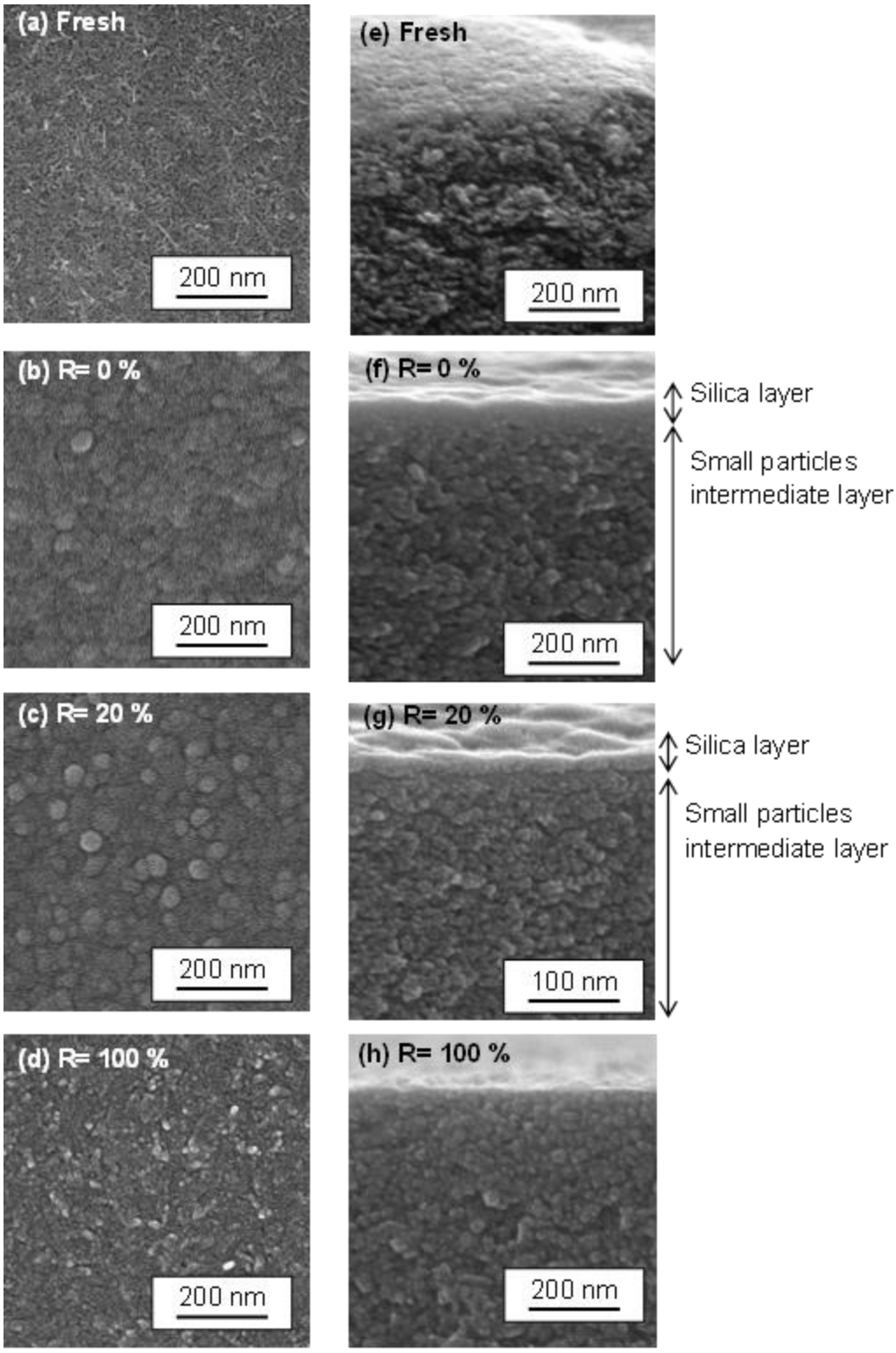

Fig. 13: SEM images of the (a)-(d) top surface and (e)-(h) cross-section. (a) and (e) are for the membrane before CVD, (b) and (f) are for the membrane (R= 0%), (c) and (g) are for the membrane (R= 20%), (d) and (h) are for the membrane (R= 100%).

2.2.5 Membrane composition

The presence of amine groups on the surface of the membranes was confirmed by XPS analysis. **Fig. 14 (a)** shows the N_{1s} spectra of the membranes with different APTES ratios (R from 5 to 100%). In the membrane with R= 1%, nitrogen was not detected. However, the nitrogen peak area increased as the concentration of amino-functionalized precursor increased. The N_{1s} spectra of the 20% APTES membrane is divided into two features (**Fig. 14 (b)**) which can be assigned to $-NH_2$ and $-NH_3^+$ [11,12,13]. The detection of $-NH_3^+$ indicates that carbamates may be formed which explains the interaction of CO_2 molecules with amine groups.

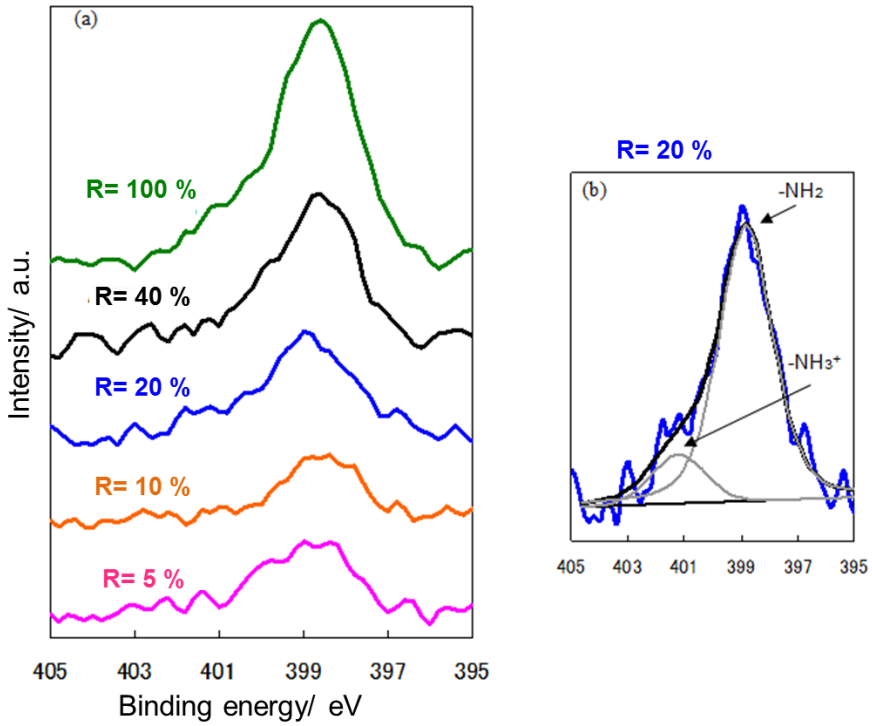

Fig. 14: (a) N1s spectra for membrane with APTES 5% to 40% and (b) assigned N1s spectral of membrane with APTES 20%.

The N/Si ratio was obtained using 1.77 and 0.86 as relative sensitivity factors for nitrogen and silica, respectively, applied to the peak areas calculated from the spectra shown in **Fig. 15**. The calculations revealed that the N/Si ratios increased with the concentration of amino-functionalized precursor. These values were significantly lower compared to the expected N/Si ratios. These results may have been can be caused by the removal of some of the aminopropyl

groups during the CVD. The low ratio also indicates that there is no need to use a higher amine concentration in these microporous hybrid membranes.

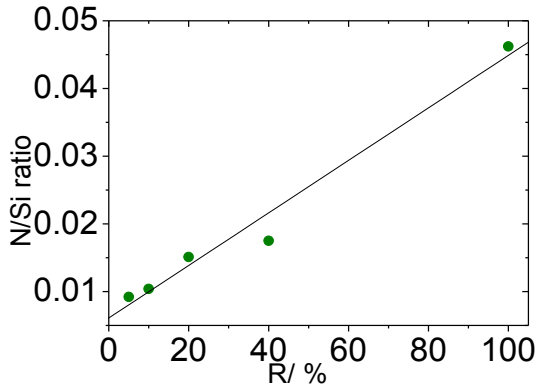

Fig. 15: The relationship between APTES ratio and N/Si ratio for hybrid membranes.

2.5 Conclusions

Inorganic-organic hybrid membranes were prepared by placing silica and amino-silica species on the surface of alumina supports by chemical vapor deposition at 673 K using tetraethylorthosilicate (TEOS), 3-aminopropyltriethoxysilane (APTES) as precursors and oxygen as co-reagent. The amino-silica ratio R was varied from R= 0 to 100%. The presence of nitrogen on the surface of the membrane was confirmed by XPS analysis, Nitrogen exists on the surface in two states, $-NH_2$ and $-NH_3^+$, and both contribute to the interactions with CO_2. The highest separation performance was obtained for the membrane having an R= 20% with a CO_2 permeance of 2.3×10^{-7} mol $m^{-2}s^{-1}Pa^{-1}$ and a CO_2/CH_4 ideal selectivity 40 at 393 K. The mean pore size of the hybrid membrane was calculated by Tsuru's method and was estimated to be 0.44 nm. The transport mechanisms for CO_2 was surface diffusion and for CH_4 was gas-translation.

The obtained permeance was beyond the 10^{-7} mol $m^{-2}s^{-1}Pa^{-1}$ level considered necessary for commercial application. The selectivity of 40 is reasonable for obtaining a pipeline quality gas (< 2.4% impurity). The permeated gas was CO_2 and the retained gas was CH_4, which is highly desirable in practice because it allows for retention of methane at high pressure, and saves substantially on downstream compression costs. Note that CO_2 is substantially heavier than CH_4, so that CO_2 would normally permeate slower.

2.6 References

[1] S.T. Oyama, M. Yamada, T. Sugawara, A. Takagaki, R. Kikuchi. Review on mechanisms of gas permeation through inorganic membranes, J. Jpn. Pet. Inst. 54 (2011) 298-309.

[2] Y. Gu, S.T. Oyama, Ultrathin hydrogen-selective silica membranes deposited on alumina-graded structures prepared from size-controlled boehmite sols, J. Membr. Sci. 306 (2007) 216.

[3] Y. Gu, P. Hacarlioglu, S.T. Oyama, Hydrothermally stable silica-alumina composite membranes for hydrogen separation, J. Membr. Sci. 310 (2008) 28.

[4] H. Lim, Y. Gu, S. T. Oyama, Studies of the effect of pressure and hydrogen permeance on the ethanol steam reforming reaction with palladiumand silica-based membranes, J. Membr. Sci. 396 (2012) 119-127.

[5] X. Ren, K. Nishimoto, M. Kanezashi, H. Nagasawa, T. Yoshioka and T. Tsuru. CO_2 permeation through hybrid organosilica membranes in the presence of water vapor. Ind. Eng. Chem. Res. 53 (2014) 6113−6120

[6] D. W. Breck, Zeolite molecular sieves: Structure, chemistry, and use, Johm Wiley & Sons, New York, 1973.

[7] H. R. Lee, M. Kanezashi, Y. Shimomura, T. Yoshioka, T. Tsuru, Evaluation and fabrication of pore-size-tuned silica membranes with tetraethoxydimethyl disiloxane for gas separation, AIChE. J. 57(2011) 2755-2765.

[8] Z. Wang, L.E.K. Achenie, S.J. Khativ, S.T. Oyama, Simulation study of single-gas permeation of carbon dioxide and methane in hybrid inorganic-organic membrane, J. Membr. Sci. 387-388 (2012) 30-39.

[9] A. W. Thornton, T. Hilder, A.J. Hill, J.M. Hill, Predicting gas diffusion regime within pores of different size, shape and composition, J. Membr. Sci. 336 (2009) 101-108.

[10] S. Morooka, S. Yan, K. Kusakabe, Y. Akiyama, Formation of hydrogen-permselective SiO_2 membrane in macropores of a-alumina support tube by thermal decomposition of TEOS, J. Membr. Sci. 101 (1995) 89-98.

[11] A.E. Hooper, D. Werho, T. Hopson, O. Palmer, Evaluation of amine- and amide-terminated self-assembled monolayers as 'Molecular glues' for Au and SiO_2 substrates, Surf. Interface Anal. 31 (2001) 809-814.

[12] E.T. Vandenberg, L. Bertilsson, B. Liedberg, K. Uvdal, R. Erlandsson, H. Elwing, I. Lundstrom, Structure of 3-Aminopropyl Triethoxy Silane on Silicon Oxide, J. Colloid Interface Sci. 147 (1991) 103-118.

[13] A. Calvo, P.C. Angelome, V.M. Sanchez, D.A. Scherlis, F.J.Williams, G.J.A.A. Soler-Illia, Mesoporous aminopropyl-functionalized hybrid thin films with modulable surface and environment-responsive behavior, Chem. Mater. 20 (2008) 4661-4668.

Chapter 3: Comparison between Different Alkyl Amino-Silica Hybrid Membranes

This Chapter is a modified version of a paper submitted to the Journal of Membrane Science: S. Belhaj Messaoud, A. Takagaki, T. Sugawara, R. Kikuchi, S.T. Oyama, Alkylamine-silica hybrid membranes for carbon dioxide/methane separation. J. Membr. Sci. 477(2015)161–171.

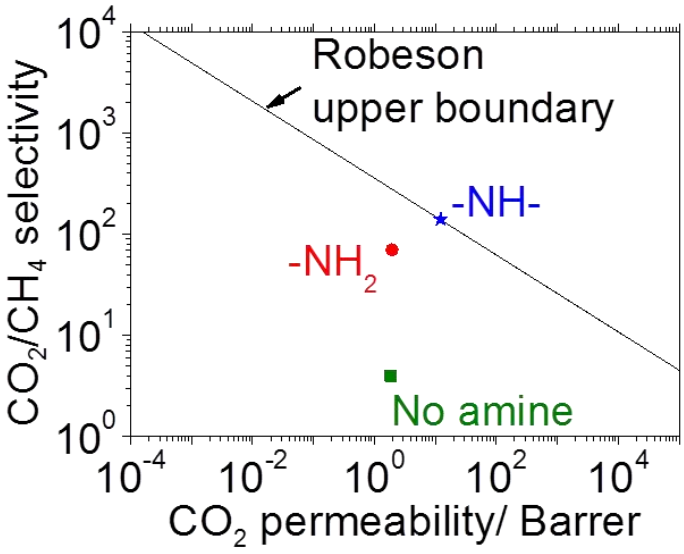

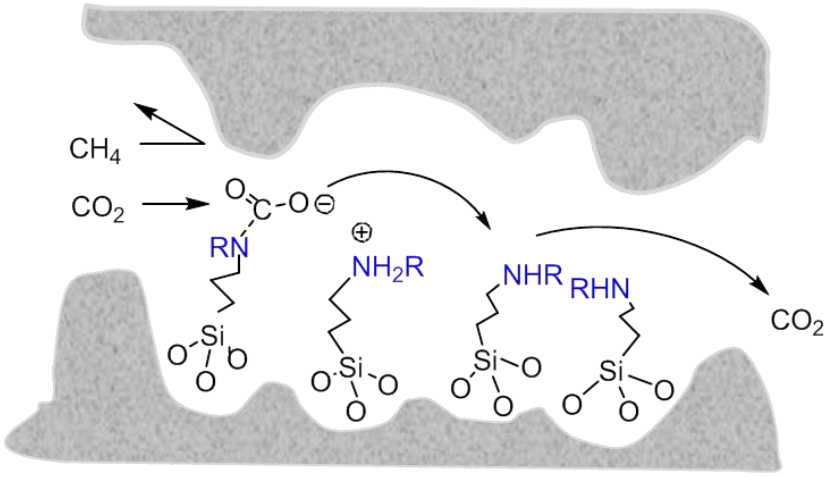

Overview

Hybrid membranes are promising materials for the purification of natural gas from carbon dioxide. The present chapter investigates the effect of the incorporation of primary and secondary amine functional groups on the performance of an organic-inorganic hybrid silica membrane for CO_2/CH_4 separation. Hybrid membranes were synthesized by chemical vapor deposition using 3-aminopropyltrimethoxysilane and (3-methylaminopropyl)trimethoxysilane as primary and secondary alkylamine-silica precursors, respectively. The amino functionalized membranes were compared to an amine-free membrane prepared using propyltrimethoxysilane as precursor. The amine-free membrane had a CO_2 permeance of $2.1x10^{-8}$ mol $m^{-2}s^{-1}Pa^{-1}$, a CO_2/CH_4 selectivity of 4 and a pore size of 0.37 nm. The primary amine membrane displayed a CO_2 permeance of $2.1x10^{-8}$ mol $m^{-2}s^{-1}Pa^{-1}$, a CO_2/CH_4 selectivity of 70 with a pore size of 0.36 nm. The secondary amine achieved a CO_2 permeance of $1.3x10^{-7}$ mol $m^{-2}s^{-1}Pa^{-1}$, a CO_2/CH_4 selectivity of 140 with a pore size of 0.43 nm. The pore sizes were estimated by Tsuru's method. The transport mechanism of CO_2 throughout the amino-silica hybrid membranes was surface diffusion. The secondary amino-silica hybrid membrane was stable for 60 h under a relative humidity of 20%.

3.1 Experimental

3.1.1 Materials

Porous alumina tubes (length: 3 cm, outside diameter: 10 mm, thickness: 1 mm, pore size: 5 nm) obtained from the Pall Corporation were used as membrane supports and were. The membrane support was connected to dense alumina using same procedure described in the previous **Chapter 2**. Same materials were used to synthesize the boehmite sols.

The silica precursor was tetraethylorthosilicate (TEOS, TCI, ≥ 96.0%, CAS number 78-10-4). The alkylamine compound, propyltrimethoxysilane (PTMS, Sigma Aldrich, 97%, CAS number 1067-25-0) was used an as amine-free silica precursor. The primary alkylamine compound, (3-aminopropyltrimethoxysilane (APTMS, Sigma Aldrich, ≥ 98.0%, CAS number 13822-56-5) and the secondary amine compound, (3-methylaminopropyl) trimethoxysilane (MAPTMS, Sigma Aldrich, 97%, CAS number 3069-25-8) were selected as amino-silica precursors. All silanes were supplied from Tokyo Chemical Industry. Pure Ar, He, H_2, O_2, CO_2,

N_2, CH_4 and SF_6 gases with a purity of 99.9% were acquired from Tokyo Koatsu Yamazaki Co., Ltd.

3.1.2 Membrane synthesis

The synthesis consisted of depositing, first, two intermediate γ-alumina layers using sol-gel method, then, the topmost selective layer using CVD. Details of the deposition methods were described in **Chapter 2**. Large and small particle size boehmite sols with 80 and 40 nm diameters, respectively, were used. The membrane support was attached to gas delivery lines and heated with a furnace to 673 K using a heating rate of 1 K min^{-1} (**Fig. 7**). The flow to the inner side of the support was switched from inert gas to a stream of silica precursor (TEOS), organo-silica precursor (PTMS or APTMS or MAPTMS), and co-reagent (O_2). Argon gas carried the silica and organo-silica reactants from bubblers to the membrane support through heated lines. Argon was also used to balance the pressure on the outer side of the membrane support. The total molar flow rate of the silica precursor was constant for all experiments and the CVD was carried out at atmospheric pressure. The concentration of the precursors was controlled by fixing the temperature of the bubblers and the flow rate of the carrier gas (**Table 5**). The silica precursor (TEOS) was mixed with all organo-silica precursors in order to adjust the inorganic content of the obtained membranes. The amine to silica ratio was chosen to be 20% based on the results presented in the previous chapter and on prior works by Paradis et al. [1]. The CVD was performed until an adequate selectivity was obtained and a CO_2 permeance in the range of 10^{-7} mol $m^{-2}s^{-1}Pa^{-1}$ was attained.

Table 5: Chemical vapor deposition conditions of the three synthesized organo-silica membranes

CVD parameter	**Amount**
Molar flow rate of the silica precursor (TEOS) (μmol s^{-1}*)	13
Molar flow rate of the co-reagent (O_2) (μmol s^{-1})	13
Molar flow rate of the organo-silane precursor (PTMS or APTMS or MAPTMS) (μmol s^{-1})	30
Molar flow rate of the balance gas (Ar) (μmol s^{-1})	56
$F_{Organo-silane} / \left(F_{Organo-silane} + F_{TEOS}\right)$ (%)**	20
CVD temperature (K)	673
Bubbler temperature of TEOS (K)	349
Bubbler temperature of PTMS (K)	272
Bubbler temperature of APTMS (K)	341
Bubbler temperature of MAPTMS (K)	317

* Flows in μmol s^{-1} can be converted to normal cm^3 min^{-1} by multiplying by 1.5

** *F* is the molar flow rate (μmol s^{-1})

Throughout this chapter, the membranes are named according to the organo-silica precursor type (**Fig. 16**). The membranes in which the precursor has no amine (PTMS), a primary amine (APTMS) and a secondary amine (MAPTMS) functionality are named M-0, M-I, and M-II, respectively.

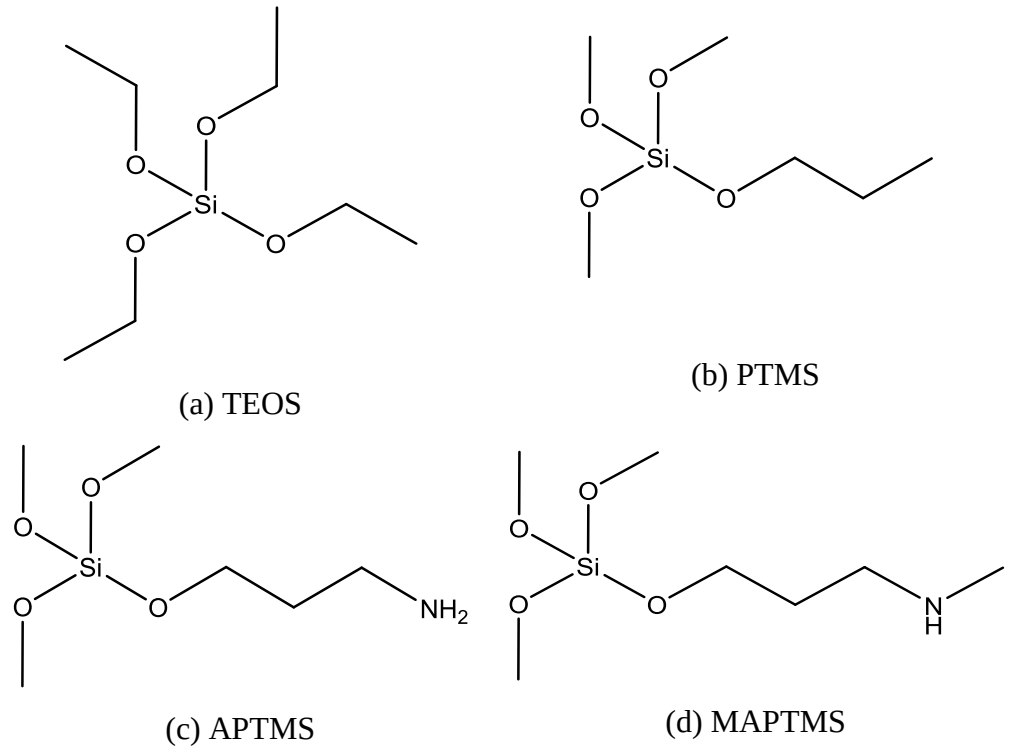

Fig. 16: Chemical structure of (a) silica, (b) amine-free silica, (c) primary amino-silica and (d) secondary amino-silica precursors.

3.1.3 Characterization techniques

The synthesized membranes were characterized in the same way as in **Chapter 2**.

3.1.4 Permeation measurements

The permeances of various gases (He, H_2, CO_2, N_2, CH_4 and SF_6) were measured separately (**Table 6**). The permeance measurements were conducted after fixing the furnace temperature at 393 K and the pressure difference between the inner and the outer side of membrane at 0.10 MPa. The permeance measurements were carried out before and after CVD and were repeated at least three times. The permeance and the selectivity were calculated using **Eq. (1)** and **Eq. (2)** explained in **Chapter 1**.

Table 6: Molecular weight and kinetic diameter of the permeated gases [2].

Gas molecule	Molecular weight (g mol^{-1})	Kinetic diameter (nm)
He	4	0.265
H_2	2	0.289
CO_2	44	0.330
N_2	28	0.364
CH_4	16	0.387
SF_6	146	0.502

3.1.5 Stability test

The conventional process to purify natural gas starts generally by condensation and dehydration steps before the removal of CO_2 [3]. Nevertheless, the gas stream may contain some water vapor before reaching the acid gas removal step. In this work, a steam tolerance test was carried out at 393 K for 60 h. The hydrothermal stability of the best synthesized hybrid membrane was evaluated at 393 K for 60 h in a flow system with a bubbler. Argon gas was used to carry distilled water from the bubbler to the membrane heated at 393 K. The relative humidity (RH) inside the membrane calculated using **Eq. (22)** was set to 20%.

$$RH(\%) = \frac{Water\ partial\ pressure}{Water\ saturation\ vapor\ pressure\ at\ the\ same\ temperature} \qquad \textbf{Eq. (22)}$$

The water saturation vapor pressure at 393 K was 198.5 kPa [4].The water partial pressure inside the membrane was 39.7 kPa and was calculated from the inlet gas composition. Both water bubbler and the membrane were at atmospheric pressure. The water bubbler temperature was adjusted to 334 K and the Ar molar flow rate was set at 13 μmol s^{-1}. Argon gas was also used as balance gas in the outer side of the membrane. The test was stopped periodically and the permeances of CO_2 and CH_4 were measured. Before every measurement, the membrane was dried at 503 K for 0.5 h in dry Ar flow using a heating and a cooling rate of 1 K min^{-1}.

3.2 Results and discussion

3.2.1 Boehmite sol analysis

Dynamic light scattering was used to measure the particle size distribution of the synthesized boehmite sols. The particle size distributions of the obtained boehmite sol precursors show maxima at 80 and 40 nm for the large and the small sols (**Fig. 17**). The same sols were used to dip-coat the three investigated membranes M-0, M-I and M-II. The sols were stored at room temperature under 200 rpm stirring for over two months. The storage did not generate any apparent change of the particle size.

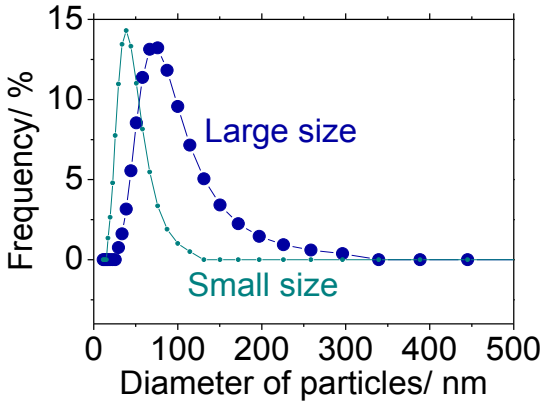

Fig. 17: Particle size distribution of large and small size boehmite sols.

3.2.2 Single gas permeation properties

Two types of membrane with primary and secondary amine functionality were prepared (M-I and M-II). A reference membrane in which the precursor has a similar chemical structure but no amine functionality was also synthesized (M-0) (**Fig. 16**). The permeances of the different single gases as a function of CVD time through the M-0, M-I and M-II membranes were measured at 393 K and 0.10 MPa (**Fig. 18 (a, b and c)**).

Before CVD, the order of permeance of the gases followed the inverse square root of their molecular weight (**Table 6**), H_2 > He > CH_4 > N_2 > CO_2 > SF_6 which obeyed the Knudsen diffusion mechanism. The ideal pair gas selectivities also had values that confirmed this mechanism such as 0.6 for CO_2/CH_4 or 2.8 for H_2/CH_4. For all membranes, the permeance of all gases dropped as the CVD progressed, indicating that a silica layer was being continuously formed. The drop was steeper for the larger gas species indicating a reduction in membrane pore

size. This caused the selectivity for small gas species compared to bigger gas molecules to grow. The best performance for the different precursor was achieved at different CVD times. At the optimum CVD time, the SF_6 molecule was not detected by flow meter measurements indicating a permeance < $1x10^{-9}$ mol $m^{-2}s^{-1}Pa^{-1}$. It can be concluded that the pores in the pretreated alumina support were being covered gradually, reaching a size lower than 0.5 nm. At the end of the CVD, the order of gas permeance, for the M-I and M-II membranes, changed and followed the order of the kinetic diameter of the molecules, He ≈ H_2 > CO_2 > N_2 > CH_4 > SF_6 (**Table 6**), showing that the few remaining pores were in the size range of molecular sieves.

The detailed CO_2 and CH_4 permeances and ideal selectivity data for the M-0, M-I and M-II membranes are presented in **Fig. 18 (d, e, and f)**. For the M-0 membrane, a sudden drop can be seen after 1 h of CVD. The CO_2/CH_4 pair gas selectivity did not show an important improvement. The optimum performance was obtained after 1.25 h of CVD with a CO_2 permeance of $2.1x10^{-8}$ mol $m^{-2}s^{-1}Pa^{-1}$ and CO_2/CH_4 selectivity of 4 (**Fig. 18 (d)**). For the M-I membrane, the permeance dropped smoothly and a large gap can be seen separating small and big molecules. The highest performance was obtained after 2.75 h CVD with a CO_2 permeance of $2.3x10^{-8}$ mol $m^{-2}s^{-1}Pa^{-1}$and a CO_2/CH_4 selectivity of 55 (**Fig. 18 (e)**). For the M-II membrane, a noticeable gap was obtained. However, it was larger than that of the M-I membrane, improving the CO_2/CH_4 selectivity. The highest performance was obtained after 1.5 h CVD with a CO_2 permeance of $1.8x10^{-7}$ mol $m^{-2}s^{-1}Pa^{-1}$and a CO_2/CH_4 selectivity of 84 (**Fig. 18 (f)**). The permeance and CO_2/CH_4 ideal selectivity showed a significant improvement. The optimum CVD time probably has little meaning here, just indicating the ease of precursor decomposition. The M-II membrane seems to carry out facilitated transport of CO_2 through the membrane better than the M-I and M-0 membranes which have the lowest separation factor (**Table 7**).

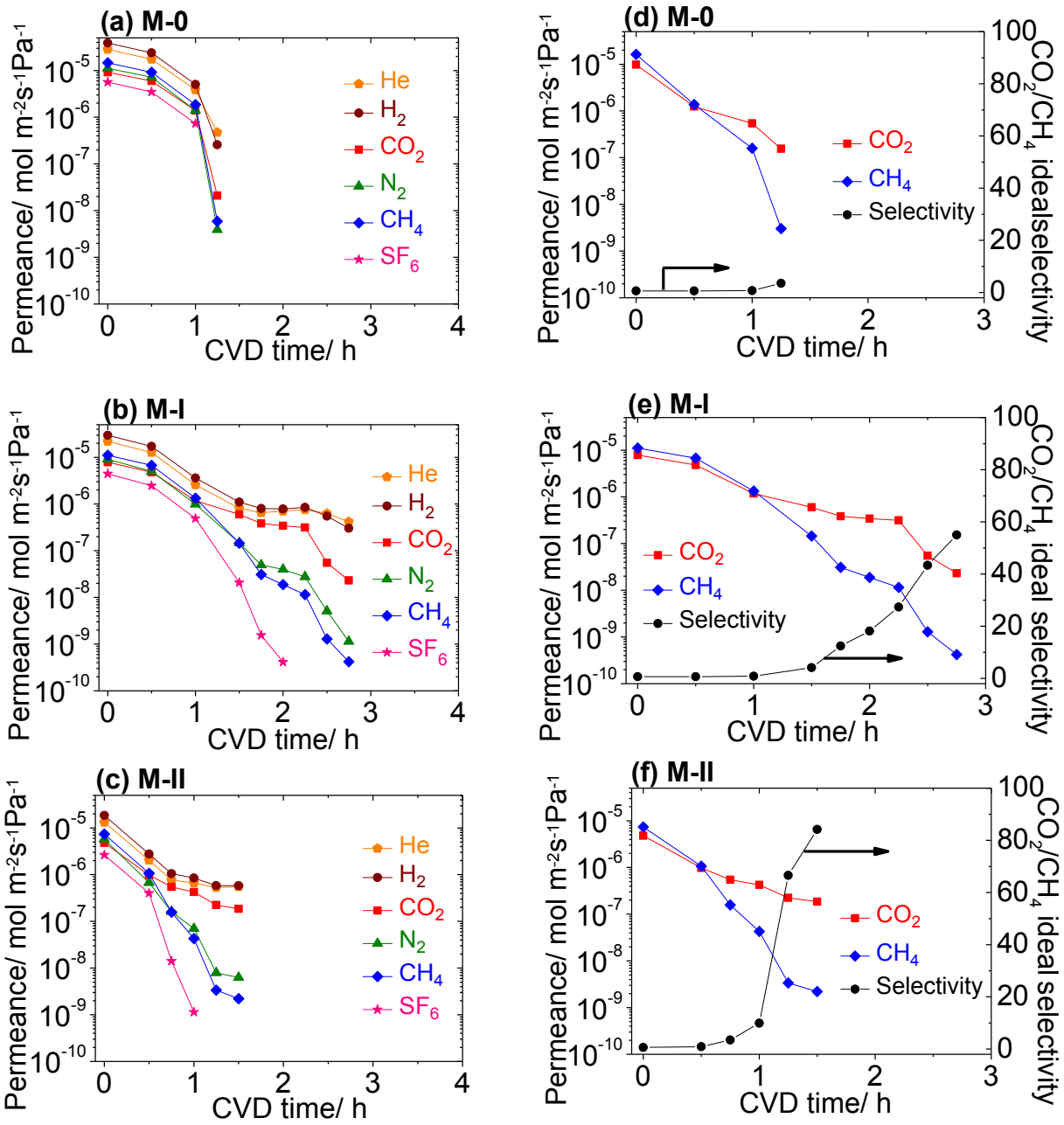

Fig. 18: Performance of M-0, M-I and M-II membranes as a function of CVD time measured at 393 K and 0.10 MPa. (a, b, c) represent the permeance of various gases and (d, e, f) show a detailed comparison of CO_2 and CH_4 gases of the M-0, M-I and M-II membranes.

Table 7: Single gas permeances at the end of the CVD at 393 K and 0.10 MPa pressure difference

Membrane	Single gas permeance (mol $m^{-2}s^{-1}Pa^{-1}$)					CO_2/CH_4 ideal selectivity
	He	H_2	CO_2	N_2	CH_4	
M-0	$4.7x\ 10^{-7}$	$2.5x\ 10^{-7}$	$2.1x\ 10^{-8}$	$3.9x\ 10^{-9}$	$5.8x\ 10^{-9}$	4
M-I	$4.1x10^{-7}$	$3.0x10^{-7}$	$2.3x10^{-8}$	$1.1x10^{-9}$	$4.2x10^{-10}$	55
M-II	$5.5x10^{-7}$	$5.8x10^{-7}$	$1.8x10^{-7}$	$6.2x10^{-9}$	$2.2x10^{-9}$	84

3.2.3 Pore size calculation

The pore sizes of the three synthesized membranes were calculated in order to have better understanding of the membrane morphology. In the first step, the permeance of He, H_2, CO_2, N_2 and CH_4 were measured at 393 K and 0.10 MPa of pressure difference. The performance of the obtained membranes at the optimum CVD time (1.25 h, 2.75 h and 1.5 h for M-0, M-I and M-II, respectively) is plotted in **Fig. 19**. The permeance of the gases roughly follows the order of kinetic diameter indicating a molecular sieving mechanism. However, there are some deviations. For example, for M-II membrane, the permeance of H_2 is higher than that of He, suggesting that H_2 can permeate by a site-hopping mechanism [5,6]. Also for the M-0 membrane, the permeance of CH_4 is higher than that of N_2, suggesting a surface diffusion pathway for CH_4.

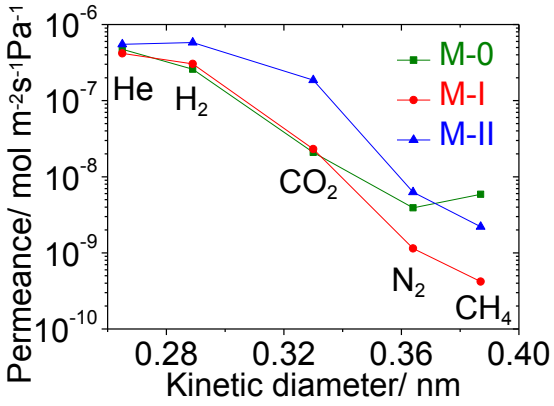

Fig. 19: Gas permeance change of various molecules with different kinetic diameter at 393 K and 0.10 MPa through M-0, M-I and M-II.

In the second step, the pore size of the synthesized hybrid membranes was estimated using Tsuru's method [7]. This method is derived from the gas translation model. First, the gas permeances of various gases with different kinetic diameters (He, H_2, N_2, and CH_4) were measured. The permeance of CO_2 was not included since this gas has strong affinity with pore walls. Then, the experimentally obtained permeances were converted to normalized Knudsen permeances using equation **Eq. (23)**. The obtained results are plotted as a function of molecular size displayed in **Table 6**. Finally, **Eq. (12)** introduced in **Chapter 2** was used to fit the experimental data, using d_p as fitting parameter.

$$f = \frac{\bar{P}_i}{\overline{P_{He}}\sqrt{\frac{M_{He}}{M_i}}} \qquad \textbf{Eq. (23)}$$

where *f* represents the ratio of the permeance of the *i*-th component ($\bar{P}_i$) to that predicted from a reference component (He) based on the Knudsen diffusion mechanism, d_i is the kinetic diameter of a gas *i* [nm], d_{He} is the kinetic diameter of helium and d_p is the estimated membrane pore size [nm]. $P_{He}\sqrt{M_{He}/M_i}$ is the permeance of the *i*-th component predicted from the He permeance under the Knudsen diffusion mechanism. M_{He} and M_i are the molecular weight of helium and gas *i*, respectively [g mol^{-1}].

The experimental and the fitted results for the M-0, M-I and M-II membranes after 1.25 h, 2.75 h and 1.5 h of CVD, respectively, are presented in **Fig. 20**. The permeances were measured at 503 K in order to minimize the interaction with the pore walls. The pore sizes are calculated to be 0.37, 0.36, 0.43 nm for M-0, M-I and M-II membranes, respectively. The difference in pore sizes is due to the difference in CVD time and precursor type. The obtained pores were larger than the 0.34 nm value reported by Hyun et al. [8] who used CVD to deposit only TEOS on the surface of γ-alumina membranes. The M-0 and M-I had approximate similar pore sizes, however, the presence of amine groups improved the CO_2/CH_4 separation. Even though M-II had pores larger than the CH_4 diameter (**Table 6**), the CO_2/CH_4 ratio was increased indicating that amine addition facilitated the CO_2 transport through the membrane. In this case, the secondary amine seems to favor CO_2 permeation better than the primary amine. As will be explained, this has to do with the basicity of the amine.

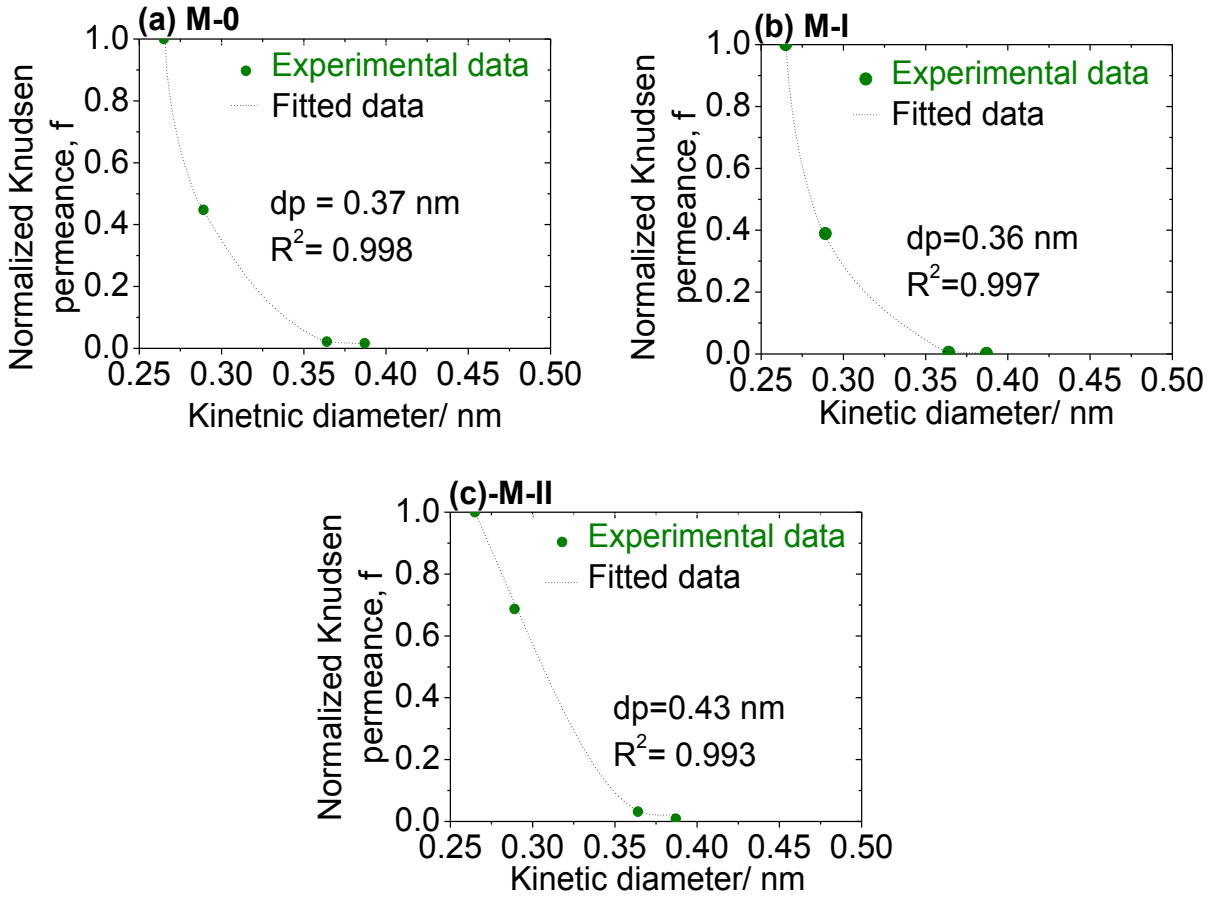

Fig. 20: Pore size estimation using Tsuru's method for (a) M-0, (b) M-I and (c) M-II membranes. The experimental permeances were measured at 503 K and 0.10 MPa and at the best CVD point. R^2 is the regression coefficient.

Yoshioka et al. [9] concluded that the NKP-plot method resulted in a rough estimation of the average pore size especially in the case of ceramic membranes having high affinity for CO_2. The authors corrected the normal f_{NKP} function by considering the activation energy and adsorption energy of each analyzed gas as written in **Eq. (24)**.

$$f_{mNKP} = \frac{\bar{P}_i}{\bar{P}_{He}}\sqrt{\frac{M_i}{M_{He}}}\,exp\left(-\frac{E_{P,He}-E_{P,i}}{RT}\right) = \frac{\left(1-{d_i}/{d_p}\right)^3}{\left(1-{d_{He}}/{d_p}\right)^3} \qquad \textbf{Eq.(24)}$$

where f_{mNKP} is the modified NKP function, E_P is the apparent activation diffusion behavior of gases, it is the summation of the attractive potential energy and the activation energy for the permeation of the considered gas (*i* is a gas species, *He* is the standard component in this case helium) [J mol^{-1}].

According to the authors, the value of E_p can be easily evaluated using **Eq. (25)**.

$$\bar{P}_{cKL} = \frac{k_{0,i}}{\sqrt{MRT}} \exp\left(-\frac{E_{P,i}}{RT}\right) \qquad \textbf{Eq. (25)}$$

where $\bar{P}_{cKL}$ is the Knudsen permeance of gas molecules that are concentrated by the attractive nature of the potential field of the pore wall, $k_{0,i}$ is a permeation constant for the i^{th} gas species [-].

The values of the adjusting parameters, $k_{0,i}$ and E_P, are obtained using **Eq. (25)** to fit the temperature dependency of each gas permeance to a curve (Appendix 1).

The new pore size is estimated using **Eq (24)** and following similar steps as for in normal NKP model. **Table 8** compares the results obtained using the NKP model (used previously in this section) and the modified NKP model. Since the permeance of CO_2 was not considered to estimate the pore size in NKP method presented in this section, pore sizes were similar to that of mNKP model.

Table 8: Pore size estimation using NKP and mNKP method

Membrane	Pore size [nm]	
	NKP method without considering CO_2 permeance	mNKP method
M-0	0.37	0.38
M-I	0.36	0.37
M-II	0.43	0.43

3.2.4 Microscopic structure

The SEM images were collected in order to have insight on the morphology of the selective layer. The surface of the synthesized membranes is shown in **Fig. 21**. The surfaces present a globular structure compared to the surface of the alumina intermediate layer before

conducting the CVD. It is likely that the decomposition of the silicate precursors deposits a thin film of silica which smoothens out the contours of the alumina particles that form the support [10]. The surfaces become smoother and more rounded after the CVD treatment. Morooka et al. [11] investigated the thermal decomposition of TEOS and suggested that TEOS molecules are adsorbed during the thermal treatment on the alumina surface and then decomposed to silica particles having globular shape. The average diameter of the globules was estimated as follow; first several circular features on the surface of the synthesized membranes were selected randomly, then the corresponding diameters were calculated. The average globule diameter were 29, 25 and 19 nm for M-0, M-I and M-II membranes, respectively.

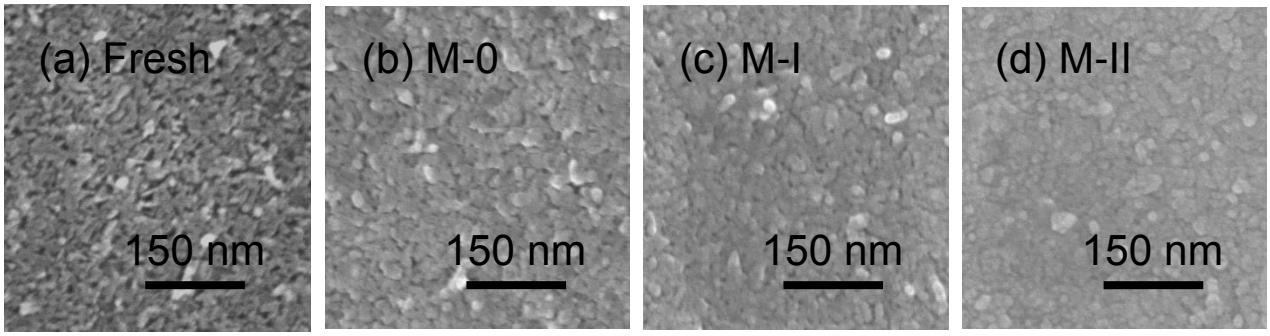

Fig. 21 : The top surface of (a) alumina intermediate layer before conducting CVD and (b) M-0, (c) M-I, and (d) M-II membranes at the optimum CVD time.

3.2.5 Membrane composition

The surface composition of the synthesized hybrid membranes was analyzed by XPS. The molar fractions are presented in **Table 9**. As expected, an N_{1s} signal was detected only on the surfaces of the M-I and M-II membranes. The M-II membrane had the highest carbon fraction possibly indicating that the terminate methyl group remained on the silane structure. The percentage of silica and oxygen were different because the CVD time was not the same for all membranes.

The N_{1s} spectra of M-I and M-II membranes are shown in **Fig. 22**. Two features can be observed in the spectra and can be assigned to free amine groups at a binding energy of 399 eV and protonated amine groups at a binding energy of 401 eV [12, 13, 14]. The presence of the protonated amine species indicated that carbamates intermediates were formed as a result of the interaction between CO_2 and the amine functionality for the M-I as well as M-II membranes.

Fernandes et al. [15] investigated the stability of several primary and secondary amine carbamate compounds and concluded that the formation of carbamates was not affected by the steric hindrance of the two -CH_2- groups bonded to nitrogen in the case of the secondary amine.

The ratio of N/Si of M-I and M-II were 0.033 and 0.029, respectively. The CVD was performed at relatively high temperature and in the presence of oxygen which might accelerate the decomposition of amine groups by pyrolysis or combustion. In the previous chapter, it has been demonstrated that there was a relationship between the obtained N/Si ratio at the end of CVD and the feed N/Si ratio. The calculation revealed that the N/Si ratios increased with the concentration of amino-functionalized precursor. These values were significantly lower compared to the expected N/Si ratios. However, the low ratio demonstrated that there is no need to increase to a higher amine concentration in these types of microporous hybrid membranes.

Table 9: Surface atomic composition of the synthesized hybrid membranes determined by XPS

Atomic composition (%)	**N_{1s}**	**C_{1s}**	**Si_{2p}**	**Al_{2p}**	**O_{1s}**
M-0	0.0	16	29	5.2	50
M-I	0.6	8.4	18	3.5	69
M-II	0.8	26	28	6.7	38

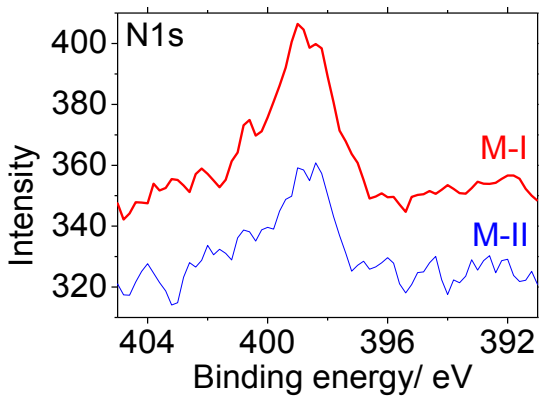

Fig. 22: The N_{1s} spectra of M-I and M-II membranes at the optimum CVD time.

3.2.6 Transport mechanism of CO_2 and CH_4 through membrane

The temperature dependence between 303-503 K of the permeance of various pure gases through the synthesized hybrid membranes was measured in order to determine the transport mechanism, focusing on CO_2 and CH_4 (**Fig. 23**). As before, the order of permeance generally followed the order of kinetic diameters. In the case of He, H_2, N_2 and CH_4, the permeances increased with temperature, indicating an activated diffusion transport mechanism through the membranes (**Fig. 23 (a, b and c)**). The diffusion activation energies of those gases can be estimated according to **Eq. (21)** (Chapter 2).

However, in the case of CO_2, the permeance passed through a maximum in the case of the M-I and M-II membranes. Hiyoshi et al. [16,17,18] demonstrated that CO_2 is completely desorbed from modified mesoporous silica SBA-15 after heating at 423 K. Therefore, it is likely that CO_2 permeated through these amine-modified silica membranes by repeated adsorption and desorption on the amino groups. Possible adsorption/desorption reactions for primary amines (**Eq. 26**) and secondary amines (**Eq. 27**) involve carbamate intermediates. **Table 10** lists the correspondent values.

$$2\,R-NH_2 + CO_2 \rightarrow R-NHCOO^- + R-NH_3^+ \qquad \textbf{Eq. (26)}$$

$$CO_2 + 2R_2NH \leftrightarrow R_2NH_2^+ + R_2NCO_2^- \qquad \textbf{Eq. (27)}$$

These reactions account for the facilitated transport. The detailed CO_2 and CH_4 permeances and selectivity for the M-0, M-I and M-II membranes are presented in **Fig. 23 (d, e and f)**.

The M-0 and M-I membranes show permeances for CO_2 of the order of 10^{-8} mol $m^{-2}s^{-1}Pa^{-1}$, whereas the M-II membrane shows a permeance of the order of 10^{-7} mol $m^{-2}s^{-1}Pa^{-1}$. The M-0 membrane shows little selectivity for CO_2 over CH_4. The M-I membrane shows a maximum selectivity of 70 at 363 K, while the M-II membrane shows a maximum selectivity of 140 at 343 K. The results are significant. A recent review of CO_2/CH_4 separation membranes concludes that permeances above the 10^{-8} mol $m^{-2}s^{-1}Pa^{-1}$ range and selectivities above 40 are in the range of commercial utilization [19].

The order of performance M-II > M-I > M-0 follows the order of base strength of the amine $2^o > 1^o > 0^o$ and reflects the ease of formation of the carbamate intermediate (**Eq. 26** and **Eq. 27**). Thus the order can be assigned to the balance between the adsorption, desorption, and

the surface diffusion of the CO_2 molecule. In the previous chapter, it was demonstrated that CO_2 permeated by a surface diffusion mechanism in amino-silica hybrid membranes using (3-aminopropyl) triethoxysilane as precursor. Titus [20] stated that in general terms, primary and secondary amines (sterically hindered or not) tend to react directly with CO_2, forming carbamates. The selectivity of the membranes shows no maximum for membrane M-0, a shallow maximum for membrane M-I, and a sharp maximum for membrane M-II. This supports the occurrence of the facilitated transport mechanism, in which adsorption, surface transport, and desorption take place depending on the presence of an amine group and its base strength. As temperature is raised adsorption and surface motion are enhanced due to the overcoming of activation barriers. However, once the temperature reaches higher values desorption occurs, decreasing the transport rate.

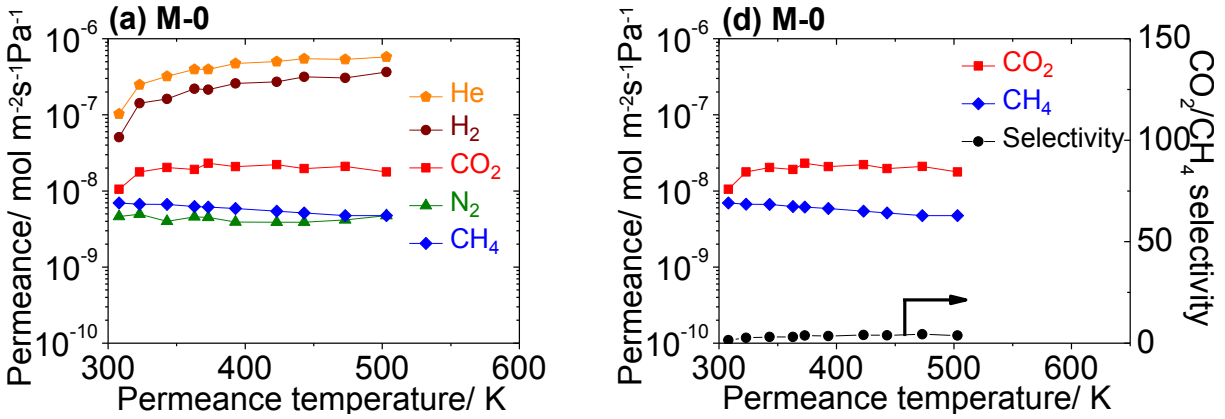

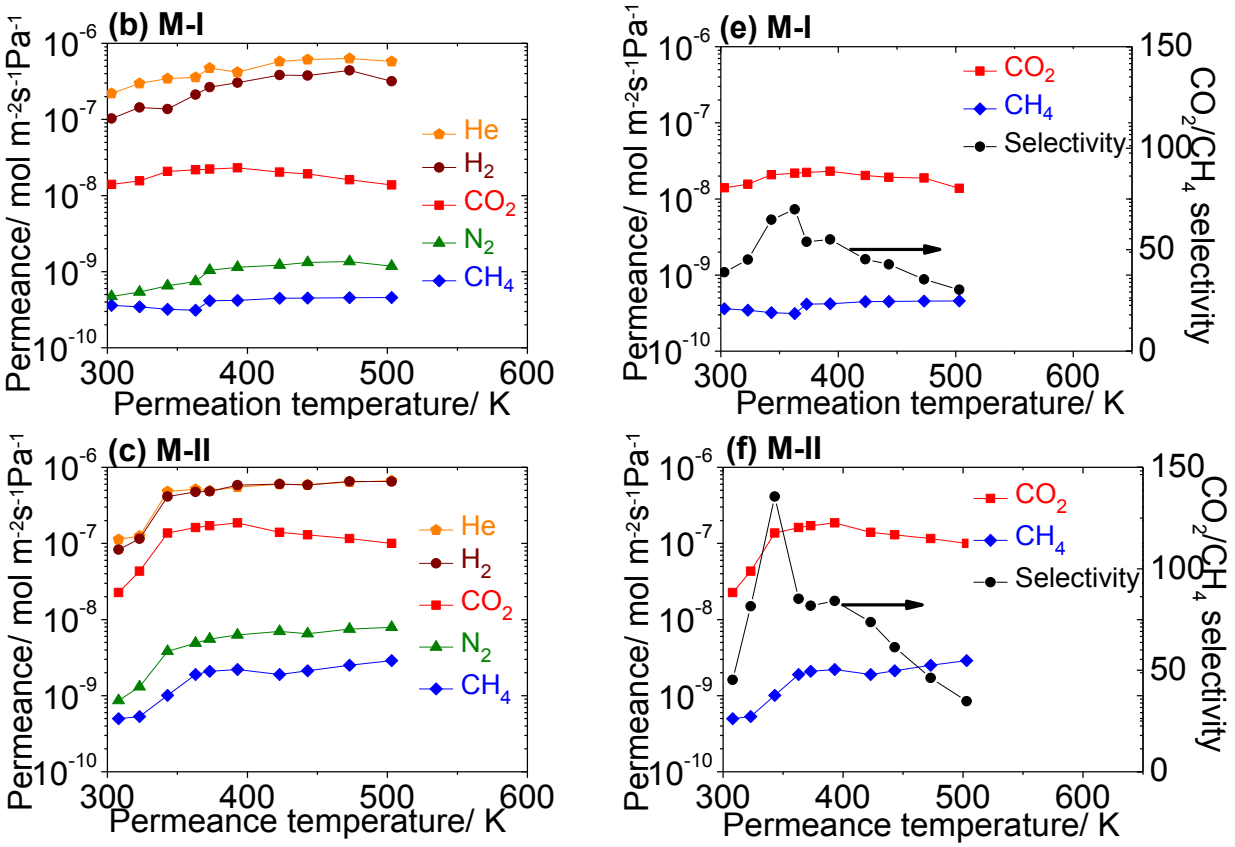

Fig. 23 : Temperature dependency of various gas permeances of (a) M-0, (b) M-I and (c) M-II membranes after 1.25 h, 2.75 h and 1.5 h CVD, respectively, measured at a pressure difference of 10 MPa. Detailed comparison of CO_2 and CH_4 gases of (e) M-0, (f) M-I and (g) M-II membranes at the same measurement conditions.

Table 10: Diffusion energies for He, H_2, N_2 and CH_4 through M-0, M-I and M-II membranes

Membrane	M-0	M-I	M-II
Gas	ΔE_{SD} (kJ mol^{-1})		
He	8.03	7.45	7.78
H_2	9.05	8.74	8.67
N_2	0.93	6.70	9.63
CH_4	0.54	3.91	9.38

The performance of the membranes is shown in a Robeson-type diagram (**Fig. 24**) where the CO_2 permeability is plotted as a function of CO_2/CH_4 selectivity. The permeability is the

product of the membrane permeance and the membrane thickness [21]. The thicknesses were estimated to be 30 nm for all synthesized membranes [**Error! Bookmark not defined.**,19,22].

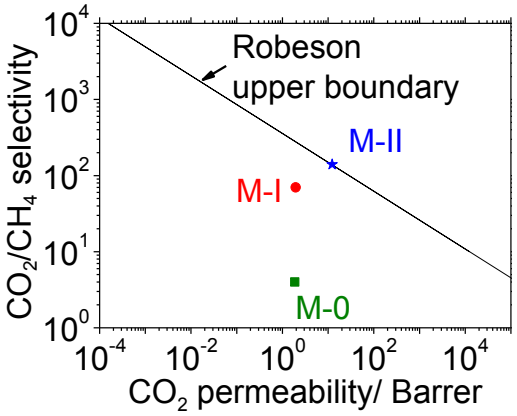

Fig. 24: Performance of the synthesized hybrid membranes in Robeson diagram for CO_2/CH_4 separation measured at 350 K and 0.1 MPa. The M-0, M-I and M-II stand for the free-amine, the primary amino and the secondary amino-silica membranes, respectively.

3.2.7 Mixed gas permeation properties

The CO_2/CH_4 separation factor of the M-0 and M-II membranes as a function of the permeation temperature (303-453 K) and the pressure difference (0.05-0.25 MPa) for a feed composition of CO_2:CH_4= 50:50 mol% are shown in **Fig. 25**. A detailed data comparing the CO_2/CH_4 ideal selectivities and CO_2/CH_4 separation factors as a function of the permeation temperature (303-453 K) and the pressure difference (0.05-0.25 MPa) for a various feed composition (CO_2:CH_4= 10:90; 50:50, and 80:20 mol%) for the M-II and M-0 membranes are shown in **Appendix 1** and **2**, respectively.

Concerning the M-II membrane (**Fig. 25 b** and **Appendix 2**), for a given pressure difference, as the temperature increased, the CO_2/CH_4 separation factor increased and passed through a maximum and then decreased. The obtained results support the previous conclusions in the previous section; as the temperatures increased the binding energy of CO_2 to the amine groups as well as its diffusivity increased. However, once the temperature reaches higher values desorption occurs, decreasing the transport rate. For a given temperature, the CO_2/CH_4 separation factor increased as the partial pressure of CO_2 is reduced. It is due to the fact that at higher CO_2 pressures the amine groups were saturated with the adsorbed CO_2 and thus they

hindered the movement of the gas phase. However, at low partial pressures, CO_2 have greater numbers of available sites to hop through, therefore, higher CO_2/CH_4 separation factors were obtained. Ostwal et al. [23] prepared amine modified silica membrane using 3-aminopropyltriethoxysilane to separate CO_2 and N_2. The authors observed an increase of the selectivity of the amine modified membranes from 2 in the case of single gas measurements to 10 in the case of mixed gas measurements (5% CO_2 and 95% N_2). They attributed the enhancement of the CO_2/N_2 separation factor in mixed gas measurements to the fact that N_2 was blocked by the adsorbed CO_2 due to the increased contribution of surface flow of CO_2.

Concerning the M-0 membrane (**Fig. 25 b** and **Appendix 3**), for a given pressure difference, as the temperature increased, the CO_2/CH_4 separation factor increased. No maximum was observed. The gas transport mechanism is activated by the temperature increase. The pair gas seems not to have great affinity with the pores walls.

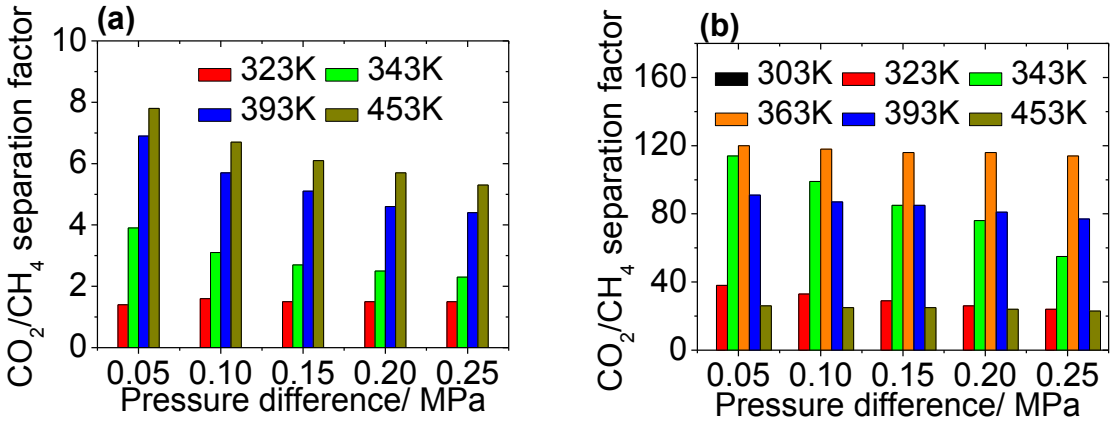

Fig. 25: The CO_2/CH_4 separation factor as a function of temperature and pressure difference for the (a) M-0 and (b) M-II membranes at a feed composition of CO_2:CH_4= 50:50 mol%.

3.2.8 Stability test

The effect of water vapor exposure on the CO_2 and CH_4 permeances through the M-II membrane is shown in **Fig. 26**. The overall permeance was stable for a 60 h exposure to a 20% relative humidity. The M-II membrane remained relatively stable compared to the M-0 and M-I membranes which lost their performances from the first minutes of exposure. It seems that the secondary amine functionality stabilized the silica membrane and avoided immediate membrane degradation. The results obtained with the M-II membrane can be explained based on previous

findings. Sayari et al. [24] exposed amine modified sorbent to a relative humidity between 0.4 to 74% at a temperature between 303 to 423 K and atmospheric pressure. They concluded that the amount of adsorbed CO_2 is enhanced by the presence of water in the stream gas. They pointed out that water can stabilize the amines surface groups upon CO_2 adsorption/desorption cycles. Mebane et al. [25] performed a parametric study on mesoporous silica supported amine sorbents. They demonstrated that silica-supported amines have limited capacity for the uptake of CO_2 in truly anhydrous conditions. The authors stated that water helped to form stable reactive intermediates. However, in **Fig. 26** an increase in selectivity was followed by a decrease as a function of time. It may be due to the length of the alkyl-amine chain as explained by Miyamoto et al. [26]. The authors fabricated amine-loaded mesoporous silica membranes for CO_2 separation using 3-trimethoxysilylpropyldiethylenetriamine (TA). The membrane showed high selectivity even under wet conditions. The authors suggested that both the long molecular length of TA and the affinity between the amine groups and polar molecules (water and CO_2) enhanced CO_2 separation. Therefore, in the case of the M-II membrane, the presence of water increased the amount of adsorbed CO_2, especially during the first hours of humidity exposure. However, the membrane degraded slowly as the exposure time increased. The XPS measurements of two repeated M-II membranes analyzed before and after steam exposure showed that the N/Si ratio did not change. Therefore, the water vapor did not destabilize the amine functionality.

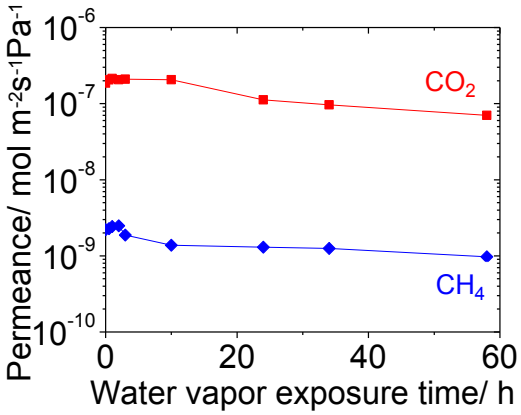

Fig. 26: Performance of M-II under 20% relative humidity measured at 393 K and 0.10 MPa.

3.3 Conclusions

Hybrid silica membranes were prepared using a chemical vapor deposition (CVD) method in order to enhance the separation of CO_2 from natural gas. Two alkylamine silane precursors having primary (3-aminopropyltrimethoxysilane) and secondary ((3-methylaminopropyl) trimethoxysilane) amine groups were selected to synthesize the selective layer because of the well-known affinity between CO_2 and amine functionalities. The obtained membranes were compared to an amine free membrane in order to understand the relationship between the microstructure and the performance of the alkylamine silica membranes. The highest separation performance was obtained at different CVD times for each membrane. The performance followed the order of base strength of the amine; secondary > primary > no amine. The highest performance was obtained with the secondary amine with a CO_2 permeance of $1.3x10^{-7}$ mol $m^{-2}s^{-1}Pa^{-1}$ and a CO_2/CH_4 ideal selectivity 140 measured at a temperature of 343 K and a pressure difference of 0.10 MPa. These values are of commercial significance, and indicate that the membranes are promising for practical applications. The mean pore size of the synthesized hybrid membranes were calculated by Tsuru's method and was estimated to be 0.37, 0.36, 0.43 nm for free, primary and secondary amino-silica membranes, respectively. Even though, the membrane with secondary amine group had the biggest pore size, the CO_2/CH_4 separation was the best. The transport of CO_2 through the amine modified silica layer was enhanced by the formation of carbamate intermediates which was verified by XPS analysis. Temperature dependence measurements indicated that CO_2 was transported by repeated adsorption/ diffusion/ desorption cycles. The membrane with secondary amine functionality was stable under 20% relative humidity during 60 h.

The obtained performance of the supported alkylamine membrane was in the shaded area presented in the introduction chapter which defined the desired area for commercial application. The selectivity was over 100 for secondary alkylamine membrane which is largely applicable to achieve a pipeline specification. The membrane was robust and stable at operating condition which makes them a potential candidate for industrial application.

3.4 References

[1] G.G. Paradis, R. Kreiter, M.M.A. van Tuel, A. Nijmeijer, and J.F. Vente, Amino-functionalized microporous hybrid silica membranes, J. Mater. Chem., 22 (2012) 7258 – 7264.

[2] D. W. Breck, Zeolite molecular sieves: Structure, chemistry, and use, Johm Wiley & Sons, New York, 1973.
[3] J. Tobin, P. Shambaugh, The crucial link between natural gas production and its transportation to market in: stages in the production of pipeline-quality natural gas and NGLs. 13.07.11, Available from: http://lba.legis.state.ak.us/sga/doc_log/2006- 01-01_eia_publication_natural_gas_processing.pdf
[4] N.S. Osborne, C.H. Meyers, A formula and tables for the pressure of saturated water vapor in the range 0 to 374 C, Research paper RP691, J. Res. Natl. Inst. Stan. 13 (1934) 1-10.
[5] S. T. Oyama , D. Lee, P. Hacarlioglu, R. F. Saraf**,** High permeability in a nonporous system: theory of hydrogen permeability in dense silica membranes, J. Membr. Sci. 244 (2004) 45-53.
[6] Y. Gu, S. T. Oyama, High molecular permeance in a pore-less ceramic membrane, Adv. Mater. 19 (2007) 1636-1640.
[7] H. R. Lee, M. Kanezashi, Y. Shimomura, T. Yoshioka, T. Tsuru, Evaluation and fabrication of pore-size-tuned silica membranes with tetraethoxydimethyl disiloxane for gas separation, AIChE. J. 57 (2011) 2755-2765.
[8] S.H. Hyun, S.Y. Jo, B.S. Kang, Surface modification of γ-alumina membranes by silane coupling for CO_2 separation, J. Membr. Sci 120 (2) (1996) 197.
[9] T. Yoshioka, M. Kanezashi, and T. Tsuru, Micropore size estimation on gas separation membranes:A study in experimental and molecular dynamics, AIChE J.l 59 (2013) 2179-2194.
[10] S. T. Oyama, D. Lee, S. Sugiyama, K. Fukui, Y. Iwasawa, Characterization of a highly selective hydrogen permeable silica membrane, J. Mater. Sci. 36 (2001) 5213.
[11] S. Morooka, S. Yan, K. Kusakabe, Y. Akiyama, Formation of hydrogen-permselective SiO_2 membrane in macropores of α-alumina support tube by thermal decomposition of TEOS, J. Membr. Sci. 101 (1995) 89-98.
[12] A.E. Hooper, D. Werho, T. Hopson, O. Palmer, Evaluation of amine- and amide-terminated self-assembled monolayers as 'Molecular glues' for Au and SiO_2 substrates, Surf. Interface Anal. 31 (2001) 809-814.
[13] E.T. Vandenberg, L. Bertilsson, B. Liedberg, K. Uvdal, R. Erlandsson, H. Elwing, I. Lundstrom, Structure of 3-aminopropyl triethoxy silane on silicon oxide, J. Colloid Interface Sci. 147 (1991) 103-118.
[14] A. Calvo, P.C. Angelome, V.M. Sanchez, D.A. Scherlis, F.J.Williams, G.J.A.A. Soler-Illia, Mesoporous aminopropyl-functionalized hybrid thin films with modulable surface and environment - responsive behavior, Chem. Mater. 20 (2008) 4661-4668.
[15] D. Fernandes, W. Conway, R. Burns, G. Lawrance, M. Maeder , G. Puxty, Investigations of primary and secondary amine carbamate stability by ^{1}H NMR spectroscopy for post combustion capture of carbon dioxide, J. Chem. Thermodyn. 54 (2012) 183–19.
[16] N. Hiyoshi, K. Yogo, T. Yashima, Adsorption of carbon dioxide on modified SBA-15 in the presence of water vapor, Chem. Lett. 33 (5) (2004) 510–511.
[17] N. Hiyoshi, K. Yogo, T. Yashima, Adsorption of carbon dioxide on aminosilane modified mesoporous silica, J. Jpn. Pet. Inst. 48 (1) (2005)29–36.
[18] N. Hiyoshi, K. Yogo, T. Yashima, Adsorption characteristics of carbon dioxide on organically functionalized SBA-15, Microporous Mesoporous Mater. 84 (2005) 357–365.
[19] D.D. Iarikov, S. T. Oyama, Review of CO_2/CH_4 Separation Membranes, in S.T.Oyama, S.M. Stagg-Williams (Eds.) Inorganic, polymeric, and composite membranes: Structure-function

and other correlations, Elsevier, Amsterdam, 2011.
[20] M. P. Titus, Porous inorganic membranes for CO_2 capture: present and prospects, Chem. Rev. 114 (2014) 1413−1492.
[21] T.H. McHugh, R. A-.Bustillos, and J.M Krochta, Hydrophilic edible films: Modified procedure for water vapor permeability and explanation of thickness effects, J. food Sci. 58 (2006) 899-903
[22] Y.S. Li, Microporous and dense inorganic membranes: current status and prospective, Sep. Purif. Technol. 25 (2001) 39-55.
[23] M. Ostwal, R.P. Singh, S.F. Dec, M.T. Lusk, J.D. Way, 3-Aminopropyltriethoxysilane functionalized inorganic membranes for high temperature CO_2/N_2 separation, J. Membr. Sci. 369 (2011) 139-147.
[24] A. Sayari, Y. Belmabkhout, Stabilization of amine-containing CO_2 adsorbents: dramatic effect of water vapor, J. Am. Chem. Soc. 132 (2010) 6312–6314.
[25] D.S. Mebane, J.D. Kress, C.B. Storlie, D.J. Fauth, M.L. Gray, and K. Li, Transport, zwitterions, and the role of water for CO_2 adsorption in mesoporous silica-supported amine sorbents, J. Phys. Chem. C, 117 (2013) 26617-26627.
[26] M. Miyamoto, A. Takayama, S. Uemiya, K. Yogo, Gas permeation properties of amine loaded mesoporous silica membranes for CO_2 separation, Desalin. Water Treat., 34 (2011) 266-271.

Chapter 4: Mixed Matrix Membranes for CO_2/CH_4 Separation

This Chapter is a modified version of a paper submitted in the Separation and Purification Technology:

S. Belhaj Messaoud, A. Takagaki, T. Sugawara, R. Kikuchi, S. T. Oyama, mixed matrix membranes using SAPO-34/polyetherimide for carbon dioxide/methane separation.

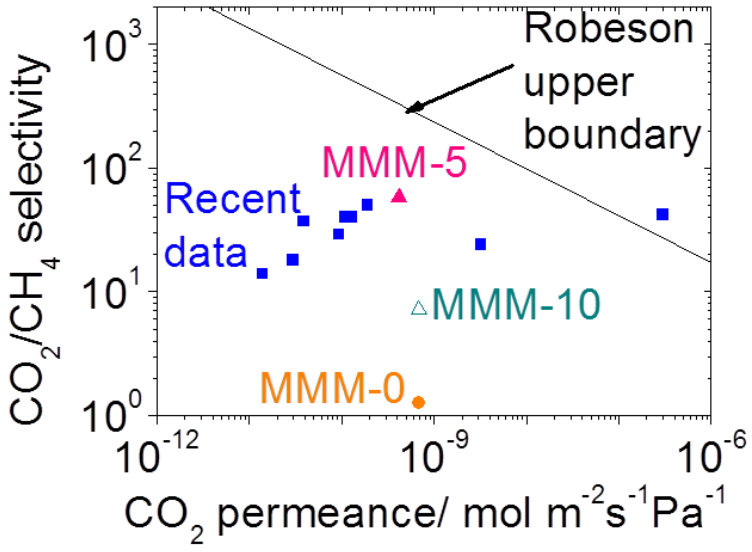

Overview

This chapter investigates the effect of adding inorganic particles into organic matrix on the performance of mixed matrix membranes (MMMs) for CO_2/CH_4 separation. Mixed matrix membranes (MMMs) are hybrid materials prepared by dispersing inorganic particles in a polymeric matrix and are attracting increasing attention for the separation of CO_2/CH_4 mixture. The SAPO-34 zeolite (**Fig. 27 a**) and polyetherimide (**Fig. 27 b**) were selected as the inorganic filler and the polymeric matrix for the synthesis of the supported MMMs. Two polymer solvents, dichloroethane and N-methyl-2-pyrrolidone, were investigated for the preparation, and the. dichloroethane solvent resulted in a membrane with better CO_2/CH_4 selectivity. Various SAPO-34 amounts from 0 to 10 wt% were dispersed in the polymer precursor which was dissolved in dichloroethane. The membrane with 5 wt% SAPO-34 content presented the highest performance with a CO_2 permeance of $4x10^{-10}$ mol $m^{-2}s^{-1}Pa^{-1}$ and a CO_2/CH_4 ideal selectivity of 60. Based on mixed gas permeances and time-lag measurements, the separation of CO_2 and CH_4 was found to be dominated by the difference in the gas solubilities. The SAPO-34 decreased CH_4 transport by increasing its diffusion pathway. Particle agglomeration was observed at 10 wt% zeolite loading in the polymeric matrix.

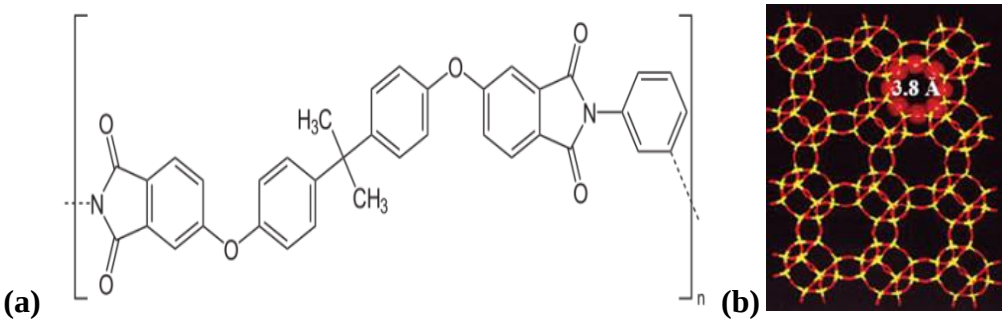

Fig. 27: (a) Polyetherimide (PEI) and (b) SAPO-34 chemical structure.

4.1 Experimental procedure

4.1.1 Materials

Porous alumina supports having an average pore size of 5 nm were obtained from the Pall Corporation. The supports were cut into 3 cm length and connected to dense alumina using glass joints as explained in previous **Chapters 2** and **3**. The glass was bought from the Nippon Electric Glass Co., Ltd. Ludox AS-40 colloidal silica (40 wt% suspension in water, Sigma Aldrich),

aluminum isopropoxide ($Al(O\text{-}iPr)_3$, > 99.99%, Sigma Aldrich), and phosphoric acid (H_3PO_4, 85 wt% in aqueous, Sigma Aldrich) were used as silica, alumina, and phosphoric oxide sources, respectively, to synthesize the SAPO-34 crystals. Tetraethylammonium hydroxide (TEAOH, 35 wt% in H_2O, Sigma Aldrich) was used as a structure directing agent in the crystal synthesis. Polyetherimide (PEI, MW30,000, Polysciences Inc.) was used as the polymeric precursor (**Fig. 27 a**). Dichloroethane (DCE, anhydrous, ≥ 99.8%, Sigma Aldrich), and N-methyl-2-pyrrolidone (NMP, anhydrous 99.5%, Sigma Aldrich) were used to investigate the effect of the polymer solvent on the resultant supported hybrid membranes. Pure Ar, H_2, CO_2, N_2, and CH_4 gases with a purity of 99.9% were acquired from Tokyo Koatsu Yamazaki Co., Ltd.

4.1.2 Membrane synthesis

4.1.2.1 SAPO-34 synthesis

The silicoaluminophosphate particles (SAPO-34) were prepared using a hydrothermal technique [1]. First, colloidal silica was mixed with TEAOH and hydrolyzed for 16 h at room temperature. Then, $Al(O\text{-}iPr)_3$ was vigorously stirred for 15 min in deionized water and H_3PO_4 was added drop wise to form an alumina gel. The mixture was stirred for 5 h. Then, the alumina gel was mixed with colloidal silica and stirred at room temperature for 3 days. The molar composition of the resultant synthesis solution was 1.0 Al_2O_3:1.0 P_2O_5:0.3 SiO_2:1.2 TEAOH: 60 H_2O. Crystal formation and growth was promoted by heating the solution to 473 K for 24 h in a Teflon-lined, stainless steel autoclave. The solid product was recovered by repeated centrifugation at 2700 rpm for 10 min and washing with deionized water. The precipitate was dried overnight at 393 K and then calcined at 823 K for 8 h. The heating and the cooling rates of the calcination were 1 K min^{-1}.

4.1.2.2 Membrane preparation

In a first investigation, two sets of polymeric precursors were prepared by dissolving PEI in either NMP or DCE solvent at room temperature with a PEI/solvent ratio of 6 wt%. After the dissolution of the polymer grains, mixed matrix membranes were prepared by dispersing mechanically 0, 5, and 10 wt% of the calcined and well-ground SAPO-34 in the polymer solution.

In a second investigation, only the DCE solvent was considered. The polymer to solvent ratio was also 6 wt%. After the dissolution of polymer grains, 0, 5, and 10 wt% of SAPO-34 were added to this precursor.

In both investigations, after the inorganic particles were dispersed, an ultrasonic treatment (AS ONE, US Cleaner AC 100V, 50/60Hz, 150W) for 30 min was conducted in order to release air bubbles and enhance SAPO-34 dispersion. The resultant mixture was used for the dip-coating (2 min) of the inner surface of an alumina support. The support was dried at room temperature overnight (**Fig. 28**).

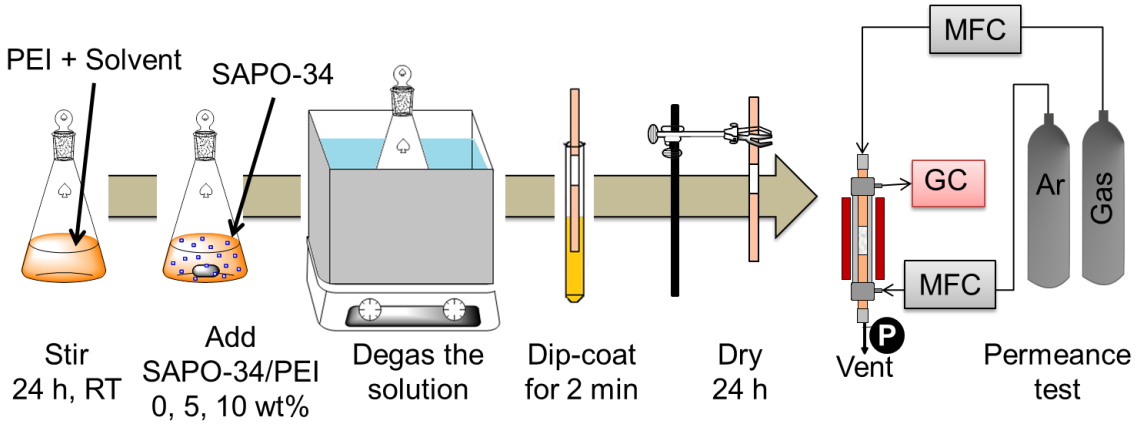

Fig. 28: Experimental procedure for the preparation of MMMs.

4.1.3 Characterization techniques

The crystalline state of SAPO-34 was determined by X-ray diffraction (XRD) (Rigaku, RINT 2400 instrument) operated at voltage 40 kV and current 100 mA. The specific surface area of SAPO-34 was evaluated by the BET method using nitrogen adsorption (Micromeritics, ASAP2000). The morphology of the obtained crystals, and MMMs were observed using a field emission scanning electron microscope (FE-SEM, Hitachi S-900). Membrane samples were prepared by mechanically breaking the membranes into small pieces. All samples were coated with a layer of Pt-Pd by ion sputtering (E-1030, Hitachi) with a current of 15 mA for 15 s. The permeance of all gases were determined by a gas chromatograph (GC, Shimadzu, TCD, GC-8A) equipped with a thermal conductivity detector. Argon was used as carrier gas (**Fig. 29 (a)**). The solubility and the diffusivity of CO_2 and CH_4 through MMMs were determined by time-lag method using the experimental set up in **Fig. 29 (b)**.

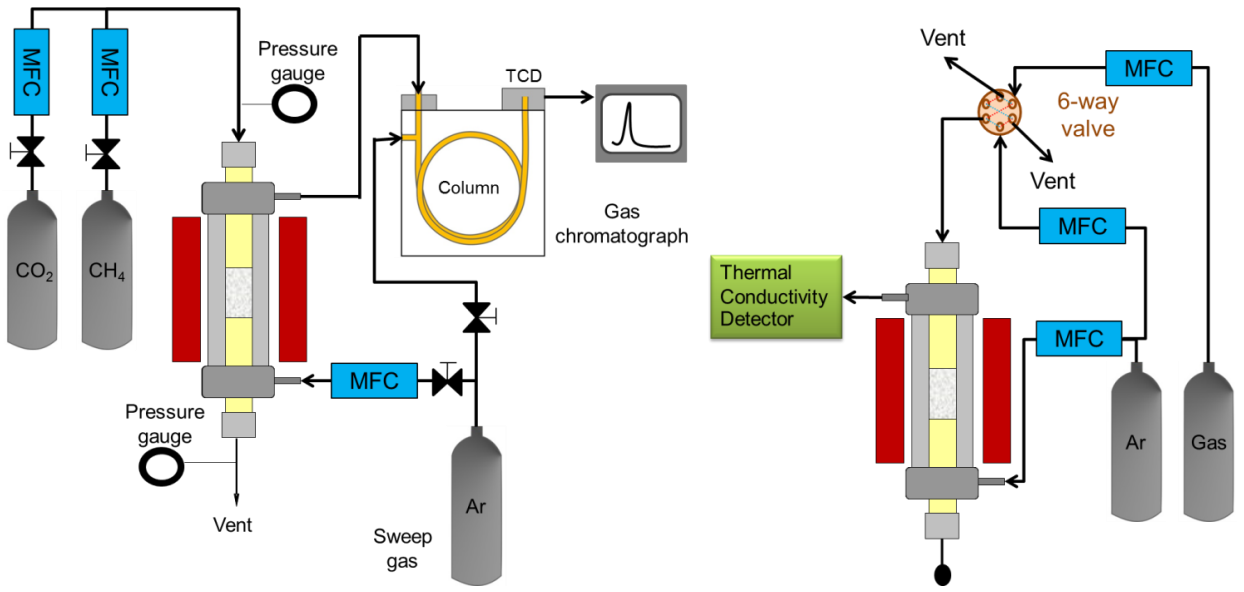

(a) **(b)**

Fig. 29: (a) Permeation measurement set up, (b) Experimental set up for time-lag measurements.

4.2 Results and discussions

4.2.1 SAPO-34 characterization

Fig. 30 (a) shows the XRD pattern of the prepared SAPO-34 and **Fig. 30 (b)** shows SEM image of the sample. The XRD pattern shows the characteristic peaks of pure SAPO-34 molecular sieves. The strong intensities indicate that the as-synthesized zeolite has high crystallinity. The SEM image shows thin plate or sheet like morphology with crystals of average length of 750 nm and thickness of 75 nm. Similar observations were reported by Tian et al. [2]. There are many shapes of SAPO-34 which depend on the synthesis parameters such as molar composition and the structure of the directing agent [3, 4].

The BET surface area and the micropores volume (**Table 11**) increased after the calcination indicating the success of the synthesis and formation of porous SAPO-34. The surface area was larger than the ones reported by previous studies such as 487 [5], 447 [6], 498 [7], 660 [8], 700 [9] $m^2 g^{-1}$.

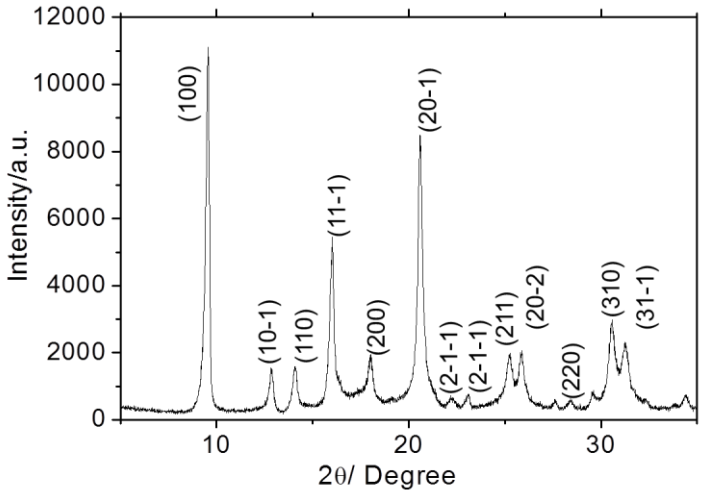

(a)

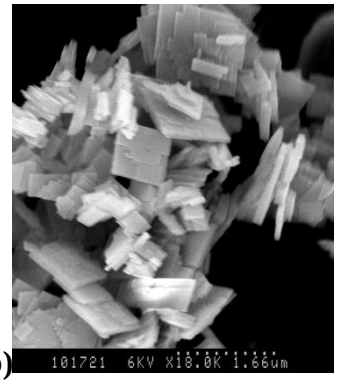

(b)

Fig. 30: (a) XRD patterns and (b) SEM image of the as-synthesized SAPO-34 crystals.

Table 11: Surface area and micropore volume of SAPO-34 before and after calcination.

Sample	**BET surface area ($m^2 g^{-1}$)**	**Micropore volume ($cm^3 g^{-1}$)**
Before calcination	28	No pore
After calcination	709	0.254

4.2.2 Solvent for polymeric precursor

Two solvents were tested to dissolve the polymer precursor; N-methyl-2-pyrrolidone (NMP) and dichloroethane (DCE). The N-methyl-2-pyrrolidone is a conventional solvent used in polyimide membranes. The dichloroethane dissolves PEI, and has higher vapor pressure and lower boiling point than the former solvent. The physical properties of DCE and NMP are displayed in (**Table 12**).

Table 12: Physical properties of DCE and NMP [10]

Solvent	Density ($g\ mL^{-1}$)	Viscosity (10^{-3} Pa s)	Boiling point (^oC)	Vapor pressure (Pa)
N-methyl-2-pyrrolidone	1.02	1.70	202	40
Dichloroethane	1.25	0.84	83	$11.6x10^3$

Two sets of mixed matrix solutions were prepared using NMP and DCE as solvent precursor with a PEI/solvent weight ratio of 6 wt% and SAPO-34/PEI concentrations of 0, 5 and 10 wt%. The performances of the obtained membranes as a function of SAPO-34 amount are shown in **Fig. 31**. It was observed that the neat polymeric membranes (SAPO-34/PEI = 0 wt%) in both sets were not selective for the separation of the pair gas. The difference in permeance through the neat membranes can be attributed to the solvent type [11]. Shao et al. [12] stated that solvents have various chemical and physical properties that induce different interactions with polymer chains. Therefore, the resultant polymeric membranes may have solvent-dependent morphologies and separation performances. The incorporation of SAPO-34 in the polymeric matrix affected differently the performance of the obtained membranes. In the case of the first set using NMP (**Fig. 31 a**), the permeance of CO_2 increased with the amount of SAPO-34, while the permeance of CH_4 remained stable. However, in the case of the second set using DCE (**Fig. 31 b**), the opposite behavior was observed, the permeance of CH_4 decreased compared to the permeance through the neat polymeric membrane, while the permeance of CO_2 remained stable. It seems that SAPO-34 in membranes using NMP behaved as a porous additive since the CO_2 permeance increased. However, it acted as a non-porous barrier when using DCE since no noticeable changes were observed in the CO_2 permeance. Membranes with 5 wt% SAPO-34 showed the highest performance with a CO_2 permeance of $2x10^{-9}$ mol $m^{-2}s^{-1}Pa^{-1}$ and a CO_2/CH_4 ideal selectivity of 12 in the case of membranes with NMP and a CO_2 permeance of $4x10^{-10}$ mol $m^{-2}s^{-1}Pa^{-1}$ and a CO_2/CH_4 ideal selectivity of 60 in the case of membranes with DCE. Earlier Chung et al. [13] stated that several variables can influence MMMs performances such as the combination of polymer/inorganic filler, the particle size, the particle sedimentation and agglomeration, and the polymer/inorganic filler interface morphologies. It can be concluded that

the precursor solvent plays an important role in defining the physical properties of the resultant polymeric matrix and the nature of the interaction between the polymer and the inorganic filler.

Membranes with 10 wt% SAPO-34 showed a decline of the ideal selectivity clearly observed in the set using DCE. It can be concluded that defects were created at 10 wt% additions allowing an increase of both CO_2 and CH_4 permeances and a decrease of CO_2/CH_4 selectivity. Similar observations were reported by Duval et al. [14] and Huang et al. [15] who found that higher zeolite content increased permeances and decreased selectivities.

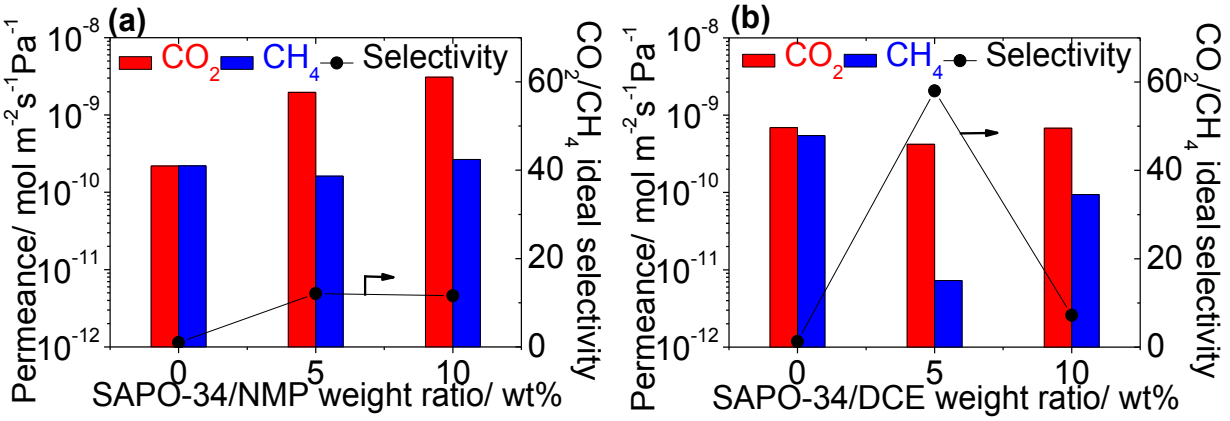

Fig. 31: Comparison between the effect of (a) NMP and (b) DCE solvents on the performance of the synthesized membranes measured at 303 K and 0.10 MPa.

The X-ray diffraction spectra of the synthesized membranes using DCE and NMP are presented in **Fig. 32**. The spectra showed the structural changes in MMMs as the solvent changes and as the amount of SAPO-34 increases. Generally, when a polymer contains large crystalline region, the XRD spectra shows sharp peaks with high intensity, while broader peaks and low intensity show amorphous region [16]. Pure PEI dissolved in both PEI and NMP showed one broad peak at $2\theta = 17^o$ indicating that both solvent did not change the crystallinity of the polymer [17]. The obtained PEI matrix was amorphous. Pure SAPO-34 presented sharp peaks (**Fig. 30 a**) with a highest peak intensity at $2\theta = 10^o$. The MMMs synthesized using NMP and DCE showed two features; one sharp peak attributed to the zeolite SAPO-34 at 10^o and one broad peak attributed to the polymer. The intensity of the sharp peak increased with increasing the amount of SAPO-34. In the case of membranes using NMP as solvent, the addition of 5 wt% SAPO-34 made the broad peak slightly sharper and changed a little its position to lower angles. Therefore,

the structure of the PEI was slightly disrupted by the incorporation of SAPO-34 which can explain the obtained enhancement of CO_2 permeance. However, in the case of membranes using DCE as solvent, the broad peak did not change. It can be surmised that the separation of CO_2 was affected by the structural state of PEI.

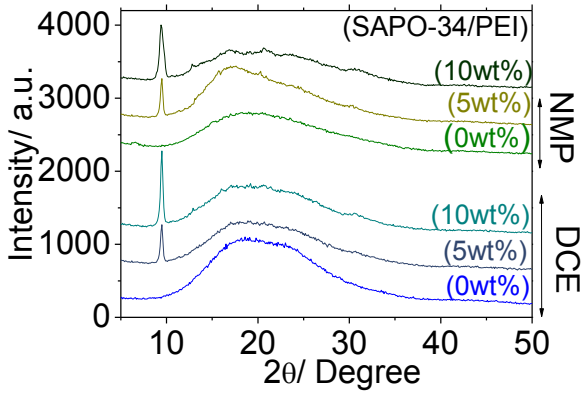

Fig. 32: XRD spectra of MMMs synthesized using NMP and DCE with various amount of SAPO-34.

It should be noted that membranes using NMP as precursor solvent needed six cycles of dip-coating and drying to achieve an appropriate separation performance, while membranes using DCE needed only one cycle for the separation. The thickness of membranes prepared using NMP was not uniform (**Fig. 31**). This can be attributed to the physical properties of the used solvents (**Table 12**).). As explained by Ahmad et al. [16] a long evaporation time of a membrane solvent may induce the sedimentation of the inorganic filler and consequently the formation of a membrane with non-homogeneous morphology. However, a low boiling point solvent requires less evaporation time and the sedimentation of the inorganic fillers may not have time to occur. According to these observations and permeation measurements, dichloroethane was selected as the MMMs solvent for further experiments because it required only one dip-coating/drying cycle and resulted in reasonable gas permeances and better CO_2/CH_4 ideal selectivity.

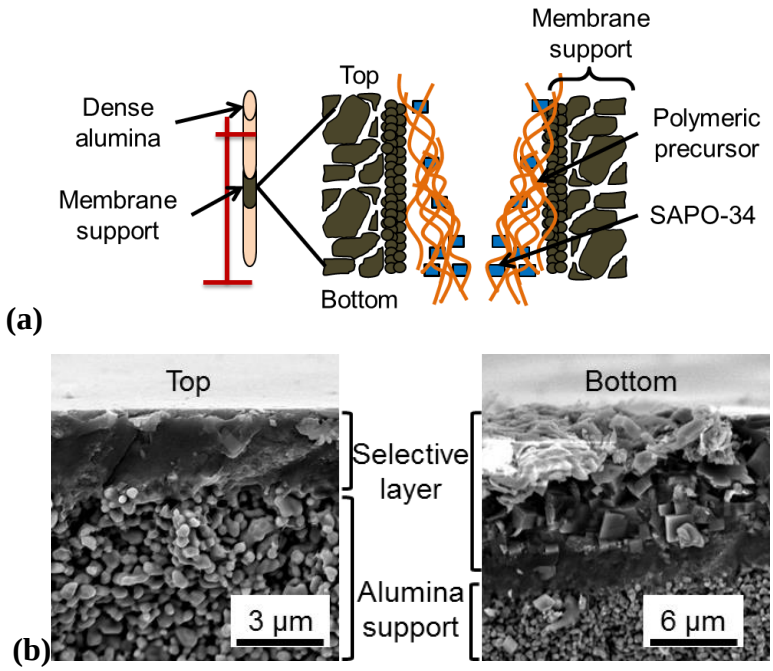

Fig. 33: (a) Drying process of the supported MMMs and (b) cross section image of membrane 5 wt% using NMP as polymeric solvent.

4.2.3 Single gas measurements

The permeance of various gases through the MMMs synthesized with the DCE solvent as a function of the kinetic diameter measured at 303 K and 0.10 MPa are shown in **Fig. 34**. From this section on, the membranes are named according to the SAPO-34 amount in the PEI/DCE precursor. Membranes with 0, 5, and 10 wt% SAPO-34/PEI are denoted MMM-0, MMM-5, and MMM-10, respectively. The permeance of the pure gases followed roughly the order of the kinetic diameter indicating a molecular sieving effect ($H_2 > CO_2 > N_2 > CH_4$). However, there were some deviations. In the case of MMM-0 and MMM-10 membranes, the permeance of CH_4 was higher than that of N_2, suggesting a shorter diffusion pathway for CH_4 which can be attributed to defects within the matrix. The addition of SAPO-34 affected mainly the permeances of bigger molecules such as N_2 and CH_4. The ideal selectivity of smaller gases towards bigger ones improved, especially in the case of the MMM-5 membrane. The permeances of large gas molecules were higher in the case of MMM-10 membrane than that of the MMM-5 membrane. This can be explained by SAPO-34 agglomeration when present in high amount in the matrix. When SAPO-34 particles were agglomerated N_2 or CH_4 had fewer barriers to overcome (**Fig. 35 c**). The MMM-10 looked like MMM-0 to some extent especially because the permeances of H_2

and CO_2 were similar (**Fig. 34** and **Fig. 35 a and c**). However, it seems that in the case of the MMM-5 membrane, particles were homogeneously dispersed resulting in longer pathways for N_2 and CH_4 (**Fig. 35 b**).

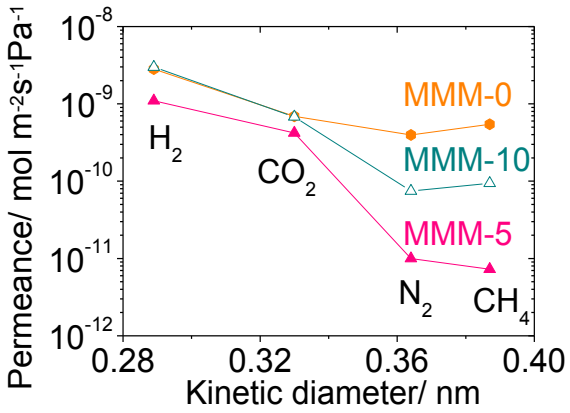

Fig. 34: Permeance of various pure gas molecules through MMM-0, MMM-5 and MMM-10 measured at 303 K and 0.10 MPa.

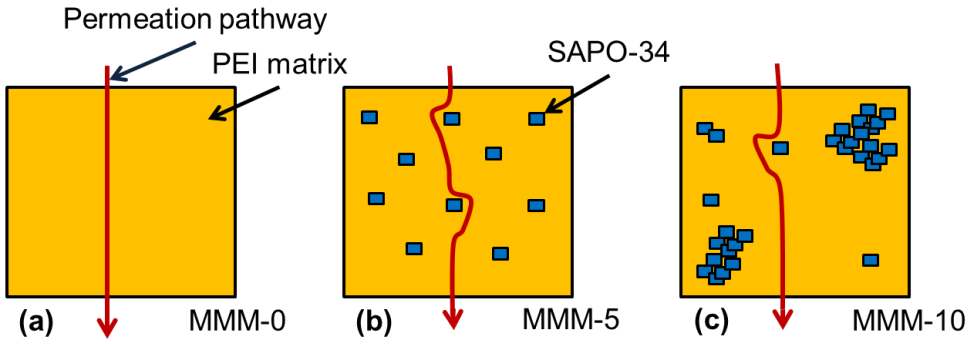

Fig. 35: Representation of the permeation pathway of N_2 and CH_4 in the synthesized membranes.

The performance of the obtained MMMs are presented in a Robeson type diagram and compared to recent work on MMMs (**Fig. 36**). The MMM-5 membrane presented a noticeable improvement compared to MMM-0. The MMM-5 is potentially attractive when compared with recently reported MMMs.

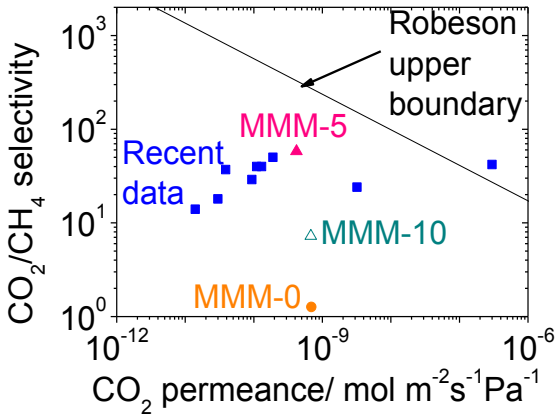

Fig. 36: Performance of the synthesized membranes presented in Robeson diagram compared with recent MMMs data for the CO_2/CH_4 separation [18,19,20,21,22,23,24,25].

4.2.4 Mixed gas measurements

The permeation behavior of a gas mixture is generally different from those of the single gases [26]. Mixed gas selectivity was evaluated at a CO_2:CH_4 molar ratio of 50:50 and was compared with single gas results (**Fig. 37**). The single gas measurements were performed at 0.05 MPa in order to maintain the partial pressure of gases equal to that corresponding to a 50:50 mixture. Both measurements were carried out at 303 K. In the case of the neat polymeric membrane MMM-0, the CO_2/CH_4 selectivity of the gas mixture was similar to that for ideal selectivity suggesting no competitive solubility or diffusion of the gases in this type of membrane. However, differences were observed when SAPO-34 particles were incorporated indicating a change in the permeation behavior.

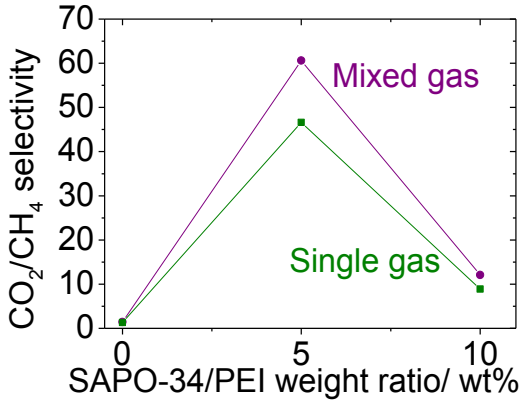

Fig. 37: Comparison between CO_2/CH_4 ideal and separation selectivities as a function of SAPO-34 amount in the polymeric matrix measured at 303 K and 0.05 MPa for single gas and at 303 K, 0.10 MPa and 50:50 mol% for mixed gas.

The effect of temperature and the pressure difference on the separation performance of the equimolar mixture CO_2/CH_4 were investigated. First, the temperatures were varied from 303 to 393 K under a pressure difference of 0.10 MPa, and the results are summarized in **Fig. 38**. The CO_2/CH_4 ideal selectivity was also shown for comparison. The performance of the synthesized membranes showed a similar trend compared to the ideal gas selectivity. In the case of the MMM-0 membrane, the ideal selectivity was almost similar to the separation factor in the mixed gas system. The permeances of both gases were similar indicating the absence of any competition between CO_2 and CH_4 in order to cross the neat polymeric membrane (**Fig. 38 a**). However, in the case of the MMM-5 and MMM-10 membranes, higher separation factors were observed with the mixtures. The reason can be attributed to competitive permeance or a hindrance effect between the gas pairs in the membrane. The permeance of CO_2 hardly changed, while the permeance of CH_4 increased from 303 to 393 K for the MMM-5 and MMM-10 membranes. It can be said that the solubility of CH_4 was significantly hindered by that of CO_2, leading to higher selectivity in the mixed gas system (**Fig. 38 b and c**).

Second, the effect of the pressure difference on the separation performance was investigated in the range between 0.05 and 0.20 MPa under a permeation temperature of 303 K (**Fig. 39**). The CO_2 permeance changed slightly (**Fig. 39 b and c**). However, the CH_4 permeance decreased with the increase of pressure difference reflecting high concentration dependence. This dependency did not occur in MMM-0 (**Fig. 39 a**).

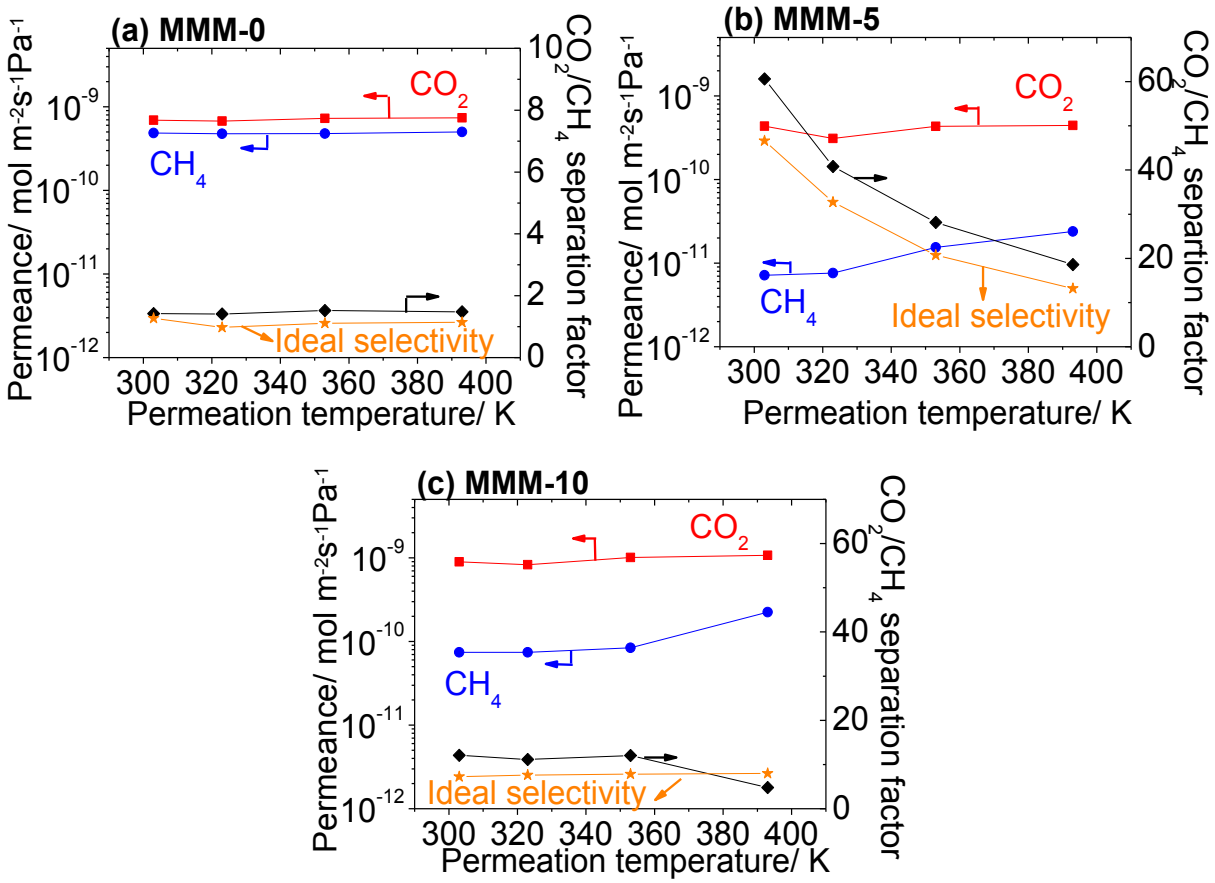

Fig. 38: Permeances and separation factors of the equimolar CO_2:CH_4 mixture as a function of permeation temperature under a pressure difference of 0.10 MPa for (a) MMM-0, (b) MMM-5, and (c) MMM-10 membranes.

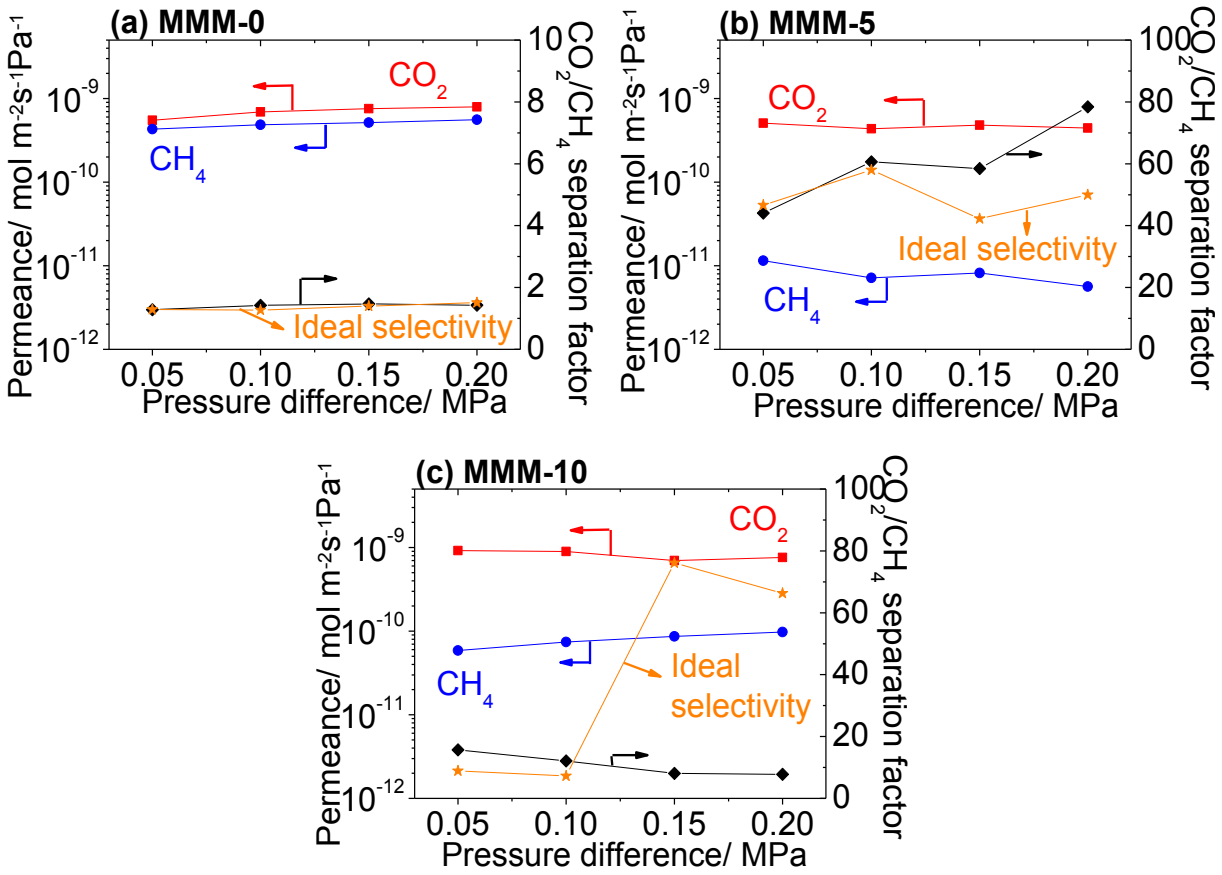

Fig. 39: Permeances and separation factors of the equimolar CO_2:CH_4 mixture as a function of pressure difference measured at 303 K for (a) MMM-0, (b) MMM-5, and (c) MMM-10 membranes.

4.2.5 Calculation of gas diffusivity and solubility

As explained in **Chapter 1**, gas molecules permeate through polymeric membranes by the solution-diffusion mechanism. The mechanism is mainly controlled by the diffusivity and the solubility of the permeated gases in the polymeric matrix and by the thickness of the membrane (**Eq. (6)**). Time-lag measurement is an experimental method that determines gas solubility and diffusivity. It was performed in order to understand the effect of the addition of SAPO-34 to gas diffusivities and solubilities in the MMMs. The experiments were carried out at 303 K and 0.10 MPa. Solubility and diffusivity can be written as in **Eq. (10)** and **Eq. (11)**, respectively. At time zero, a precise amount of CO_2 or CH_4 was injected into the membrane at the feed side. The amount of gas permeated through the membrane gradually increased until reaching a steady state. The total amount of permeated gas as a function of time is shown in **Fig. 40 a**. The response of

CO_2 and CH_4 were similar for the case of MMM-0 membrane. The addition of SAPO-34 affected mostly the CH_4 response. The cumulative quantities of the permeated gas as a function of time are shown in **Fig. 40 b**. The x-intercept determined the time-lag (**Eq. (10)**), while the slope of the line determined the flux at the steady state (**Eq. (11)**). The MMM-5 membrane had the smallest slope for both gases. The obtained results are displayed in **Table 13**. The addition of SAPO-34 affected clearly the time-lag of CH_4.

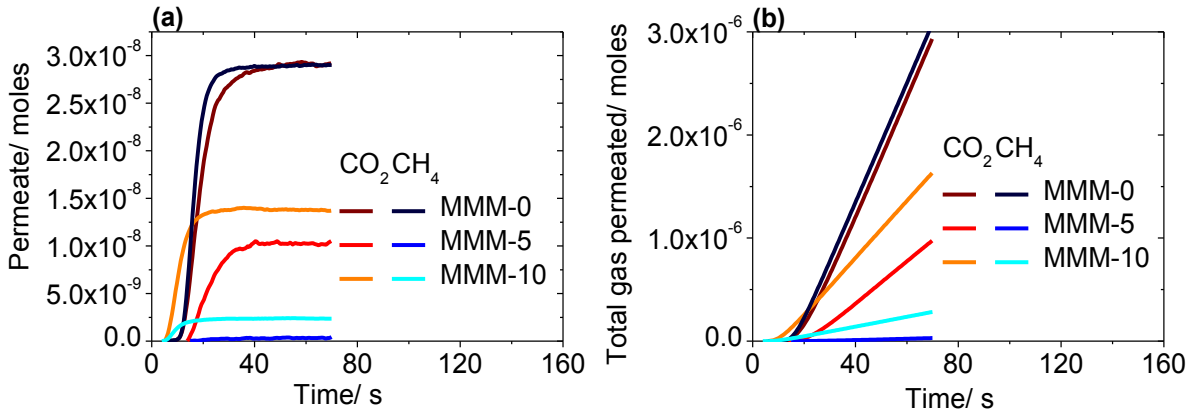

Fig. 40: (a) Response curves for the time-lag measurements, and (b) time-lag curves of CO_2 and CH_4 measured at 303 K and 0.10 MPa for the MMM-0, MMM-5, and MMM-10 membranes.

Table 13: Slopes, y-intercepts and time-lag of 0, 5, 10, 15 and 20 wt% SAPO-34/PEI MMMs of the cumulative quantity of permeated gases.

Gas	CO_2		
Membrane	MMM-0	MMM-5	MMM-10
Slope ($x10^{-8}$) ($mol\ s^{-1}$)	6	2	5
y-intercept ($x10^{-7}$) (s)	-10	-5	-11
Time lag (s)	20	22	21

Gas	CH_4		
Membrane	MMM-0	MMM-5	MMM-10
Slope ($x10^{-9}$) (mol s^{-1})	60	0.7	5
y-intercept ($x10^{-8}$) (s)	-0.9	-2	-5
Time lag (s)	15	29	10

The solubilities and the diffusivities of CO_2 and CH_4 through the synthesized MMMs are shown in **Fig. 41 a and b**, respectively. The zeolite affected mainly gas solubility, while the diffusivity was stable. Therefore, SAPO-34/PEI membranes separated CO_2 and CH_4 by differences in solubility and both gases competed for the solubility sites as was concluded for the mixed gas experiments. At the temperature of permeance and time lag measurement, 303 K, the diffusivity does not change with SAPO-34 content, but the solubility of CH_4 goes down. This could be because the SAPO-34 crystallites occupy the matrix volume that would otherwise contribute to solubility. The CO_2 solubility goes down a little, indicating that CO_2 can enter the zeolite. The diffusivity is not changed because the temperature is too low and there is little transport through the SAPO-34. Indeed, when temperature is increased the permeance of both gases increases.

A comparison between the single gas permeance experimentally obtained and calculated using the time-lag method is shown in **Fig. 42**. Even though the permeances obtained from the two methods were slightly different, they were consistent and confirmed the accuracy of the experimental procedure. The differences might be related to the experimental errors and the assumption of membrane thickness.

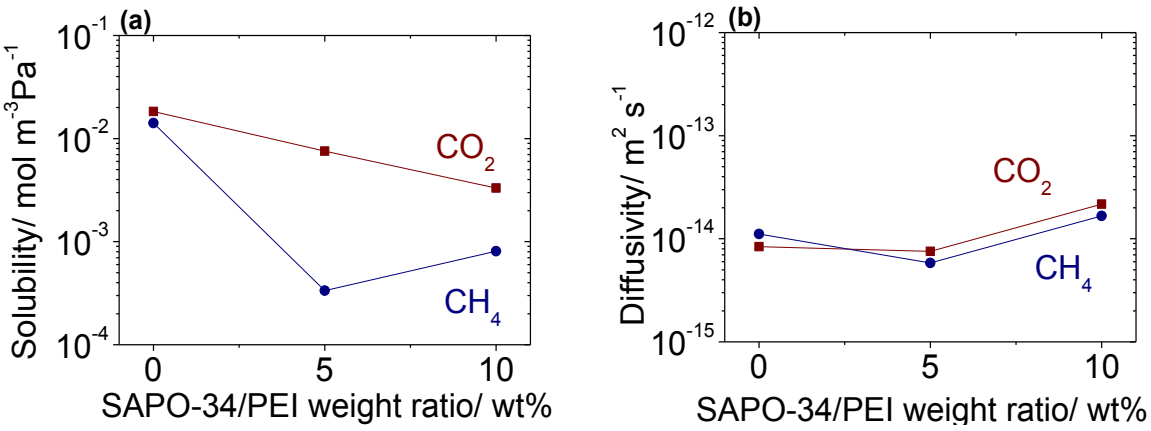

Fig. 41: (a) Solubility and (b) diffusivity of CO_2 and CH_4 in SAPO-34-PEI membranes as a function SAPO-34 loading obtained at 303 K and 0.10 MPa.

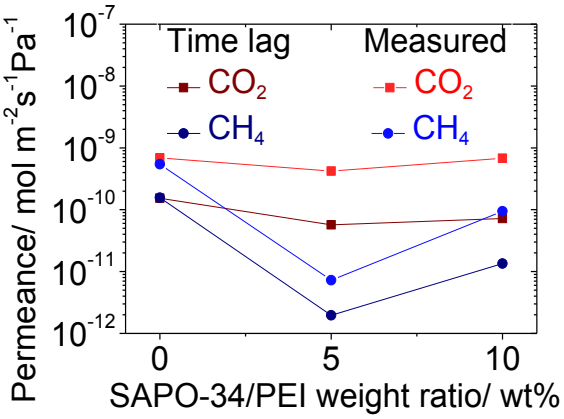

Fig. 42: Comparison between measured permeance and calculated permeance using time-lag method as a function of SAPO-34 loading assuming a membrane thickness of 1 μm.

4.2.6 Microscopic structure

The surfaces of the obtained MMMs are shown in **Fig. 43**. The MMM-0 and MMM-5 membranes had defect free surfaces. However, the MMM-10 membrane presented particle agglomeration. Evidently, the agitation and the ultrasonic treatment were not enough to disperse the zeolite in the matrix. The absence of trend in the permeance measurements, especially for the high SAPO-34 content membrane, can then be explained by the presence of agglomeration and holes within the selective layer. The agglomeration is due to the incompatibility (difference of affinity) between the SAPO-34 surface and the polymer chains. Chung et al. [13] stated that precipitation of zeolites may occur during MMM preparation because of the very different

physical properties and difference in density between zeolite and polymers. Bastani et al. [27] attributed the particle agglomeration in MMM especially at high zeolite loading to the sedimentation or surface pattern (migration to the surface). Therefore, the probability of voids formation was increased. The thickness of the MMM-5 membrane was 1 μm.

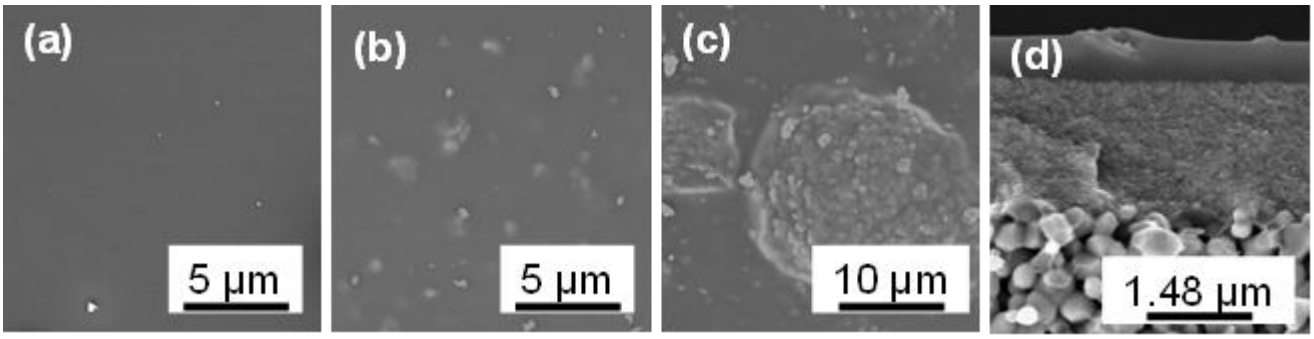

Fig. 43: The top surface of the synthesized MMMs; (a) 0, (b) 5, (c) 10, (d) 15, (e) and (f) 20 wt% SAPO-34/ PEI, and (g) the cross section of 5 wt% membrane.

4.3 Conclusions

Mixed matrix membranes were synthesized by dispersing zeolite SAPO-34 in polyetherimide polymer. Dichloromethane was selected to dissolve the polymer rather than N-methyl-2-pyrrolidone; a conventional solvent used for the polyetherimide membranes since the former solvent resulted in a homogeneous selective layer and gave high CO_2/CH_4 selectivity. Various SAPO-34 amounts from 0 to 10 wt% were dispersed in the polymer precursor dissolved into dichloroethane. A membrane with 5 wt% SAPO-34 loading presented the highest performance with a CO_2 permeance of 4.41×10^{-10} mol $m^{-2}s^{-1}Pa^{-1}$ with a CO_2/CH_4 selectivity of 60. The separation occurred based on the difference in gas solubility. The SAPO-34 decreased CH_4 permeance by increasing its diffusion pathway. Higher loading caused the agglomeration of the zeolite particles.

4.4 References

[1] G. Li, J. Yang, J. Wang, W. Xiao, L. Zhou, Y. Zhang, J. Lu, D. Yin. Thin carbon/SAPO-34 microporous composite membranes for gas separation J. Membr. Sci. 374 (2011) 83–92

[2] Y. Tian, L. Fan, Z. Wang, S. Qiu and G. Zhu. Synthesis of a SAPO-34 membrane on macroporous supports for high permeance separation of a CO_2/CH_4 mixture. J. Mater. Chem. 19 (2009) 7698–7703.

[3] M.A. Carreon, S. Li, J.L. Falconer, and R.D. Noble. SAPO-34 Seeds and Membranes Prepared Using Multiple Structure Directing Agents. Adv. Mater. 20 (2008) 729–732.
[4] E. Peyman, F. Shohreh, A.T. Siamak. Effect of synthesis parameters on phase purity, crystallinity and particle size of SAPO-34. Iran. J. Chem. Chem. Eng. 30 (2011) 29-36.
[5] S.R. Venna, and M.A. Carreon, Amino-Functionalized SAPO-34 Membranes for CO_2/CH_4 and CO_2/N_2 Separation, Langmuir 27 (2011) 2888-2894.
[6] S.R. Venna, and M.A. Carreon, Microwave assisted phase transformation of silicoaluminophosphate zeolite crystals, J. Mater. Chem. 19 (2009) 3138-3140.
[7] M.U.M. Junaidi, C.P. Khoo, C.P. Leo, A.L. Ahmad, The effects of solvents on the modification of SAPO-34 zeolite using 3-aminopropyltrimethoxy silane for the preparation of asymmetric polysulfone mixed matrix membrane in the application of CO_2 separation, Microporous Mesoporous Mater. 192 (2014) 52-59.
[8] J.K. Das, N. Das, and S. Bandyopadhyay, Effect of PVP intermediate layer on the properties of SAPO 34 membrane, Adv. Mater. Sci. Eng., (2012) 7, doi:10.1155/2012/650217.
[9] J. Surendar, R. Venna, and M.A. Carreon, Synthesis of SAPO-34 crystals in the presence of crystal growth inhibitors, Phys. Chem. B 112 (2008) 16261-16265.
[10] R. Scarlet, L.R. Manea, I. Sandu, L. Martinova, O. Cramariuc, I.G. Sandu, Study on the Solubility of polyetherimide for nanostructural electrospinning. Rev.Chim. 7 (2012) 688-692.
[11] T. Sener, E. Okumus, T. Gurkan, and L. Yilmaz, The effect of different solvents on the performance of zeolite-filled composite pervaporation membranes, Desalination 261 (2010) 181-185.
[12] L. Shao, T.S. Chung, G. Wensley, S.H. Goh, and K.P. Pramoda, Casting solvent effects on morphologies, gas transport properties of a novel 6FDA/PMDA-TMMDA copolyimide membrane and its derived carbon membranes, J. Membr. Sci. 244 (2004) 77-87.
[13] T. Chung, L.Y. Jiang, Y. Li, S. Kulprathipanja, Mixed matrix membranes (MMMs) comprising organic polymers with dispersed inorganic fillers for gas separation, Prog. Polym. Sci. 32 (2007) 483-507.
[14] J.M. Duval, B. Folkers, M.H.V. Mulder, G. Desgrandchamps, C.A. Smolders, Adsorbent filled membranes for gas separation, Part 1: Improvement of the gas separation properties of polymeric membranes by incorporation of microporous adsorbents, J. Membr. Sci. 80 (1993) 189-201.
[15] Z. Huang, J. Su, X. Su, Y. Guo, L. Teng, C.M. Yang, Preparation and permeation characterization of β-zeolite-incorporated composite membranes, J. Appl. Polym. Sci. 112 (2009) 9-18.
[16] J. Ahmad, M.B. Hägg, Development of matrimid/zeolite 4A mixed matrix membranes using low boiling point solvent, Sep. Purif. Technol. 115 (2013) 190-197.
[17] C. R. Desper, A.J. Hsieh, and N.S. Schneider, Transient crystallization of an aromatic polyetherimide: effect of annealing, Polymer research branch, U.S. army materials technology laboratory (1991) 1473-1487.
[18] S. Shahid, N. Nijmejer, Performance and plasticization behavior of polymer-MOF membranes for gas separation at elevated pressures, J. Membr. Sci. 470 (2014) 166-177.
[19] W. Qiu, K. Zhang, F.S. Li, K. Zhang, W.J. Koros, Gas separation performance of carbon molecular sieve membranes based on 6FDA-mPDA/DABA (3:2) polyimide, Chem. Sus. Chem. 7 (2014) 1186-1194.
[20] W.N.W Salleh, A.F. Ismail, T. Matsuura, M.S. Abdullah, Precursor selection and process

conditions in the preparation of carbon membrane for gas separation: A review, Sep. Purif. Rev. 40 (2011) 261-311.
[21] T. Rodenas, M. van Dalen, E. Garcia-Perez, P. Serra-Crespo, B. Zornoza, F. Kapteijn and J. Gascon, Visualizing MOF mixed matrix membranes at the nanoscale: Towards structure-performance relationships in CO_2/CH_4 Separation Over NH_2-MIL-53(Al)@PI, Adv. Funct. Mater. 24 (2014) 249-256.
[22] N. Du, H.B. Park, M.M. Dal-Cin and M.D. Guiver, Advances in high permeability polymeric membrane materials for CO_2 separations, Energy Environ. Sci. 5 (2012) 7306-7322.
[23] A. Ambrosetti, P.L. Silvestrelli, Gas separation in nanoporous graphene from first principle calculations, J. Phys. Chem. 118 (2014) 19172-19179.
[24] W.E.V. Perez, K.J. Balkus Jr., J.P. Ferraris, I.H. Musselman, Mixed-matrix membranes containing MOF-5 for gas separations, J. Membr. Sci. 328 (2009) 165-173.
[25] S. Matteucci, V.A. Kusuma, S.Swinnea, B.D. Freeman, gas permeability, solubility and diffusivity in 1,2-polybutadiene containing brookite nanoparticles, Polymer 28 (2008) 757-773.
[26] A.B. Fuertes, D.M. Nevskaia, T.A. Centeno, Carbon composite membranes from Matrimid and Kapton polyimides for gas separation, Micropor. Mesopor. Mater. 33 (1999) 115-125.
[27] D. Bastani, N. Esmaeili, M. Asadollahi, Polymeric mixed matrix membranes containing zeolites as a filler for gas separation applications: A review, J. Ind. Eng. Chem. 19 (2013) 375-393.

Chapter 5: Robeson Upper Boundary Optimization for CO_2/CH_4 Separation

This Chapter is a modified version of a paper submitted in the chemical engineering research and design: B. Castro-Dominguez, P. Leelachaikul, S. Belhaj Messaoud, A. Takagaki, T. Sugawara, R. Kikuchi, S. T. Oyama, The Optimal Point within the Robeson Upper Boundary.

Example: CO_2/N_2

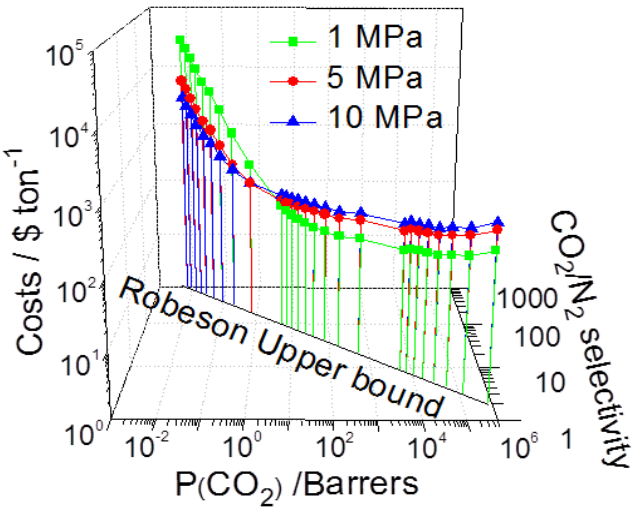

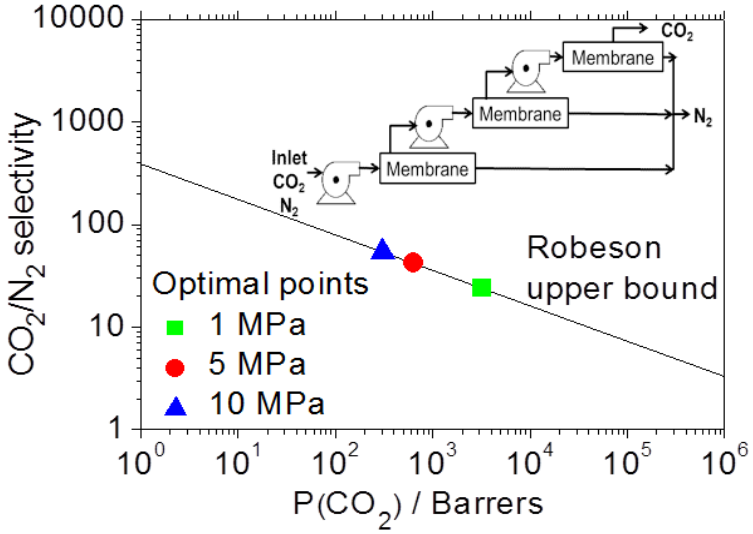

Overview

The Robeson correlation is an empirical plot that shows a tradeoff between selectivity and permeability of gases whose upper boundary is often used to evaluate the performance of a membrane system. This chapter shows that it is possible to define an optimum permeability/selectivity point on this boundary based on economic optimization. Examples are presented for the separation of four gas pairs: CO_2/N_2, O_2/N_2, CO_2/CH_4, and N_2/CH_4. The constraints used to limit the optimal point are based on the cost of the membrane, the number of units required to achieve a specific separation, and the compression requirements. The total costs include the fees for utilities and capital costs, and interest payments. The model results are verified against other studies, while initial and targeted parameters are subject to a sensitivity analysis. The optimum points obtained at an operating pressure of 1 MPa were for CO_2/N_2 a permeability of 3,200 barrers and a selectivity of 24, for O_2/N_2 a permeability of 550 barrers and a selectivity of 4, for CO_2/CH_4 a permeability of 2,000 barrers and a selectivity of 20, and for N_2/CH_4 a permeability of 110 barrers and a selectivity of 2.

5.1 Simulation Parameters

This work involves a mathematical analysis of membranes in a serial cascade, which is the most direct arrangement for implementing a separation. As shown in **Fig. 44**, the permeate stream is sent through a series of *n* membrane units and *n* centrifugal compressors to achieve a given purity. Generally in practice, recompression of the permeate stream is often not implemented to avoid complexity. However, the present model presents recompression for each stage in order to make an analysis at the same pressure, and also to consider identical staged units, in order not to make assumptions about process operations. The simulation accounts for recovery, production target, purity of species and the permeation properties of the membranes. The following assumptions were made for the development of the mathematical model to optimize the membrane separation process:

- Negligible pressure drop and composition change within a membrane unit (perfect mixing).
- Constant unit recovery (r) for all stages.
- Invariant permeability and selectivity of the gases in all stages.
- Constant pressure difference (ΔP) between the feed and permeate in each stage.

- Unaltered operating temperature of 298 K.

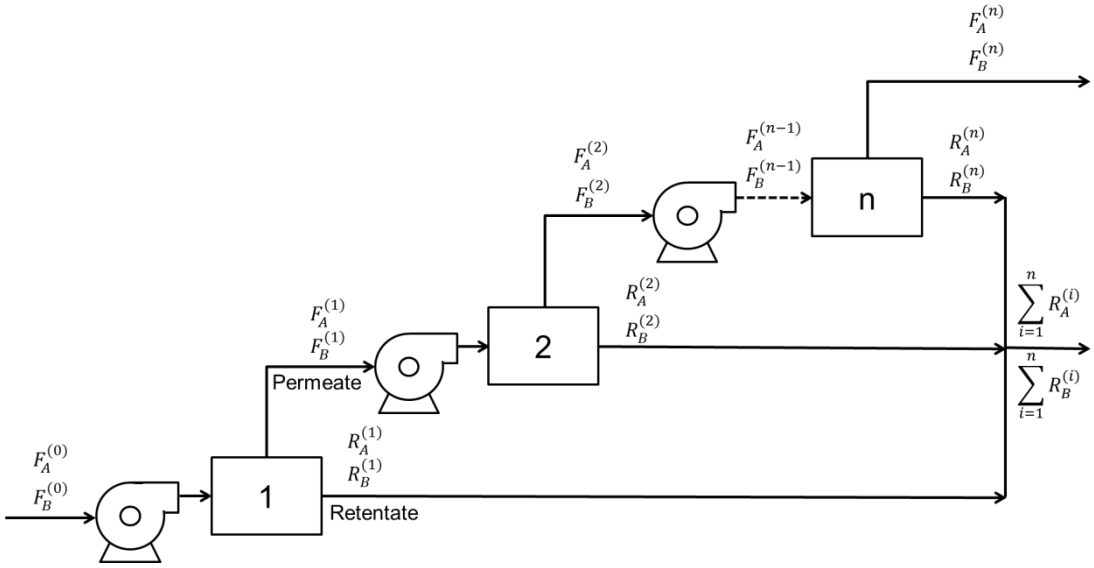

Fig. 44 : Membrane process configuration.

For simplicity the present simulation does not make assumptions of co-current or counter-current flow and takes the concentration difference to be constant. This perfect mixing assumption might not be the case in actual units since the permeation of gases makes the gas partial pressure difference vary along the membrane length. A comparison of partial pressure difference among ideal, co-current and counter-current cases will be presented and discussed in **section 5.4.1**.

The simulation was performed with MATLAB 7.0.4 and was designed to calculate the capital and operating costs that polymeric membranes have at specific permeabilities and selectivities within the Robeson's upper limit. Several parameters including product purity, recovery, operating pressure, membrane selectivity and membrane thickness were investigated to find an optimum cost required for the separation of CO_2/N_2, O_2/N_2, CO_2/CH_4 and N_2/CH_4 gas streams. The gas pairs are listed in the order of their permeances, so the first species is the permeating species and the second is the retained species. In the separation of CO_2/N_2 the targeted product was in the permeate stream while in the other three (O_2/N_2, CO_2/CH_4 and N_2/CH_4) the desired product was in the retentate. In this chapter species "A" represents the gas that permeates faster and exits with the permeate, while "B" represents the species that permeates slower and remains in the retentate. A reasonable thickness of the selective layer of all

membranes was assumed to be 1 μm [1,2,3] to convert to barrers, which is used in the Robeson plot.

Case I: Main product (A) in permeate

The selectivity (α), purity of A (Pur_A) and number of membrane units (n) for stages (in superscripts) are mathematically related as shown in **Eqs. (28)-(30)**.

$$\boldsymbol{\alpha} = \frac{\bar{P}_A^{(i)}}{\bar{P}_B^{(i)}} = \frac{F_A^{(i)}/A_i \Delta P_A^{(i)}}{F_B^{(i)}/A_i \Delta P_B^{(i)}} = \frac{F_A^{(i)}}{F_B^{(i)}} \frac{F_B^{(i-1)}}{F_A^{(i-1)}} \quad \textbf{Eq. (28)}$$

$$\frac{F_A^{(n)}}{F_B^{(n)}} = \boldsymbol{\alpha}^{\boldsymbol{n}} \frac{F_A^{(0)}}{F_B^{(0)}} \quad \textbf{Eq. (29)}$$

$$\boldsymbol{Pur_A} = \frac{F_A^{(n)}}{F_A^{(n)} + F_B^{(n)}} \quad \textbf{Eq. (30)}$$

where $\bar{P}_A^{(i)}$ is the permeance of gas A at stage i (mol $m^{-2}s^{-1}Pa^{-1}$), $\bar{P}_B^{(i)}$ is the permeance of gas B at stage i (mol $m^{-2}s^{-1}Pa^{-1}$), $F_A^{(i)}$ is the molar flow rate of gas A in the permeate stream at stage i (mol s^{-1}), $F_B^{(i)}$ is the molar flow rate of gas B in the permeate stream at stage i (mol s^{-1}), A_i is the membrane area required for stage i (m^2), and Pur_A is the purity of gas A. Substituting **Eq. (29)** into **Eq. (30)** yields the number of units required to reach a specific product purity as shown in **Eq. (31)**.

$$\boldsymbol{n} = \frac{\boldsymbol{log}\left(\boldsymbol{Pur_A} \cdot \boldsymbol{F_B^{(0)}} / (\boldsymbol{1} - \boldsymbol{Pur_A}) \cdot \boldsymbol{F_A^{(0)}}\right)}{\boldsymbol{log}(\boldsymbol{\alpha})} \quad \textbf{Eq. (31)}$$

The trade-off relationship between permeability (P) and selectivity is based on the Robeson's upper limit in polymeric membranes [18] as represented in **Eq. (32)**. In this equation the constants k and m are shown in **Table 14**.

$$P = k\alpha^m \quad \textbf{Eq. (32)}$$

Table 14 : Parameters k and m for Robeson's upper bound curve [18]

Gas pair	k (barrers)	m
CO_2/N_2	31,000,000	-2.89
O_2/N_2	1,400,000	-5.67
CO_2/CH_4	5,370,000	-2.64
N_2/CH_4	2,600	-4.51

The recovery of species A (r_A) for each unit is defined in **Eq. (33)**, while the overall recovery (Rec_A) is shown in **Eq. (34)**. Their relationship was obtained as shown in **Eq. (35)**.

$$\mathbf{r_A} = \frac{F_A^{(i)}}{F_A^{(i-1)}} \qquad \textbf{Eq. (33)}$$

$$\boldsymbol{Rec_A} = \frac{F_A^{(n)}}{F_A^{(0)}} \qquad \textbf{Eq. (34)}$$

$$\mathbf{r_A} = \boldsymbol{Rec_A^{1/n}} \qquad \textbf{Eq. (35)}$$

Furthermore, the molar flow rate of gas A at stage *i* ($F_A^{(i)}$) and the permeance of gas B at stage *i* ($F_B^{(i)}$) were computed as in **Eqs. (36)-(37)**.

$$\boldsymbol{F_A^{(i)} = r_A^i F_A^{(0)}} \qquad \textbf{Eq. (36)}$$

$$\boldsymbol{F_B^{(i)} = F_A^{(i)} \frac{F_B^{(0)}}{F_A^{(0)}} \frac{1}{\alpha^i}} \qquad \textbf{Eq. (37)}$$

The area of the membrane required in each unit *i* is expressed by **Eq. (38)**. The power required for each compressor ($PWR_{Comp}^{(i)}$, kW) was computed according to **Eq. (39)** [4].

$$\boldsymbol{A^{(i)} = \frac{F_A^{(i)}}{\bar{P}_A} \frac{(F_A^{(i-1)} + F_B^{(i-1)})}{\Delta P \cdot F_A^{(i-1)}}} \qquad \textbf{Eq. (38)}$$

$$\boldsymbol{PWR_{Comp}^{(i)} = (8.277 \times .2^{-3}) \left(\frac{F^{(i)} T_I}{\eta}\right) \left(\frac{K}{K-1}\right) \left[\left(\frac{P_O}{P_I}\right)^{K\prime - 1/K\prime} - 1\right]} \qquad \textbf{Eq. (39)}$$

where η is the compressor mechanical efficiency, assumed to be 60%, T_I the inlet temperature (K), P_I the inlet compressor pressure (Pa), P_O the outlet compressor pressure (Pa), K' the gas specific heat ratio (C_p/C_v), assumed to be 1.4. The molar flow rate $F^{(i)}$ in **Eq. (39)** is in mol s^{-1}.

The economic evaluation required the estimation of the capital cost for each membrane unit ($C_M^{(i)}$, \$) and compressor ($C_{Comp}^{(i)}$, \$) which were computed according to **Eqs. (40)-(41)** [4]. The area $A^{(i)}$ in **Eq. (39)** has units of m^2 and $PWR_{Comp}^{(i)}$ in **Eq. (40)** of kW. Note that capital costs have a chemical engineering (CE) plant cost index of 394 (2002) as specified by Seider et al. [4].

$$\boldsymbol{C_M^{(i)} = 377\, A^{(i)}} \qquad \textbf{Eq. (40)}$$

$$\boldsymbol{C_{Comp}^{(i)} = F_M F_D \left(exp\left\{7.4580 + 0.80\left[ln\left(PWR_{Comp}^{(i)}\right)\right]\right\}\right)} \qquad \textbf{Eq. (41)}$$

The material and design factors (F_M and F_D) corresponded to 5.0 and 1.25, respectively [4]. Utilities included the electricity needed to run the compressors. The utility cost (C_U, \$ yr^{-1}) for the process was computed by **Eq. (42)** where the power required for the compressors ($PWR_{Comp}^{(i)}$) in **Eq. (42)** is in kW [5]. The number of compressors starts from stage 0 (before entering the first stage) to stage n-1 (before entering the final stage). Therefore, (*i-1*) was used to indicate the compressor for stage *i* in **Eq. (37)**.

$$\boldsymbol{C_U = 0.045\left(\sum_{i=1}^{n} PWR_{Comp}^{(i-1)}\right)(operating\ hours\ per\ year)} \qquad \textbf{Eq. (42)}$$

The annual cost was used as the economic indicator as suggested by Seider et al. [4] and a rate of return of 20% was assumed as a reasonable internal interest rate. Other costs included in this model include factors to account for 1) piping and additional equipment (10% of compressor cost) 2) purchase price markup (50% of total capital cost) and 3) installation (15% of total capital cost) [5]. The annual cost for each gas separation process (C, \$ yr^{-1}) was estimated utilizing **Eq. (43)**. The flow diagram utilized in this simulation is shown in **Fig. 45**.

The objective function is the total cost for producing the targeted gas which is a function of capital costs and utilities. The capital costs are distributed based on the assumption of having a return of investment 20% (**Eq. 43**).

$$\boldsymbol{C = C_U + (0.2)(1.5)(1.15)\sum_{i=1}^{n}(C_M^{(i)} + 1.1C_{Comp}^{(i-1)})} \quad \textbf{Eq. (43)}$$

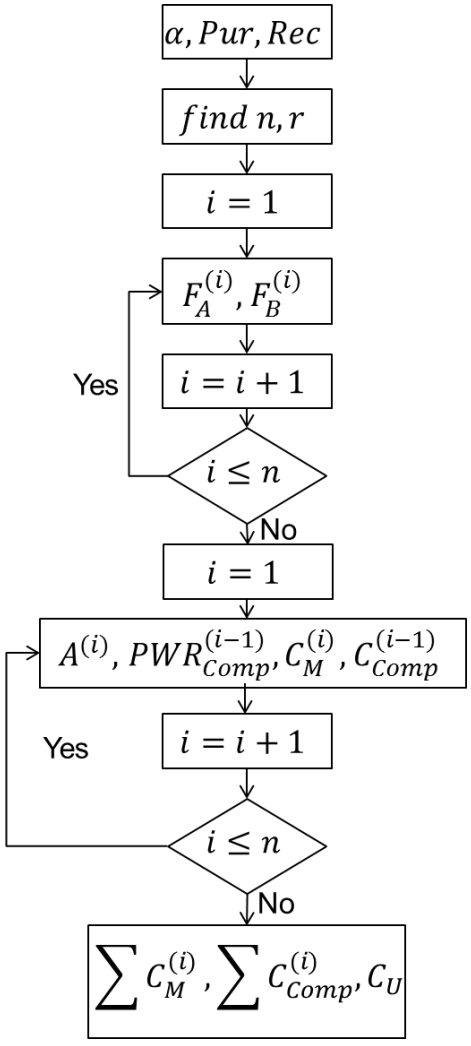

Fig. 45 : Flow diagram of the simulation program.

Case II: Main product (B) in retentate

In this case, the purity of B (Pur_B) and overall recovery of B (Rec_B) in the retentate was targeted. In order to use the simulation above, the purity of A (Pur_A) and recovery of A (Rec_A) in the permeate phase needed to be calculated from **Eqns. (44)-(45)** below.

$$\boldsymbol{Rec_B = \frac{\sum_{i=1}^{n} R_B^i}{F_B^0} = \frac{F_B^{(0)} - F_B^{(n)}}{F_B^{(0)}}} \qquad \textbf{Eq. (44)}$$

$$\boldsymbol{Pur_B = \frac{\sum_{i=1}^{n} R_B^i}{\sum_{i=1}^{n} R_A^i + \sum_{i=1}^{n} R_B^i} = \frac{F_B^{(0)} - F_B^{(n)}}{\left(F_A^{(0)} - F_A^{(n)}\right) + \left(F_B^{(0)} - F_B^{(n)}\right)}} \qquad \textbf{Eq. (45)}$$

Rearranging **Eqs. (44)** and **(45)**.

$$F_B^{(n)} = (1 - Rec_B) F_B^{(0)} \qquad \textbf{Eq. (46)}$$

$$\boldsymbol{F_A^{(n)} = \frac{Pur_B \cdot F_A^{(0)} - (1 - Pur_B)(F_B^{(0)} - F_B^{(n)})}{Pur_B}} \qquad \textbf{Eq. (47)}$$

$F_A^{(n)}$ can be obtained from **Eq. (47)**, and then the purity and recovery of A in the permeate can be calculated.

5.2 Validation of the model

The validation of the model consisted of comparing the costs reported in the literature to the values obtained in this simulation. The gas pair chosen for this validation was the purification of O_2 from air since it is a simple, yet important separation [18]. This work considers the process analyzed by Gollan and Kleper [5] for oxygen enrichment.

The process consists of an increase in the atmospheric oxygen concentration (21%) to 35% by utilizing one membrane unit with a selectivity of 3.5 to 6 and capacity of 1 to 20 ton day^{-1} requiring a constant electric consumption of 177 kWh ton^{-1}. One stage is required to achieve the desired separation with an O_2 recovery of 50%. The cost reported by Gollan and Kleper [5] for this separation was estimated between \$20 to \$30 ton^{-1}.

The present simulation was run assuming a selectivity of 4.75, a membrane thickness of 100 μm and a transmembrane pressure drop of 65 kPa to achieve an energy consumption of 181 kWh ton^{-1}. These assumptions were made in order to keep the parameters consistent with those presented earlier [5].

The simulation performed in the present study showed that enriched O_2 with a 50% recovery and an O_2 concentration of 35% costs \$26 ton^{-1}. The cost obtained of \$26 ton^{-1} (394 CE index, 2002), was converted to \$21 ton^{-1} (323 CE index, 1984) to compare with the costs reported in the literature; suggesting that the simulation model predicts valid operational costs.

5.3 Results and Discussion

5.4.1 Ideal, co-current and counter-current flows

Ideal flow (perfect mixing), counter-current flow and co-current flow were examined in order to investigate the effect of flow patterns on the partial pressure difference between the feed and the permeate. The calculation was performed for a single membrane unit to reach the product purity and recovery as shown in **Table 15.** As expected, the results show that the partial-pressure difference decreases in the order; ideal > counter-current > co-counter. The point though is that the differences are not immense, so that for a first-order analysis as in this study the assumption is adequate. The objective of this paper is to demonstrate that there is an optimal point in the Robeson upper boundary, something that has not been considered before. More refined studies that consider more realistic flow patterns and membrane process design are needed before installing a membrane process in industry.

Table 15: Comparison of partial pressure difference among ideal, co-current and counter-current flows at a total feed pressure of 1.1 MPa.

Gas pairs (A/B)	Feed composition	Product Purity	Recovery	Partial pressure difference of gas A (MPa)		
				Ideal	Counter-current	Co-current
CO_2/N_2	15/85	CO_2 85%	CO_2 50%	0.17	0.09	0.05
O_2/N_2	21/79	N_2 90%	N_2 50%	0.23	0.15	0.14
CO_2/CH_4	20/80	CH_4 90%	CH_4 90%	0.22	0.12	0.13
N_2/CH_4	14/86	CH_4 90%	CH_4 99%	0.15	0.11	0.11

5.4.2 Operating conditions

Operating conditions and targets for the gas pairs presented are summarized in **Table 16**. These conditions consist of the targeted purity and recovery of the desired species, the capacity of production and raw composition of the gas mixture and the properties of the membrane such as thickness and cost ($\$ m^{-2}$). Each parameter is supported by the literature and its description is presented in detail in the following sections.

5.4.2.1 CO_2/N_2

The separation of N_2 from CO_2 is necessary for the recovery of CO_2 from flue gases. This separation requires a CO_2 with a purity of 95% with a minimum recovery of 90% as specified by Van der Luus et al. [6].

5.4.2.2 O_2/N_2

The separation of the O_2/N_2 gas pair is performed mainly to obtain purified nitrogen from air which is composed of 21% O_2 and 79% N_2. Baker [7] reported that the principal market for nitrogen is for 99% nitrogen purity. To achieve this separation nitrogen can be recovered to 50% by utilizing membranes that have selectivity of 8. It is reasonable to assume a recovery of 50% in

air separation since air does not have value. MVS Engineering Ltd. developed ZEN series models of membrane nitrogen generators with capacity of 150 tons day^{-1}. This number was used as a parameter in the simulation.

5.4.2.3 CO_2/CH_4 and N_2/CH_4

Methane is the most abundant component in natural gas, but CO_2 is an impurity that can be present in concentrations as high as 70% [7]. The concentration of CO_2 is desired to be reduced to less than 2 mol% as specified for pipeline quality gas [8]. Bhide and Stern [9] reported the production of CH_4 with a capacity of 510 tons day^{-1} with CO_2 feed concentrations of 5-40 mol%. Nitrogen is another impurity in natural gas that requires removal to have a high heating value of the fuel. The separation of CH_4 and N_2 is one of the most difficult gas separations as shown by Robeson's upper limit [18]. Nitrogen can be in concentrations as high as 15% and requires its removal to a concentration of < 4% to have a pipeline quality gas.

Table 16 summarizes the values used for the various gas separation based on the four studies just discussed. These quantities will be used in the analysis carried out here, as they will allow the comparison of results to those obtained earlier.

Table 16: Base parameters used in CO_2/N_2, O_2/N_2, CO_2/CH_4 and N_2/CH_4 simulation

Parameter	CO_2/N_2	O_2/N_2	CO_2/CH_4	N_2/CH_4
Purity	CO_2 99%	N_2 99%	CH_4 99%	CH_4 99%
Recovery	90% [6]	90%	99%	90%
Capacity (ton product day^{-1})	37,000 [6]	150	510 [9]	550 [8]
Raw composition	15/85%	21/79%	20/80%	14/86%
Membrane thickness (μm)	1	1	1	1
Membrane cost ($ m^{-2})	377	377	377	377

5.4.3 Selectivity, purity and number of stages

The number of stages required to perform a separation and reach a desired purity is one of the most important quantities that affect the economics of a membrane process. The relationship between selectivity, permeability and number of units required to separate CO_2/N_2, O_2/N_2, CO_2/CH_4 and N_2/CH_4 to achieve a desirable purity are shown in **Fig. 46**. The Robeson's line is plotted as a diagonal in the selectivity/permeability basal plane while the number of units required is displayed vertically.

The number of units presented in **Fig. 46** show the minimum number of units required to achieve at least the specified purity. For example, the separation of CO_2/N_2 requires only two units to achieve a purity of 99% as long as the selectivity is greater than 24. Note that selectivities higher than 76 will achieve a purity of $\geq$ 99.9% for two units.

The trend within the Robeson's line shows that at high selectivities and low permeabilities the number of units required is minimal (front-right quadrant of graph). As the selectivity decreases, the permeability becomes higher but the number of units increases. The separation of CO_2/N_2 targeting a purity of 99% requires 1 unit for selectivities greater than 560. Nevertheless, lower selectivities ranging from 560 to 24, 23 to 9 and 8 to 5 require a minimum of 2, 3, and 4 units, respectively, as indicated in the graph.

The separation of N_2/CH_4 is more difficult than O_2/N_2, CO_2/CH_4 and CO_2/N_2 since the Robeson's upper bound shows lower selectivities and permeabilities for the former gas pair. This difficulty results in higher number of units required to reach a specified purity. This can be seen in the larger y-scale range for those gas pairs (**Fig. 46**). Polymeric membranes can separate O_2/N_2 and CO_2/CH_4 effectively. In addition, since the initial concentration of N_2 and CH_4 is high, most O_2/N_2 and CO_2/CH_4 selectivities are high enough to purify nitrogen and natural gas without the necessity of a cascade system. The separation of CO_2 from N_2 can be achieved at high permeabilities with a moderate number of units.

From the Robeson's line, lower number of units implies lower permeabilities. To overcome these low permeabilities and reach any specified production target, either an increase in the membranes' surface area or the driving force (pressure) is required. An increase in the surface area affects proportionally the membrane costs. Increasing the pressure of the system can be a method to increase flux while maintaining low membrane area. Nevertheless, a pressure

increase represents higher compressor costs and higher electricity consumption. Pressure costs and the area of the membrane are in a trade-off that needs to be optimized. However, the optimum point does not necessarily correspond to the minimum number of units.

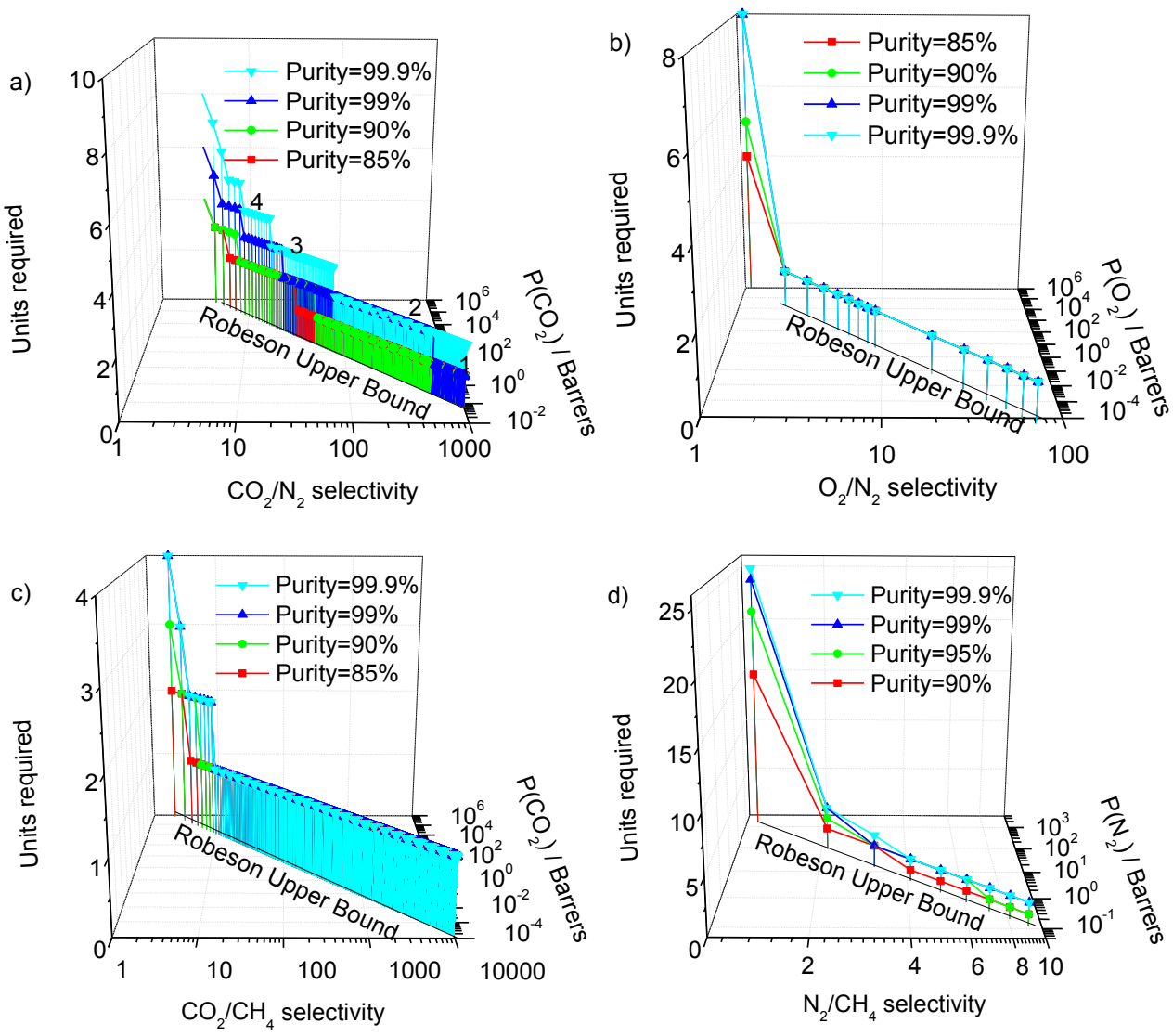

Fig. 46 : Number of stages required to purify gas pairs at different purities and permeabilities a) CO_2/N_2 b) O_2/N_2 c) CO_2/CH_4 d) N_2/CH_4.

5.4.4 Effects of pressure on membrane costs

The partial pressure difference between the permeate and the retentate streams is the driving force in membrane separations. The pressure required in membrane processes can be

generated by compressors installed at the entrance of each membrane unit. The costs of compressing gas mixtures increase at higher pressures (**Fig. 47**). An increase of pressure from 1 to 5 MPa has higher compression costs (50 to 100 \$ ton^{-1}) at selectivities ranging between 30 and 300. The number of compressor units influences the costs of compression. **Fig. 47** shows a step increase as each compressor unit is added. For example, at a selectivity of 30 the compression cost at 1 MPa changes from 60 to 70 \$ ton^{-1}.

Increasing the membrane's operating pressure allows the use of lower permeabilities and thus higher selectivities. However, there is also an economic tradeoff between the cost of compression and the membrane areas. Consequently, to achieve a desired production rate, recovery and purity, the cost of the compressors and the membranes must be optimized to achieve the most economical separation.

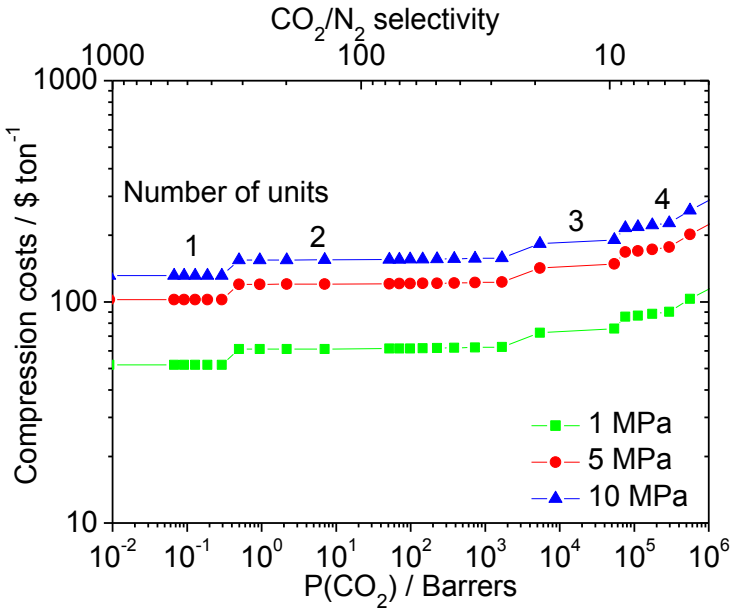

Fig. 47 : Effect of the number of stages on compression costs for the separation of CO_2/N_2.

This study evaluates the tradeoff relationship between compression, number of units and membrane area in economic terms. The costs shown in **Fig. 48** represent the costs of separating the gas pairs with the particular targets specified in **Table 16**. The expenses are plotted within the Robeson's line to illustrate the economics of the upper boundary.

Initially, the curves in **Fig. 48** show that the highest expenses, independently of the operating pressure, are at the lowest permeabilities. As the permeability increases, the costs

decrease exponentially. This is caused by the reduction of the area of the membrane required to reach a specific production rate and recovery. **Fig. 48** shows log-log plots where the exponential decay is represented as straight lines with slopes of ~-1. The negative unity slopes indicate that the cost of the membrane is the main contributor to the operation expenditure and that pressure has a small contribution at small permeabilities. The lowering of the membrane's area is always beneficial, as long as the selectivity does not affect the separation economically. However, the Robeson's line presents a tradeoff between selectivity and permeability.

After the exponential decrease in costs with increasing permeability, the expenses reach minimum points which have slopes = 0 indicating that the costs of compression and membrane contribute equally to the lowest expenditure. As shown in **Fig. 48**, the minimum point occurs when increasing the permeability does not improve the economics of the membrane. This is the result of lower selectivities at higher permeabilities. Consequently, as the selectivity decreases, the required number of membrane units needed to achieve the desired purities increases. This minimum point shows where the maximum flux across the membrane occurs while the number of compression stages, the surface area of the membrane, and the number of units are minimal.

After the minimum point, a moderate increase in costs is observed with increasing permeability and decreasing selectiity. This is caused by the increase in the number of membrane units which entail higher membrane area and compression requirements. This section has a slope > 0 indicating that the pressure is the highest expenditure.

The influence of the operating pressure on the economics of the process presents an interesting behavior (**Fig. 48**). Membranes with small permeabilities operating at high pressures show lower costs than at low pressures. This is a result of the costs of the membrane overcoming the costs for compression.

From another point of view, the curves in **Fig. 48** represent the optimal pressure difference between the retentate and the permeate stream. A membrane with a specific permeability should be operated at a pressure that reflects the lowest costs. For example, **Fig. 48 (b)** shows that to separate O_2 and N_2 at permeabilities between of 10^{-4} and 1 barrers, it is desired to operate the membrane system at a pressure of 10 MPa, rather than 1 or 5 MPa.

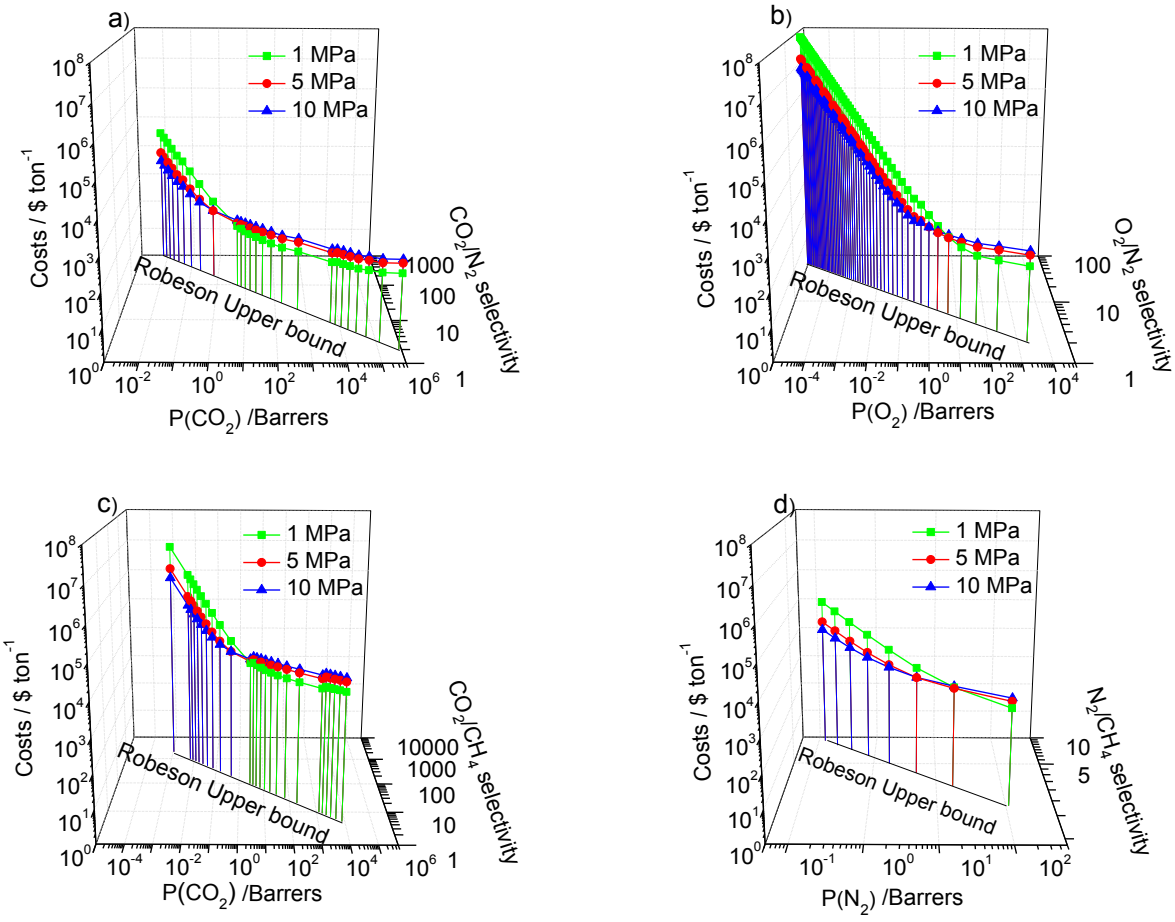

Fig. 48 : Effect of pressure drop across the membrane on costs for the separation of a) CO_2/N_2 b) O_2/N_2 c) CO_2/CH_4 d) d) N_2/CH_4.

For membranes with a given selectivity and permeability, it is possible to find the optimum operating pressure as shown in **Fig. 49**. This figure shows separately the costs of the membrane, compression, and total costs as a function of operating pressure and membrane area available for a membrane used to separate an O_2/N_2 mixture. The membrane was set with a selectivity of 8 and the production targets shown in **Table 16**.

Compression costs decrease as the area of the membrane increases as a result of the reduction in the pressure needed to achieve a specific flux (**Fig. 49**). In contrast, the membrane costs decrease as the operating pressure increases as a result of the reduction in the area for permeation required. The total costs of membrane operation are in tradeoff between the costs of the membrane and compression costs. This results in a minimized cost of operation. For instance this point occurs at a pressure of 6 MPa with a total cost of 900 \$ ton^{-1} for the O_2/N_2 separation

considered. This figure mainly focuses on operating parameters. By fixing the properties of the membrane to selectivity and permeability, it is possible to appreciate that there is an optimum operating pressure to achieve the targeted flux.

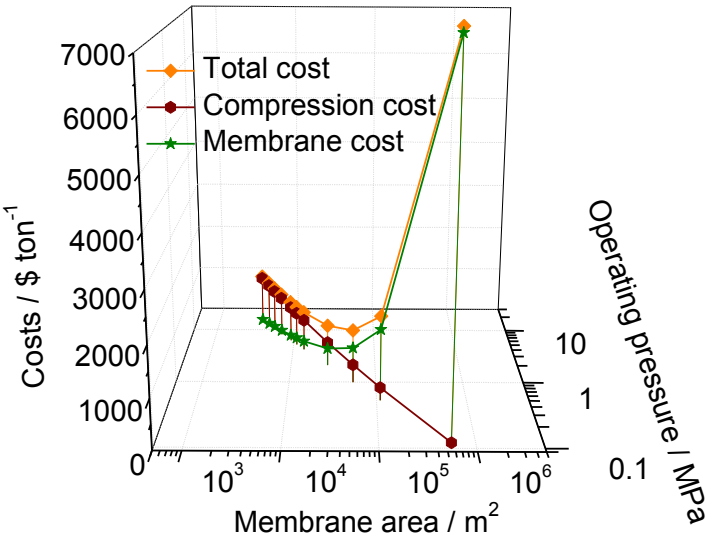

Fig. 49 : Effect of operating pressure, area of the membrane and costs for a membrane with an O_2/N_2 selectivity of 8.

5.4.5 Optimum economic point within the Robeson's line and operating recommendations

Obtaining the optimal point along the Robeson's line is not a straightforward task since the results depend on the targets of production (production rate, purity and recovery), feed compositions and the properties of the membranes. Nevertheless, this is achievable for the separation of gas pairs with specific targets. The optimum point is the critical point where the flux is maximized by minimizing the number of stages and the area of the membrane.

The optimal points within the Robeson's upper limit for the specified operating conditions presented in **Table 16** are shown in **Fig. 50**. For example, at 1 MPa the recovery of CO_2 from flue gases, it is desired to operate the membrane with a permeability of 3,200 barrers and CO_2/N_2 selectivity of 24. For the purification of N_2 from air, the membrane requires a permeability of 550 barrers and an O_2/N_2 selectivity of 4. For the removal of CO_2 from natural gas, it is desired to have a permeability of 2,000 barrers and a CO_2/CH_4 selectivity of 20. Similarly, for the removal of N_2 from natural gas requires a permeability of 110 barrers and a

N_2/CH_4 selectivity of 2. The number of stages required to reach a product purity of 99% at different operating pressures are summarized in **Table 17**. For the separation of CO_2/N_2 and N_2/CH_4, the results show that the optimal numbers of stages required are high at low operating pressure. However, for the separation of O_2/N_2 and CO_2/CH_4, the number of stages is fixed to 2 for all operating pressures. **Table 17** shows the equivalent optimum permeance for each gas pair. This allows designing a membrane with lower permeabilities but with the desired permeances. Even though the optimum points in Robeson upper bound were predicted, these values do not consider the degradation issues of the membrane material due to the contamination and the physical aging.

For all the gas pairs presented in this work, the cost of the membrane is the highest expense, even when operating at an optimum pressure. Consequently, by increasing the permeability of the membrane, the area required to achieve the separation is reduced. However, the reduction of the area is constrained by the number of membrane units which tend to increase at higher permeabilities. The economic relationship between permeability, selectivity and the number of membrane units were subject to a sensitivity analysis to demonstrate the stability of the optimized point and to provide recommendations when targeting the design of polymeric membranes. From the sensitivity analysis, it was found that recovery and production rate did not affect the optimized point significantly while the purity, operating pressure, membrane cost and membrane thickness had a considerable effect. The following recommendations are critical to consider when designing a process or membrane for the presented gas pairs in polymeric membranes.

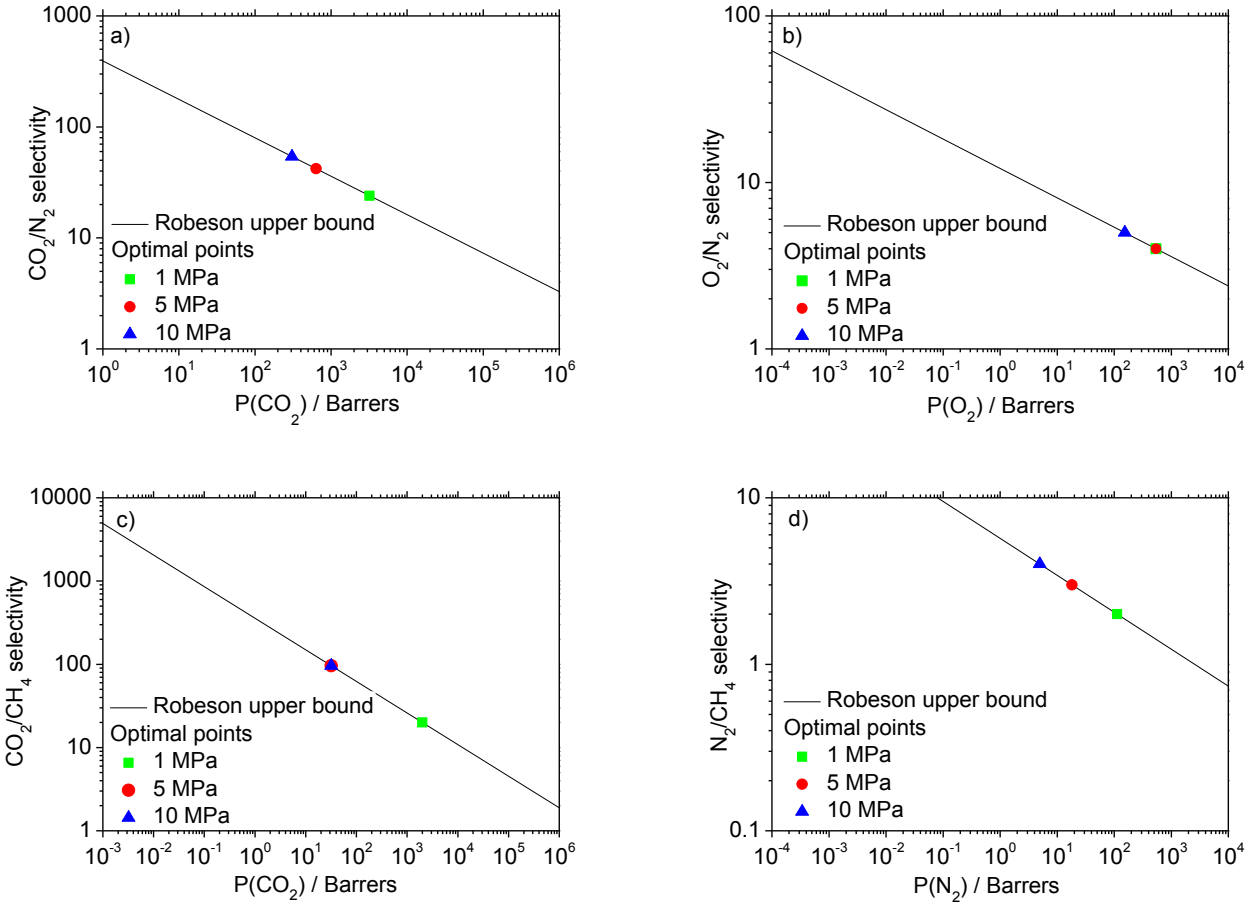

Fig. 50 :Optimum economic point in the Robeson's line for 99% purity a) CO_2/N_2 b) O_2/N_2 c) CO_2/CH_4 d) N_2/CH_4.

Table 17: Optimum points and operating conditions for the different gas pairs

Pair gas	Permeability (barrer)*	Permeance (mol $m^{-2}s^{-1}Pa^{-1}$)	Permeance (GPU)**	Selectivity	ΔP (MPa)	Number of stages
CO_2/N_2	3200	$3.57x10^{-8}$	107	24	1	3
	650	$7.22x10^{-8}$	215	42	5	2
	300	$3.33\ x10^{-8}$	99	54	10	2
O_2/N_2	550	$6.11\ x10^{-8}$	182	4	1	2
	550	$6.11\ x10^{-8}$	182	4	5	2
	150	$1.67\ x10^{-8}$	50	5	10	2
CO_2/CH_4	2000	$2.22\ x10^{-7}$	663	20	1	2
	30	$3.33\ x10^{-9}$	10	96	5	2
	30	$3.33\ x10^{-9}$	10	96	10	2
N_2/CH_4	110	$1.22\ x10^{-8}$	36	2	1	4
	20	$2.22\ x10^{-9}$	7	3	5	3
	5	$5.52\ x10^{-10}$	2	4	10	2

* 1 barrer = $3.35x10^{-16}$ mol m $m^{-2}s^{-1}Pa^{-1}$.

** 1 GPU = $1x10^{-6}$ cm^3(STP) $cm^{-2}s^{-1}cmHg^{-1}$ = $3.35x10^{-10}$ mol $m^{-2}s^{-1}Pa^{-1}$.

5.4.5.1 CO_2/N_2 optimization

- For an operating pressure of 1 MPa, use a CO_2/N_2 selectivity of 24 when targeting a separation with a purity ranging between 85 and 99%.
- Use a selectivity higher than 60 when the cost of the membrane is less than 10 \$ m^{-2}. Use a membrane with lower selectivity if the membrane cost is higher. For instance, it is recommended to use selectivities between 32-24 if the cost of the membrane is between 100 and 1000 \$ m^{-2}.
- Operate at a selectivity of 24 when the pressure is 1 MPa. Increase selectivity to operate at higher pressure. For instance, operate at a selectivity of 54 when the pressure is 10 MPa.
- It is recommended to engineer membranes with a thickness between 0.1 and 1 μm to operate with a selectivity of ~24.

5.4.5.2 O_2/N_2 optimization

- For an operating pressure of 1 MPa, target a selectivity of 4 and a permeability of 550 barrers when the objective is a N_2 purity between 85 to 99.9%.
- Use a selectivity of ~5 if the cost of the membrane is higher than 100 \$ m^{-2}.
- For pressure drops between 1 MPa and 10 MPa, use a selectivity of 4 to 5.
- It is recommended to use a membrane with a selectivity of 4 for membrane thicknesses >1 μm and higher selectivities for to thinner membranes. For instance, a 0.1 μm membrane should have a selectivity of at least 8.

5.4.5.3 CO_2/CH_4 optimization

- For an operating pressure of 1 MPa, target CO_2/CH_4 selectivities of 20 and permeabilities of 2,000 barrers for a CH_4 purity ranging between 85 to 99.9%.
- For membranes with costs ranging between \$5 and \$1,000 m^{-2} used selectivity of 20. When the cost of the membrane is higher, it is recommended to operate at lower selectivity (higher permeability) in order to minimize the area required.
- Increase permeability of the membrane if operating at lower pressures and decrease permeability if at higher pressures. For instance, at 1 MPa the optimum permeability is 2,000 barrers with a selectivity of 20 while at 10 MPa the optimum permeability is 30 barrers with a selectivity of 96.
    - For an operating pressure of 1 MPa, use a selectivity of 20 for membrane thicknesses of 1 μm; thinner membranes require to have higher selectivities. A membrane with a thickness of 0.1μm should have a selectivity of 100.

5.4.5.4 N_2/CH_4 optimization

- The separation of N_2/CH_4 requires operation at a selectivity around 2 when targeting a purity of 90 to 99% at an operating pressure of 1 MPa.
- The cost of the membrane should be between \$10 to \$3000 m^{-2} to target a selectivity of 2 or 3.
- For operating pressures between 1 and 10 MPa use low selectivities from 2 to 4. For higher pressures increase selectivity.

- For an operating pressure of 1 MPa, use a selectivity of 2 or 3 for membrane thicknesses between 0.1 to 1 μm.

5.4 Summary : Influence of the investigated parameters on CO_2/CH_4 separation

The tables shown in Appendix 3 and 4 summarize the influence of the several investigated parameters on the CO_2/CH_4 separation process. The effect of the operating pressures on the compression and membrane costs and on the number of stages for a methane purity of 99%, and a membrane thickness of 1 μm is shown in **Appendix 4**. As it can be seen, at low selectivities, the total costs depended mainly on the compression costs. However, at high selectivities, the total costs were dependent on the membrane costs. In addition, the lower the permeances were, the higher the number of stages became.

The effect of the required methane purity and the operating pressures on total costs and number of stages for a membrane thickness of 1 μm is shown in **Appendix 5**. As it can be seen, for a given purity and at low selectivities, low operating pressures resulted in lower total costs than at high pressures. However, at high selectivities, the opposite results were observed: the total costs at low operating pressures were higher than that at high pressures. As the required purity decreased, the total costs decreased slightly. For a purity of 80%, only one stage was needed for all selectivities.

5.5 Economical evaluation of previously synthesized membranes

Secondary alkylamine silica membrane (M-I) and mixed matrix membrane composed of 5 wt% SAPO-34/PEI (MMM-5) presented the highest investigated membrane performance (**Fig. 51**). The synthesis and characterization methods were detailed in chapter 3 and 4, respectively. An economic evaluation of both membranes was calculated using the model presented previously in this chapter. However, it should be noted that the Robeson upper boundary delimited the data of polymeric membranes. This line was used for other membrane materials only to situate the results. Therefore, the evaluation of M-II and MMM-5 membranes gives just a general idea about the operating costs.

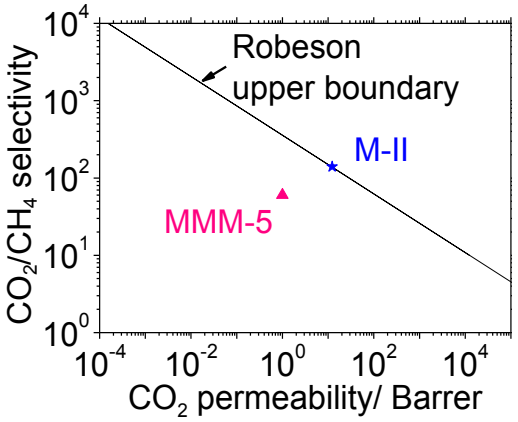

Fig. 51: Performance of the synthesized hybrid membranes plotted in Robeson diagram for CO_2/CH_4 separation. M-II refers to secondary alkylamine membrane where the performance was measured at 350 K and 0.1 MPa. MMM-5 refers to mixed matrix membrane with 5 wt% SAPO-34/PEI where the performance was measured at 303 K and 0.10 MPa.

Concerning the secondary alkylamine silica membrane (M-II), fortunately the obtained performance fell on the Robeson upper boundary with a CO_2 permeance of 1.3×10^{-7} mol $m^{-2}s^{-1}Pa^{-1}$ (CO_2 permeability of 12 Barrers) and a CO_2/CH_4 selectivity of 140 measured at a pressure difference of 0.10 MPa (**Fig. 51**). Similar steps were applied for the economic evaluation of the M-II membrane. An operating pressure of 0.10 MPa was considered. The effect of this pressure on the economics is shown in **Fig. 52**. The curve presented similar behavior as shown in **Fig. 48**. The performance of M-II membrane was close to the projection of the minimum costs (**Fig. 52**). Concerning the mixed matrix membrane (MMM-5), the obtained performance was below the Robeson upper boundary (**Fig. 51**). The simulation was run considering the permeability, the selectivity and the operating pressure of the MMM-5 membrane. The total costs were higher than that of M-II membrane. A comparison between the optimal point obtained for an operating pressure of 0.10 MPa and the total costs required for M-II and MMM-5 membranes to achieve 99% product purity is shown in **Table 18**. The M-II membrane required the lowest cost for the separation with only one stage compared to the MMM-5. The M-II membrane had the most reasonable permeance in the range of 1×10^{-7} mol $m^{-2}s^{-1}Pa^{-1}$.

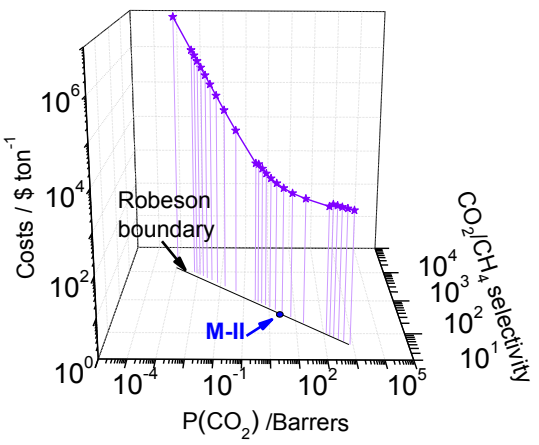

Fig. 52: Effect of an operating pressure of 0.10 MPa on membrane costs.

Table 18: Economic evaluation of M-II and MMM-5 membranes and comparison with the optimal point on the Robeson upper boundary for operating pressure of 0.10 MPa.

	Selectivity (-)	**Permeability (Barrers)**	**Permeance (mol $m^{-2}s^{-1}Pa^{-1}$)**	**Total cost (x10^3 \$ ton^{-1})**	**Number of stages**
Optimum point for an operating pressure of 0.10 MPa	14	5520	$1.8x10^{-6}$	1.5	2
M-II	140	12	$1.3x10^{-7}$	3.5	1
MMM-5	60	1.3	$4.5x10^{-10}$	900	2

5.6 Conclusions

The optimum point for the separation of CO_2/N_2, O_2/N_2, CO_2/CH_4, and N_2/CH_4 within the Robeson's upper limit was found by means of a techno-economical optimization. The constraints used in the analysis were the number of units required for a given purity, the cost of the membrane (area) required to achieve a desired flux, and the cost for compression to provide the driving force for the separation. The simulation showed that the optimum pressure drop to operate an optimized membrane is between 1 to 10 MPa. In addition, curves of costs and permeabilities were generated at different pressures to indicate the most economical operational pressure for any given permeability. The following optimum points were reported at an operating pressure of 1 MPa: CO_2/N_2 requires a permeability of 3,200 barrers and selectivity of 24, O_2/N_2 a

permeability of 550 barrers and a selectivity of 4, CO_2/CH_4 a permeability of 2,000 barrers and selectivity of 20 and for N_2/CH_4 a permeability of 110 barrers and selectivity of 2.

5.7 References

[1] Koros, W.J.; Mahajan, R. Pushing the limits on possibilities for large-scale gas separation: which strategies? J. Membr. Sci. 175 (2000) 181-196.

[2] H. Lin, M. Zhou, J. Ly, J. Vu, J.G. Wijmans, T.C. Merkel, J. Jin, A. Haldeman, E.H. Wagener, D. Rue, Membrane-based oxygen-enriched combustion. Ind. Eng. Chem. Res. 52 (2013) 10820.

[3] Cabasso, I.; Lundy, K.A. Method of making membranes for gas separation and the composite membranes. US Patent 4602922 A. July 1986.

[4] W.D. Seider, J.D. Seader, D.R. Lewin, Product and process design principles: synthesis, analysis, and evaluation, second ed., Wiley: New York, 2003.

[5] A. Gollan, H.M. Kleper, The economics of oxygen enriched air production via membranes, Proceedings from the 6th Annual Industrial Energy Technology Conference 1. (1984) 298-306.

[6] J.P. Van der Luus, C.A. Hendriks, K. Blok, Feasibility of polymer membranes for carbon dioxide recovery from flue gases. Energy Convers. Manage. 33 (1992) 429-436.

[7] M.A. Carreon, S. Li, J.L. Falconer, R.D. Noble, SAPO-34 seeds and membranes prepared using multiple structure directing agents. Adv. Mater. 20 (2008) 729-732.

[8] B.D. B hide, S.A. Stern, Membrane process for the removal of acid gases from natural gas, I Optimization of operating conditions and process configurations. J. Membr. Sci. 81 (1993) 209-237.

[9] B.D. Bhide, S.A. Stern, Membrane process for the removal of acid gases from natural gas. II. Effects of operating conditions, economic parameters and membrane properties. J. Membr. Sci. 81 (1993) 239-252.

Chapter 6: Summary and Conclusions

The separation of carbon dioxide from natural gas using hybrid inorganic-organic membranes was investigated. Two types of hybrid membranes were prepared; alkylamine silica membranes and mixed matrix membranes.

The alkylamine silica membranes were selected because of the well-known affinity between CO_2 and amine functionalities. In this case, the selective layer was deposited on the surface of porous alumina supports by chemical vapor deposition at 673 K using a mixture of silica precursor (tetraethylorthosilicate) and amino-silica precursor (3-aminopropyltriethoxysilane) and oxygen as co-reagent. The amino-silica ratio was varied in order to determine the optimum combination for the separation. The highest separation performance was obtained for the membrane having a amine to silica ratio of 20% with a CO_2 permeance of $2.3x10^{-7}$ mol $m^{-2}s^{-1}Pa^{-1}$ and a CO_2/CH_4 ideal selectivity 40 at 393 K. The XPS analysis confirmed the presence of nitrogen on the surface in two states, $-NH_2$ and $-NH_3^+$, and both contribute to the interactions with CO_2. The transport mechanism for CO_2 permeation was surface diffusion and for CH_4 passage was gas-translation. The mean pore size of the hybrid membrane was calculated by Tsuru's method and was estimated to be 0.44 nm.

The effect of primary and secondary amine was also investigated. Two alkylamine silane precursors having primary (3-aminopropyltrimethoxysilane) and secondary ((3-methylaminopropyl) trimethoxysilane) amine groups were selected for the study. The obtained membranes were compared to an amine free membrane in order to understand the relationship between the microstructure and the performance of the alkylamine silica membranes. The selective layer was deposited using an amine to silica ratio of 20 wt% and chemical vapor deposition temperature of 673 K. The highest separation performance was obtained at different CVD times for each membrane. The performance followed the order of base strength of the amine; secondary > primary > no amine. The amine-free membrane had a CO_2 permeance of $2.1x10^{-8}$ mol $m^{-2}s^{-1}Pa^{-1}$, a CO_2/CH_4 selectivity of 4. The primary amine membrane displayed a CO_2 permeance of $2.1x10^{-8}$ mol $m^{-2}s^{-1}Pa^{-1}$, a CO_2/CH_4 selectivity of 70. The secondary amine achieved a CO_2 permeance of $1.3x10^{-7}$ mol $m^{-2}s^{-1}Pa^{-1}$, a CO_2/CH_4 selectivity of 140. The performance of the secondary amine was the highest and has values of commercial significance, and indicates that the membranes are promising for practical applications. The mean pore size of the synthesized hybrid membranes were calculated by Tsuru's method and was estimated to be 0.37, 0.36, 0.43 nm for free, primary and secondary amino-silica membranes, respectively. Even

though, the membrane with secondary amine group had the biggest pore size, the CO_2/CH_4 separation was the best. The transport of CO_2 through the amine modified silica layer was enhanced by the formation of carbamate intermediates which was verified by XPS analysis. Temperature dependence measurements indicated that CO_2 was transported by repeated adsorption/ diffusion/ desorption cycles. The membrane with secondary amine functionality was stable under 20% relative humidity during 60 h.

Mixed matrix membranes were synthesized by dispersing zeolite SAPO-34 in polyetherimide polymer. Dichloromethane was selected to dissolve the polymer rather than N-methyl-2-pyrrolidone; a conventional solvent used for the polyetherimide membranes since the former solvent resulted in a homogeneous selective layer and gave high CO_2/CH_4 selectivity. Various SAPO-34 amounts from 0 to 10 wt% were dispersed in the polymer precursor dissolved into dichloroethane. A membrane with 5 wt% SAPO-34 loading presented the highest performance with a CO_2 permeance of 4.41×10^{-10} mol $m^{-2}s^{-1}Pa^{-1}$ with a CO_2/CH_4 selectivity of 60. The separation occurred based on the difference in gas solubility. The SAPO-34 decreased CH_4 permeance by increasing its diffusion pathway. Higher loading caused the agglomeration of the zeolite particles.

Finally, the optimum point within the Robeson's upper boundary was determined based on a techno-economical optimization. The separation of CO_2/N_2, O_2/N_2, CO_2/CH_4, and N_2/CH_4 was taken as examples. The optimization parameters used in the analysis were the number of units required for a given purity, the cost of the membrane (area) required to achieve a desired flux, and the cost for compression to provide the driving force for the separation. The simulation showed that the optimum pressure drop to operate an optimized membrane is between 1 to 10 MPa. In addition, curves of costs and permeabilities were generated at different pressures to indicate the most economical operational pressure for any given permeability. The following optimum points were reported at an operating pressure of 1 MPa: CO_2/N_2 requires a permeability of 3,200 barrers and selectivity of 24, O_2/N_2 a permeability of 550 barrers and a selectivity of 4, CO_2/CH_4 a permeability of 2,000 barrers and selectivity of 20 and for N_2/CH_4 a permeability of 110 barrers and selectivity of 2.

Based on the overall results presented in this thesis, several future works can be considered:

- The effect of the number secondary amine functionality in the alkylamine-silica membranes could be investigated.
- Mixture primary and secondary amine functionalities within the same membrane can also be a promising membrane material.
- The reaction between SAPO-34 and polytherimide using alkylamine silane may be an option to eliminate all defects in the interface zeolite/polymer in the mixed matrix membranes.

Nomenclature

α	Probability for diffusion through a micropore.
$\bar{P}_A^{(i)}$	Permeance of gas A at stage i (mol $m^{-2}Pa^{-1}s^{-1}$)
$\bar{P}_i$	Permeance of species *i* [mol $m^{-2}s^{-1}Pa^{-1}$].
ΔE_{SD}	Energy barrier to be overcome by diffusion [J mol^{-1}].
ΔH_a	Enthalpy of adsorption [J mol^{-1}].
A_i	Membrane area required for stage i [m^2]
$C_{Comp}^{(i)}$	Capital cost for each compressor [$]
$C_M^{(i)}$	Capital cost for membrane a unit [$]
C_U	Utility cost [$ yr^{-1}]
$F_A^{(i)}$	Molar flow rate of gas A permeate at stage i [mol s^{-1}]
$F_B^{(i)}$	Molar flow rate of gas B permeate at stage i [mol s^{-1})
N_{SD}	Molar flux [mol m^{-2} s^{-1}].
$P_A^{(i)}$	Permeability of gas A at stage i [mol $m^{-1}Pa^{-1}s^{-1}$]
$P_{He}\sqrt{M_{He}/M_i}$	Permeance of i-th component predicted from He permeance under the Knudsen diffusion mechanism.
P_I	Pressure at the compressor inlet [Pa]
P_O	Pressure at the compressor outlet [Pa]
PWR_{Comp}^{i}	Power required for compressor at stage i [kW]
Pur_A	Purity of gas A
Pur_B	Purity of gas B
$R_A^{(i)}$	Retention rate of gas A at stage i [mol s^{-1}]
Rec_A	Overall recovery of species A
Rec_B	Overall recovery of species B

a_g	Pre-exponential.
q_s	Saturation amount of adsorbed molecules [mol kg^{-1}].
$\alpha^*_{i,j}$	Ideal selectivity of a specie *i* over *j* [-].
ΔP	Pressure difference between the feed and permeate (Pa)
A	Species A
A	Surface area of the membrane [m^2].
AIP	Aluminum isopropoxide.
AlOOH	Boehmite.
AlP	Aluminum isopropoxide.
APTES	(3-Aminopropyl)triethoxysilane.
APTMS	3-aminopropyltrimethoxysilane.
B	Species B
CH_3COOH	Acetic acid.
CVD	Chemical vapor deposition.
DCE	Dichloroethane
d_{He}	Kinetic diameter of helium [nm].
d_i	Kinetic diameter of gas i [nm].
d_p	Estimated membrane pore size [nm].
f	Ratio of the permeance of the i-th component ($\bar{P}_i$) to that predicted from a reference component (He) based on the Knudsen diffusion mechanism.
F_D	Design factor
F_i	Molar flow rate of the gas *i* [mol s^{-1}].
F_M	Material factor
GPU	Gas permeation unit.
HNO_3	Nitric acid.
K	Adsorption equilibrium constant [Pa^{-1}].
K’	Gas specific heat ratio
L	Membrane thickness
M-0, M-I, and M-II	Membranes having no amine, primary amine and secondary amine functionality, respectively.
MMM-x [x=0, 5, and 10]	Mixed matrix membranes having 0, 5, and 10 wt% SAPO-34/PEI.

MAPTMS	(3-methylaminopropyl) trimethoxysilane.
M_{He}	Molecular weight of helium [g mol^{-1}].
M_i	Molecular weight of gas i [g mol^{-1}].
MMD	Membrane material design.
MMMs	Mixed matrix membranes.
MSE	Membrane system engineering.
n	Number of membrane units.
NMP	N-methyl-2-pyrolidone.
p	Pressure [Pa].
PTMS	Propyltrimethoxysilane.
PVA	Polyvinyl alcohol.
q	Amount of adsorbed gas molecules per unit mass of adsorbent [mol kg^{-1}].
R	Amino-silica ratio.
r	Unit recovery.
R^2	Regression coefficient.
RH	Relative humidity [%].
TEOS	Tetraethylorthosilicate.
Ti	Inlet temperature [K].
ΔP_i	Partial pressure difference of a gas *i* between the inner and the outer side of the membrane tube [Pa].
ε	Porosity of the membrane.
η	Compressor mechanical efficiency.
θ	Fractional occupancy of adsorption sites.
λ	Distance between the adsorption sites [m].
λv	Velocity in the right direction [m s^{-1}].
v	Jump frequency of the molecule between adsorption sites [s^{-1}].
ρ	Density of the gas molecules [kg m^{-3}].
τ	Tortuosity.
C	Annual cost [$ yr^{-1}].
D	Diffusivity [m^2 s^{-1}]

S	Solubility [mol $m^{-3}Pa^{-1}$]
α	Selectivity of gas A respected to gas B.

Appendix 1

The relationship between the values of the cubic root of $k_{0,i}$ and the kinetic diameter of the permeated gas molecule for M-0, M-I and M-II membranes are shown in **Fig. 53**. A good linear correlation was observed for the three membranes and the following equation was fitted to the obtained results by using d_p and k_0 as fitting parameters.

$$\sqrt[3]{k_{0,i}} = \sqrt[3]{k_0}\, d_p - \sqrt[3]{k_0}\, d_i \qquad \textbf{Eq. (48)}$$

where d_i is the kinetic diameter of a permeating gas i [nm], d_p is the effective pore size [nm], and k_0 is a structural parameter of the membrane.

The adjustable parameter k_0 has a physical meaning that depends only on the membrane porous structure and is independent of the permeating gas species as defined by the following equation.

$$k_0 = \frac{N_P\sqrt{2\pi}}{6\tau A_m L} \qquad \textbf{Eq. (49)}$$

where N_P is the number of pores, A_m is the membrane area [nm^2], τ is the tortuosity, and L is the effective membrane thickness [nm].

The obtained values of d_p and k_0 are summarized in **Table 19**. The values of the estimated membrane pore size d_p were compared to NKP and mNKP plot methods. They showed complete agreement with those obtained in mNKP plot. Therefore, it can be concluded that the adopted methods were consistent for the estimation of the membrane pore size.

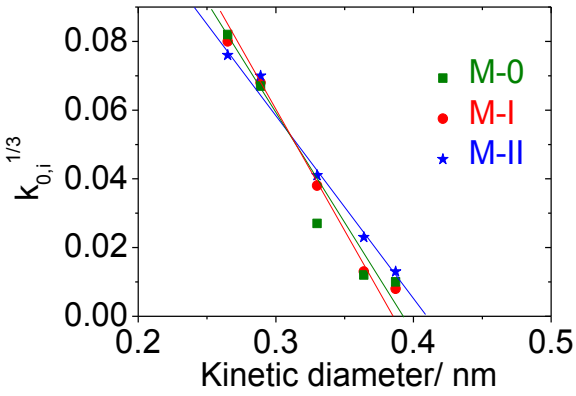

Fig. 53: Relationship between the values of $k_{0,i}^{1/3}$ and the kinetic diameter of gas molecules plotted for M-0, M-I and M-II membranes.

Table 19: Estimated values of d_p and k_0 for M-0, M-I, M-II membranes.

Membrane	d_p (nm)			k_0 (nm^{-3}) **(Fig. 53)**
	NKP plot without considering CO_2 permeance	Modified NKP plot	From **Fig. 53**	
M-0	0.37	0.38	0.38	0.252
M-I	0.36	0.37	0.39	0.251
M-II	0.43	0.43	0.41	0.160

Appendix 2

Ideal selectivity and separation factors as a function of temperature and pressure difference of M-II membrane

Temperature (K)	ΔP (MPa)	Ideal selectivity	Separation factor		
			CO_2:CH_4 (mol%)		
			10:90	50:50	80:20
303	0.05	21	26	25	24
	0.1	17	23	21	21
	0.15	16	20	19	19
	0.2	14	18	17	17
	0.25	13	17	15	16
323	0.05	28	42	38	40
	0.1	21	37	33	34
	0.15	23	32	29	26
	0.2	21	29	26	27
	0.25	23	26	24	26
343	0.05	81	103	114	141
	0.1	68	88	99	113
	0.15	59	76	85	99
	0.2	54	69	76	87
	0.25	49	63	55	80
363	0.05	95	116	120	138
	0.1	85	62	118	122
	0.15	74	61	116	108
	0.2	64	59	116	98
	0.25	58	58	114	102
393	0.05	63	87	91	103
	0.1	58	78	87	97

	0.15	54	73	85	99
	0.2	51	64	81	94
	0.25	48	60	77	90
453	0.05	22	24	26	27
	0.1	25	23	25	26
	0.15	24	24	25	25
	0.2	23	23	24	25
	0.25	23	23	23	24

Appendix 3

Ideal selectivity and separation factors as a function of temperature and pressure difference of M-0 membrane.

Temperature (K)	**ΔP (MPa)**	**Ideal selectivity**	**Separation factor**		
			CO_2:CH_4 mol ratio		
			10:90	**50:50**	**80:20**
303	0.05	N.M	N.M	1.91	2.11
	0.1	1.0	N.M	N.M	N.M
	0.15	1.2	1.40	1.70	1.76
	0.2	1.1	1.30	N.M	1.67
	0.25	1.2	1.39	1.51	1.63
323	0.05	2.6	N.M.	1.4	3.2
	0.1	2.1	1.4	1.6	2.8
	0.15	1.8	1.4	1.5	2.5
	0.2	1.6	1.4	1.5	2.4
	0.25	1.3	1.4	1.5	2.4
343	0.05	3.7	2.0	3.9	4.7
	0.1	2.8	1.7	3.1	3.7
	0.15	2.1	1.5	2.7	3.1
	0.2	2.3	1.4	2.5	2.9
	0.25	3.65	1.3	2.3	2.7
393	0.05	6.3	7.0	6.9	7.5
	0.1	4.9	5.8	5.7	6.4
	0.15	4.3	5.1	5.1	5.6
	0.2	3.8	4.7	4.6	5.2
	0.25	3.4	4.5	4.4	4.8
453	0.05	10.9	7.9	7.8	7.5
	0.1	5.3	6.8	6.7	6.6
	0.15	4.5	6.1	6.1	6.0

	0.2	4.2	5.6	5.7	5.6
	0.25	3.8	5.4	5.3	5.2

N.M. : not measured

Appendix 4

Effect of operating pressures on compression and membrane costs and number of stages for a methane recovery of 99%, methane purity of 99%, and membrane thickness of 1 μm.

Selectivity	Permeability (Barrers)	Total costs ($ ton^{-1})				Compression costs ($ ton^{-1})				Membrane costs ($ ton^{-1})				Number of stages
		0.1 MPa	1 MPa	5 MPa	10 MPa	0.1 MPa	1 MPa	5 MPa	10 MPa	0.1 MPa	1 MPa	5 MPa	10 MPa	
5	77200	1.82 x10^{3}	6.57 x10^{3}	1.26 x10^{4}	1.60 x10^{4}	1.80 x10^{3}	6.57 x10^{3}	1.26 x10^{4}	1.60 x10^{4}	20.3	2.03	4.05 x10^{-1}	2.03 x10^{-1}	3
10	12400	1.52 x10^{3}	5.18 x10^{3}	9.92 x10^{3}	1.27 x10^{4}	1.41 x10^{3}	5.17 x10^{3}	9.92 x10^{3}	1.27 x10^{4}	1.01 x10^{2}	10.1	2.02	1.01	2
60	110	1.21 x10^{4}	5.99 x10^{3}	9.63 x10^{3}	1.21 x10^{4}	1.34 x10^{3}	4.91 x10^{3}	9.41 x10^{3}	1.20 x10^{4}	1.08 x10^{4}	1.08 x10^{3}	2.15 x10^{2}	1.08 x10^{2}	2
100	29	3.46 x10^{4}	7.25 x10^{3}	8.17 x10^{3}	9.90 x10^{3}	1.06 x10^{3}	3.90 x10^{3}	7.49 x10^{3}	9.56 x10^{3}	3.35 x10^{4}	3.35 x10^{3}	6.71 x10^{2}	3.35 x10^{2}	1
140	12	8.25 x10^{4}	1.20 x10^{4}	9.12 x10^{3}	1.04 x10^{4}	1.06 x10^{3}	3.90 x10^{3}	7.49 x10^{3}	9.56 x10^{3}	8.14 x10^{4}	8.14 x10^{3}	1.63 x10^{3}	8.14 x10^{2}	1
700	0.2	5.67 x10^{6}	5.71 x10^{5}	1.21 x10^{5}	6.62 x10^{4}	1.06 x10^{3}	3.90 x10^{3}	7.49 x10^{3}	9.56 x10^{3}	5.67 x10^{6}	5.67 x10^{5}	1.13 x10^{5}	5.67 x10^{4}	1

Appendix 5

Effect of the methane purity and the operating pressures on the total operating costs and number of stages for a membrane thickness of 1 μm.

Selectivity	Permeability (Barrers)	Methane purity of 99%				Methane purity of 90%				Methane purity of 80%			
		Total costs ($ ton^{-1})			Number of stages	Total costs ($ ton^{-1})			Number of stages	Total costs ($ ton^{-1})			Number of stages
		1 MPa	5 MPa	10 MPa		1 MPa	5 MPa	10 MPa		1 MPa	5 MPa	10 MPa	
5	77200	6.57 x10^3	1.26 x10^4	1.60 x10^4	3	6.06 x10^3	1.16 x10^4	1.48 x10^4	3	3.90 x10^3	7.49 x10^3	9.56 x10^3	1
10	12400	5.18 x10^3	9.92 x10^3	1.27 x10^4	2	4.92 x10^3	9.42 x10^3	1.20 x10^4	2	3.90 x10^3	7.49 x10^3	9.56 x10^3	1
60	110	5.99 x10^3	9.63 x10^3	1.21 x10^4	2	4.41 x10^3	7.60 x10^3	9.62 x10^3	1	3.91 x10^3	7.50 x10^3	9.57 x10^3	1
100	29	7.25 x10^3	8.17 x10^3	9.90 x10^3	1	5.86 x10^3	7.89 x10^3	9.76 x10^3	1	3.93 x10^3	7.50 x10^3	9.57 x10^3	1
140	12	1.20 x10^4	9.12 x10^3	1.04 x10^4	1	8.65 x10^3	8.44 x10^3	1.00 x10^4	1	3.98 x10^3	7.51 x10^3	9.57 x10^3	1
700	0.2	5.71 x10^5	1.21 x10^5	6.62 x10^4	1	3.34 x10^5	7.36 x10^4	4.26 x10^4	1	9.80 x10^3	8.67 x10^3	1.02 x10^4	1